NUREG/CR-1360
EGG-2024
Distribution Category: R3

REACTIVITY INITIATED ACCIDENT TEST SERIES
RIA SCOPING TESTS
FUEL BEHAVIOR REPORT

R. Scott Semken
Shu Shiozawa
Zoel R. Martinson
Richard K. McCardell
Philip E. MacDonald
Jose A. Fernandez
Steven K. Fukuda

Published April 1980

EG&G Idaho, Inc.
Idaho Falls, Idaho 83401

Prepared for the
U.S. Nuclear Regulatory Commission
Washington, D.C. 20555
Under DOE Contract No. DE-AC07-76IDO1570
FIN No. A6041

ABSTRACT

This report presents and discusses the results from the Reactivity Initiated Accident Scoping Tests (RIA-ST) conducted in the Power Burst Facility (PBF) at the Idaho National Engineering Laboratory. Four unirradiated test fuel rods were subjected, one during each of the four tests, to one or more power transients resulting in estimated axial peak radial average fuel enthalpies ranging from 185 to 350 cal/g (205 to 530 cal/g peak fuel enthalpy near the pellet surface). These values of fuel enthalpy resulted from total radial average energy depositions ranging from 250 to 695 cal/g UO_2. This report describes the design and conduct of the tests and presents and discusses test results in terms of the test objectives which were to (a) evaluate proposed methods for measuring fuel rod energy deposition during a power burst, (b) determine the peak fuel enthalpy threshold for failure and the rod failure mechanism of unirradiated fuel rods at BWR hot-startup coolant conditions, (c) determine the relative sensitivity of test instrumentation to high radiation during a power burst, and (d) determine the magnitudes and sources of pressure pulses resulting from rod failure during an inadvertent high energy deposition in the PBF liquid-filled test loop.

SUMMARY

The Reactivity Initiated Accident Scoping Tests (RIA-ST) were enabling tests performed prior to the RIA Test Series being conducted by EG&G Idaho, Inc., for the U.S. Nuclear Regulatory Commission. The main objectives of the scoping tests were to (a) evaluate proposed methods for measuring fuel rod energy deposition during a power burst, (b) determine the peak fuel enthalpy threshold for failure and the rod failure mechanism of unirradiated fuel rods at BWR hot-startup coolant conditions, (c) determine the relative sensitivity of test instrumentation to high radiation during a power burst, and (d) determine the magnitudes and sources of pressure pulses resulting from rod failure during an inadvertent high energy deposition in the PBF liquid filled test loop.

The RIA Scoping Tests consisted of four, separate, single-rod tests designated RIA-ST-1, RIA-ST-2, RIA-ST-3, and RIA-ST-4. Each test was performed with a fuel rod assembled from available unirradiated pressurized water reactor (PWR) zircaloy cladding (0.914 m active fuel length) enclosed in a cylindrical flow shroud sized to provide a coolant flow volume approximately equivalent to the volume per rod in a commercial BWR rod bundle. The PWR-size test rods were not prototypical, but fuel rod behavior during an RIA was expected to be roughly equivalent for the PWR and BWR rod types. The four unirradiated test fuel rods were each subjected to one or more power transients resulting in maximum axial peak radial average fuel enthalpies ranging from 185 to 350 cal/g (205 to 530 cal/g peak fuel enthalpy near the pellet surface). These enthalpies resulted from total radial average energy depositions of 250 to 695 cal/g UO_2, respectively.

Five methods were evaluated for measuring test rod radial average fission energy deposited during each transient. The five measurement methods had estimated uncertainties ranging from ±11 to ±14%. Detailed independent review of the measurement methods confirmed that none were unreliable; however, direct radiochemical burnup analyses were judged to be the most reliable method. The other methods relied on calorimetric measurements of fuel rod power during steady state operation and therefore had to be interrelated to the calorimetric measurement instruments to determine the fuel rod energy deposition during a power burst.

Axial peak radial average fuel enthalpy is the limiting parameter for the Nuclear Regulatory Commission's licensing criteria regarding an RIA event. The evidence suggests that peak fuel enthalpy near the pellet surface is the parameter most important to fuel behavior during such an event. The Fuel Rod Analysis Program-Transient, Version 5 (FRAP-T5), computer code was used to account for heat transfer from the fuel pellet for each energy deposition in determining peak fuel enthalpies for the RIA Scoping Tests. The calculations indicated that in each case, nearly all of the energy transferred from the fuel pellet into the cladding remained in the cladding when the peak fuel enthalpy was reached.

The axial and radial peak fuel enthalpy threshold for failure determined in the RIA Scoping Tests was about 265 cal/g, which occurred near the surface of the fuel. This value corresponds to an axial peak radial average fuel enthalpy failure threshold of 240 cal/g, resulting from a total axial peak radial average energy deposition of 315 cal/g UO_2. The scenario of cladding failure near the failure threshold is as follows. Plastic flow of the cladding occurred, producing regions of cladding wall thickening and thinning. The zircaloy was then oxidized by steam and UO_2, and became completely embrittled in the thinner regions. Extensive cracking of the embrittled cladding occurred due to thermal stresses during the quench and rewet following ~30 s of film boiling. After the occurrence of extensive fuel shattering along grain boundaries in the two fuel rods tested at axial peak radial average fuel enthalpies of 250 and 260 cal/g (275 to 290 cal/g UO_2 radial peak near the pellet surface), approximately 10 and 15% of the UO_2 fuel, respectively, was swept out of the flow shrouds.

The radiation sensitivity of five pressure transducers, one thermocouple, a linear variable differential transformer (LVDT), two strain gages, and two turbine flowmeters was evaluated. All of the pressure transducers performed well in the RIA high-radiation burst field environment and can be considered for use in future RIA testing. The LVDT, normally used to measure cladding elongation, showed no indication of radiation sensitivity, nor did the Type S (platinum-platinum, 10% rhodium) thermocouple. The two strain gages, however, displayed

significant radiation sensitivity due to gamma heating, and appear to be useless in the RIA radiation environment. A slow response time of the turbine flowmeter signal conditioning electronics created significant error in the flow measurements during the tests. This is not an inherent problem.

The RIA-ST-4 experiment was performed to evaluate the consequences of an inadvertent high energy deposition during the RIA Test Series. The magnitude of the RIA-ST-4 power transient was well above that considered possible in a commercial power reactor. Probable molten fuel-coolant interaction produced a measured pressure pulse of 35 MPa during the 350-cal/g axial peak radial average fuel enthalpy (530 cal/g peak) power burst. The total fuel energy deposition for this burst was 695 cal/g. A mechanical-to-nuclear energy conversion ratio of 6% was calculated. The working fluid which produced the pressure pulse was postulated to be water in a liquid, liquid-vapor, or supercritical state during a molten fuel-coolant interaction. Although a large source pressure was measured, only low magnitude pressure increases were measured elsewhere in the PBF in-pile tube and loop piping.

CONTENTS

NOTE: All of the appendixes to this report are presented on microfiche attached to the inside of the back cover.

FIGURES

TABLES

REACTIVITY INITIATED ACCIDENT TEST SERIES
RIA SCOPING TESTS
FUEL BEHAVIOR REPORT

1. INTRODUCTION

Rapid insertion of excess reactivity into a light water nuclear reactor (LWR) core has long been recognized as an accident mechanism with the potential for failure of the fuel rod cladding. Extensive cladding failure and subsequent dispersal of fuel into the coolant could disrupt the core such that the postaccident capability for cooling the core would be significantly impaired. To minimize the possibility of damage from postulated inadvertent reactivity initiated accidents (RIAs) in commercial LWRs, United States Nuclear Regulatory Commission (NRC) design requirements have been imposed on reactivity control systems to limit "the potential amount and rate of reactivity increase to assure that the effects of postulated reactivity accidents can neither (a) result in damage to the reactor coolant pressure boundary greater than limited local yielding nor (b) sufficiently disturb the core, its support structure, or other reactor pressure vessel internals to impair significantly the capability to cool the core."[1]

Worst-case RIAs in commercial LWRs are postulated to result from the rapid removal of control rod elements from the reactor core. In a pressurized water reactor (PWR), the RIA is a result of the hypothesized mechanical rupture of a control rod drive mechanism housing or control rod drive nozzle, which results in the coolant system pressure ejecting an inserted control rod from the core. In a boiling water reactor (BWR), the worst-case RIA (rod dropout) results from (a) the separation (complete rupture, breakage, or disconnection) of an inserted control rod drive from its cruciform control blade at or near the coupling, (b) the sticking of the control blade in the inserted position as the rod drive is withdrawn, and (c) the rapid falling of the control blade to the withdrawn rod drive position.

A reactor operator (or vendor) is expected to show that:

> "1. Reactivity excursions will not result in a radial average fuel enthalpy greater than 280 cal/g UO_2 at any axial location in any fuel rod.
>
> 2. Maximum reactor pressure during any portion of the assumed transient will be less than the value that will cause stresses to exceed the Emergency Condition stress limits as defined in Section III of the ASME Code.
>
> 3. Off-site dose consequences will be well within the guidelines of 10 CFR 100."[1]

The axial peak radial average fuel enthalpy limitation ($\leq$280 cal/g) is based on a Nuclear Regulatory Commission staff review of fuel behavior experimental data available prior to 1974. Their findings indicated that failure consequences were insignificant for total energy depositions below 300 cal/g UO_2 for both irradiated and unirradiated UO_2 fuel rods subjected to rapid power excursions. Therefore, an axial peak radial average fuel enthalpy of 280 cal/g was considered a conservative maximum limit to ensure minimal core damage and maintenance of both short- and long-term core cooling capability.[a] The guidelines regarding reactor coolant pressure boundary stresses are assumed to be met if compliance with the enthalpy limitation is satisfactorily demonstrated. Additional calculations must be performed to prove that the guidelines regarding off-site dose consequences are met.

Complex analysis techniques are used to estimate the effects of postulated RIAs in light water reactors.[2,3,4] These techniques generally couple the transient neutronics behavior, fuel rod thermal and mechanical response, and the coolant hydrodynamic response. Verification of these analytical models is incomplete, however, due to the limitations in existing fuel behavior data. Much of the applicable RIA experimental data were obtained several years ago in the Special

a. Axial peak radial average fuel enthalpy is somewhat less than the associated total energy deposition because of heat transfer from the fuel to the cladding and coolant during the power transients and the relatively large fraction of the total energy which is due to delayed fissions (10 to 20%, depending on the reactor design).

Power Excursion Reactor Test (SPERT) (Capsule Driver Core) and Transient Reactor Test Facility (TREAT) test programs, which investigated the behavior of single or small clusters of fuel rods under atmospheric pressure and temperature conditions, with no forced coolant flow and zero initial powers. Similar tests have been performed in the Japanese Nuclear Safety Research Reactor (NSRR).

In each of these facilities, a driver core with encapsulated test fuel in a central flux trap was operated to produce a power excursion. The magnitude and time duration of these excursions were comparable to those of severe, hypothesized RIAs in LWRs. The experiments were performed with single fuel rods (or a small cluster of rods) placed at the center of test capsules containing stagnant water. The initial coolant conditions for the CDC, TREAT, and NSRR tests were closely representative of BWR cold critical conditions, namely, reactor critical at a power level of 10^{-8} of rated power, coolant at 300 K, and atmospheric pressure with no flow. Energy deposition, and consequent enthalpy increase in the test fuel, was found to be the single most important independent variable. The incipient failure threshold of unirradiated fuel rods was in the range of 205 to 225 cal/g axial peak radial average fuel enthalpy (260 to 265 cal/g peak fuel enthalpy near the fuel surface). These enthalpies correspond to total energy depositions in the range of 245 to 265 cal/g UO_2.[a] The narrow range of values (260 to 265 cal/g UO_2) is evidence that peak fuel enthalpy near the pellet surface is the variable most important to incipient cladding failure.

In the CDC, TREAT, and NSRR tests, test rods failed by cladding melting, cracking of embrittled cladding, or both. The incipient failure threshold was found to be relatively insensitive to cladding material, cladding heat treatment, fuel form, material, and gap width. Single NSRR fuel rods within shroud enclosures failed at lower energy depositions than rods not enclosed in shrouds. The incipient failure threshold for rods enclosed in a 14-mm cylindrical shroud was found to be in the range of 210 to 245 cal/g UO_2 total energy deposition, compared with 245 to 265 cal/g UO_2 for unenclosed fuel rods. Reference 5 presents a review and summary of the SPERT and NSRR results.

The test program currently underway in the Power Burst Facility (PBF) at the Idaho National Engineering Laboratory is expected to provide RIA fuel behavior data under conditions more nearly typical of power reactor operation, thus allowing further assessment and development of analytical models. These tests are being conducted by the Thermal Fuels Behavior Program of EG&G Idaho, Inc., as part of the Nuclear Regulatory Commission's Reactor Safety Research Program.[6,7] The objectives of these RIA tests are to (a) determine fuel rod failure threshold enthalpies and failure mechanisms for both fresh and previously irradiated rods, (b) determine the mechanisms and consequences of rod failure for previously irradiated and fresh fuel at (or slightly above) the NRC design limit axial peak radial average fuel enthalpy of 280 cal/g, and (c) measure the thermal, mechanical, and chemical interaction behavior of a typical LWR fuel rod during an RIA. For each test in the PBF RIA Series I Tests, the pressure, temperature, and flow rate of the coolant will be typical of the hot-startup condition in a commercial boiling water reactor. These conditions were selected in order to simulate the coolant conditions of the postulated RIA believed to be the most severe—the BWR control rod dropout accident during hot-startup conditions.

Extensive thermal-hydraulic analyses were performed to compare the behavior of the shorter length (0.9 m) PBF test rods with full-length (3.8 m) BWR/6 fuel rods during an RIA event at BWR hot-startup conditions. The analyses indicated that for the same energy deposition and initial coolant mass flux, the PBF test rods experience nearly the same maximum cladding temperatures as the full-length power reactor fuel rods, but lower coolant outlet velocities which cause a slower reduction in cladding temperature. The analyses indicated that the maximum cladding temperature and duration of film boiling calculated for the PBF RIA fuel rods would be most similar to the calculated RIA behavior of the commercial 3.8-m BWR/6 fuel rods if (a) the PBF rod flow shroud inner diameter was minimized, (b) the flow loss coefficient at the inlet of the PBF rod flow shroud was equivalent to the loss coefficient of a BWR/6 fuel assembly, and (c) initial

a. Axial peak radial average fuel enthalpy is reported because it relates to the NRC licensing criteria. Total energy deposition relates to previous RIA testing results, and peak fuel enthalpy near the pellet surface is important to fuel rod behavior.

PBF coolant conditions were equivalent to commercial BWR/6 hot-startup conditions. These conditions were incorporated into the design of the RIA tests.

The PBF was designed primarily for performing very high-power excursions. In the PBF, a power excursion is initiated by a fast-acting drive system that moves the transient rods at a velocity of 9.5 m/s, which corresponds to a reactivity addition rate of about 50$/s or a reactivity insertion time of about 50 ms. In contrast, BWRs have devices attached to the control rods to limit the rod drop velocity. The maximum control rod free-fall velocity is about 1.5 m/s, which corresponds to a reactivity insertion time of about 1.15 s. Thus, in terms of rod drop speed, the PBF is not prototypical of a commercial power reactor, however, the influence of this difference in reactivity insertion times between the PBF and a BWR is mitigated since the time constant for heat transfer between the fuel and the coolant is long, compared to the reactivity insertion time for a BWR.

The PBF RIA Series I tests are listed in Table 1. The Reactivity Initiated Accident Scoping Tests (RIA-ST) were preliminary tests, performed prior to the PBF RIA Series I program. The RIA Scoping Tests consisted of four tests designated RIA-ST-1, RIA-ST-2, RIA-ST-3, and RIA-ST-4. Completed August 30, 1978, the Scoping Tests were performed to examine and resolve some anticipated RIA research problems before the NRC programmatic tests were conducted. The main objectives of the RIA Scoping Tests were to:

1. Evaluate proposed methods for measuring fuel rod energy deposition during a power burst

2. Determine the peak fuel enthalpy threshold for failure and the rod failure mechanism of unirradiated fuel rods at BWR hot-startup coolant conditions

3. Determine the relative sensitivity of test instrumentation to high radiation during a power burst

4. Determine the magnitudes and sources of pressure pulses resulting from rod failure during an inadvertent high energy deposition in the PBF liquid filled test loop.

This report presents an analysis, interpretation, and discussion of the results from the RIA Scoping Tests. Reference 8 presents the experimental data from those tests. The PBF system design and capabilities, and the design and conduct of the Scoping Tests are presented in the following sections. Analyses and discussions of the RIA-ST results in terms of each of the four test objectives are then presented. First, the results of five independent energy insertion measurement methods are compared and evaluated. The method having the highest probability of being correct is identified and uncertainties are estimated. Second, the estimated fuel enthalpy threshold for cladding failure of unirradiated LWR-type fuel rods tested at BWR hot-startup conditions is identified, and rod damage at 225 cal/g axial peak radial average fuel enthalpy is compared with rod damage at 250 and 260 cal/g. Third, relative PBF test instrument sensitivity to the high radiation bursts is discussed, and finally, a preliminary assessment of source pressure and fuel-coolant interaction during a very high energy power transient[a] in a liquid filled system is presented. The conclusions drawn from the RIA Scoping Tests are also presented.

Details of fuel rod assembly, design, and pretest characterization are presented in Appendix A, Appendix B reviews the code input for the fuel rod behavior analyses, Appendix C presents details of the postirradiation examination, and finally, Appendix D presents a WHAM hydraulic code analysis of the RIA-ST-4 postfailure pressure data. All of the appendixes to this report are provided on microfiche attached to the inside of the back cover.

a. Considered inpossible in a commercial power reactor, this power transient was performed to evaluate the consequences to the PBF of an inadvertent high energy deposition during the RIA Test Series.

TABLE 1. PBF RIA SERIES I TESTS[a]

Test	Number of Rods	Fuel Rod Type	Burnup (MWd/t)	Fuel Material	Pellet Density (%)	Pellet Outside Diameter (mm)	Diametral Gap (mm)	Axial Peak Radial Average Fuel Enthalpy (cal/g)	Objectives and Comments
RIA-ST-1	1	PWR-type	0	UO_2	94	8.23	0.190	250[d]	To address potential problem areas in the performance of the PBF RIA Series 1 tests.
RIA-ST-2	1	PWR-type	0	UO_2	94	8.23	0.190	260[d]	
RIA-ST-3	1	PWR-type	0	UO_2	94	8.23	0.190	225[d]	
RIA-ST-4	1	PWR-type	0	UO_2	93	9.3	0.210	350[d]	
RIA 1-1	2	MAPI[b]	5500	UO_2	94	8.58	0.165	285[d]	To provide a comparison of irradiated and unirradiated fuel behavior using Saxton and MAPI rods at the NRC licensing criteria enthalpy limit of 280 cal/g UO_2.
	2	Saxton[c]	0	UO_2	94	8.53	0.165	285[d]	
RIA 1-2	4	MAPI	5000	UO_2	94	8.58	0.165	185[d]	To test irradiated MAPI rods at the expected fuel enthalpy to cause cladding failure. Two rods will be pressurized to BWR end-of-life conditions.
RIA 1-3	4	BWR/6	5000 to 12 000	UO_2	95	10.57	0.228	220[e]	To test preirradiated BWR/6 fuel rods at a peak fuel enthalpy of 220 cal/g.
RIA 1-4	9	MAPI	5000	UO_2	94	8.58	0.165	280[e]	To investigate core coolability of clustered, preirradiated MAPI rods for comparison with the results of Test RIA 1-1.
RIA 1-6	4	BWR/6	0 to 20 000	UO_2	95	10.57	0.228	240[e]	To test preirradiated BWR/6 rods at a higher peak fuel enthalpy for comparison with the results of Test RIA 1-3.
RIA 1-7	9	BWR/6	5000 to 12 000	UO_2	95	10.57	0.228	165[e]	To investigate the failure threshold of a cluster of preirradiated BWR/6 fuel rods.

a. All tests in this series will be performed from BWR hot-standby conditions.

b. Mitsubishi Atomic Power Industries of Japan.

c. The Saxton reactor was a small, prototype, closed cycle, pressurized, light water reactor designed by Westinghouse Electric Corporation for the USAEC.

d. Actual result of tests.

e. Enthalpy may be changed, depending on results of previous tests.

2. PBF DESIGN AND CAPABILITIES

The PBF was designed as a subassembly testing facility for obtaining experimental data to aid in defining the behavior of nuclear fuels in off-normal operating conditions. The PBF reactor core can be operated in three modes: (a) a steady state mode with power levels up to 28 MW, (b) a natural power burst mode with reactor periods as short as 1.0 ms and peak powers as high as 270 GW, and (c) a shaped burst mode (for example, a square wave power shape) with up to 1350 MJ (1350 MW·s) integrated energy. The facility consists primarily of an open tank reactor vessel; canal; driver core region; central flux trap region containing an in-pile tube (IPT) in which the test fuel is located; and a pressurized water flow loop that permits control of the test fuel rod coolant flow rate, temperature, and pressure within typical LWR levels. Figure 1 is a cutaway view of the reactor, and Figure 2 illustrates the cross section of the core. The experimental envelope for operation of the PBF is provided in Table 2. The open top reactor vessel provides access for installation and removal of test hardware. The canal is used for transfer and temporary storage of PBF reactor fuel and test fuel assemblies.

The PBF core is approximately a right-circular annulus, 1.3 m in diameter and 0.91 m high, enclosing a centrally located, vertical test space 0.21 m in diameter. The PBF fuel consists of stainless steel rods containing ceramic ternary fuel pellets. The fuel rods are grouped in fuel canisters containing from 28 to 63 fuel rods, which form a close-packed, square fuel lattice. The reactor is controlled with eight control rods and four transient rods, each consisting of a cylindrical annulus of boron carbide positioned in a steel canister and operated in air-filled shrouds. The transient rods are capable of controlled movement at speeds up to 9.5 m/s. These rods are used to initiate and control natural and shaped power bursts, whereas steady state operation is controlled with only the control rods.

The PBF reactor core is cooled by a low-pressure primary coolant system. Coolant flow through the core at a rate of up to 0.95 m^3/s is provided by two 260-kW primary coolant system pumps. The primary system is composed entirely of stainless steel. Heat exchange from the primary to the secondary coolant system is provided through two vertical tube and shell heat exchangers. Ultimate heat rejection is to the atmosphere through a two-bay redwood cooling tower.

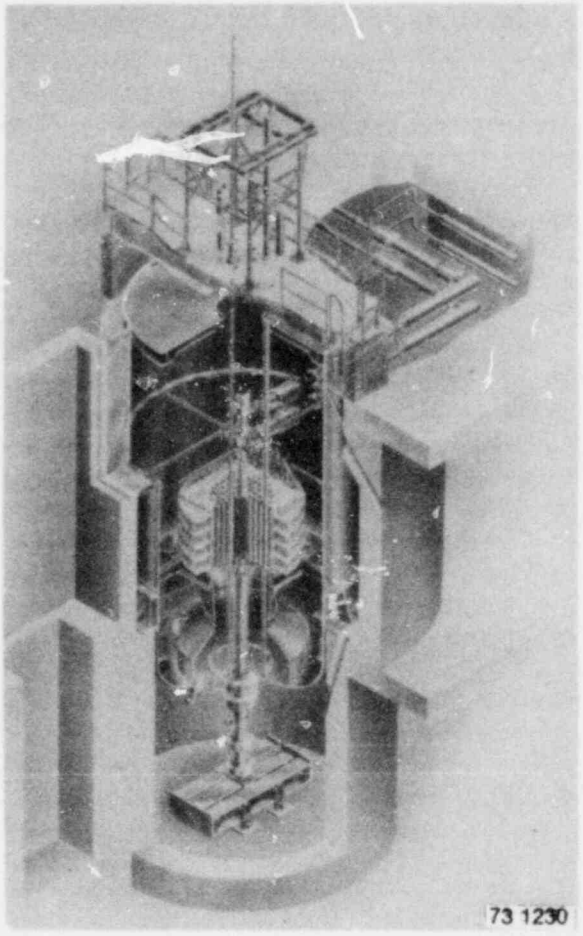

GS-018-040

Figure 1. Cutaway view of PBF reactor.

Test fuel, either single rods or rod clusters, is contained in the in-pile tube shown in Figure 3, a thick walled, Inconel 718, high-strength pressure tube designed to contain the steady state operating pressure and the pressure surges that may result from test fuel failure. Any conceivable failure (such as cladding failure, gross fuel melting, fuel-coolant interactions, fuel failure propagation, or fission product release) of the test fuel during a test can be safely contained by the PBF in-pile tube without damage to the driver core. The maximum steady state pressure that can be maintained in the loop coolant system is 15.6 MPa, and the in-pile tube part of the coolant system is designed

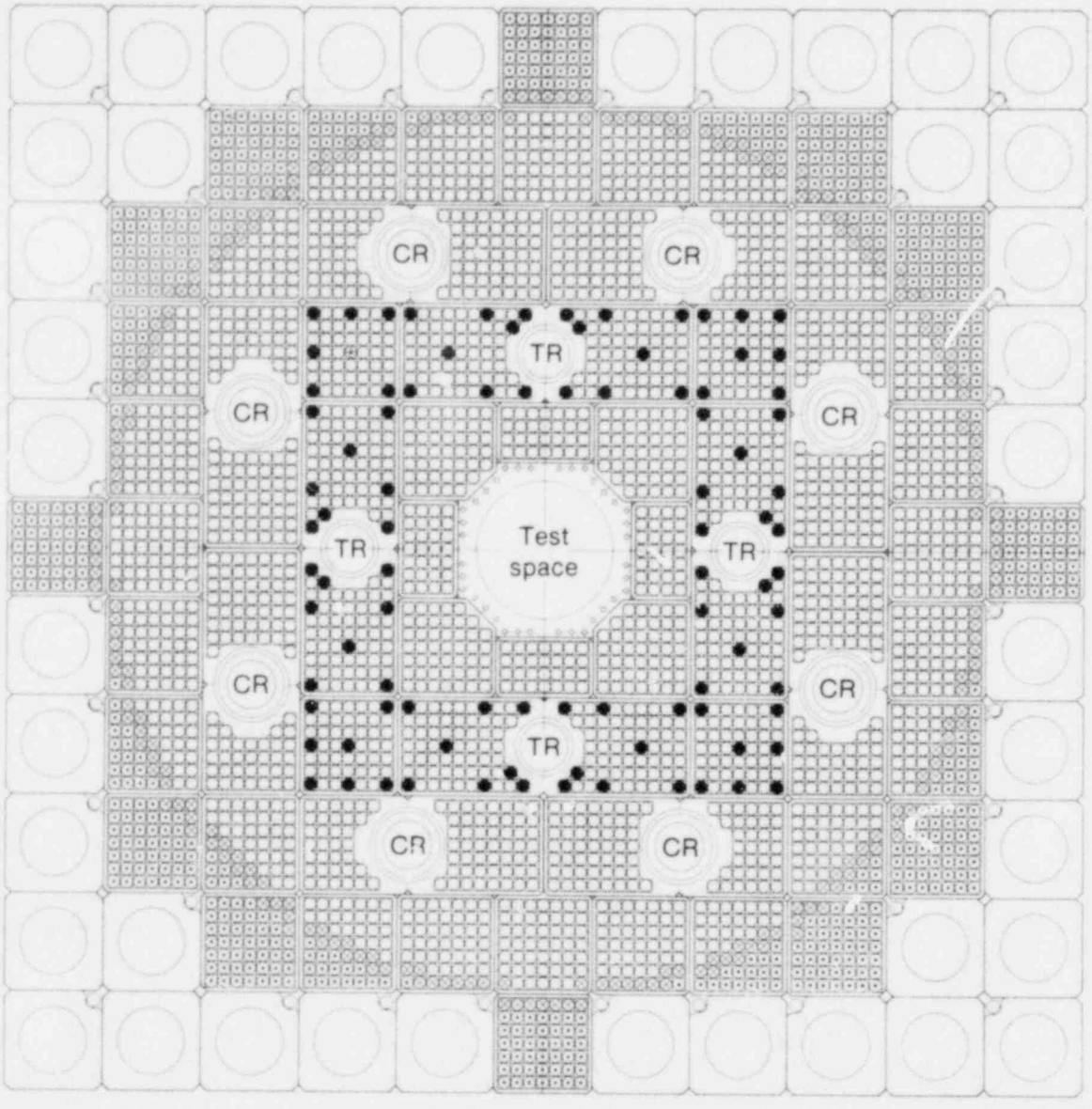

INEL-A-9917

○ Ternary fuel rod
⊗ Stainless steel reflector rod
⊙ Aluminum filler rod
● Stainless steel shim rod
⊕ Source rod
CR Control rod
TR Transient rod

Figure 2. Cross section of PBF core.

TABLE 2. EXPERIMENTAL ENVELOPE FOR OPERATION OF PBF

Parameter or Variable	Design Capabilities and/or Limits
Maximum core steady power	28 MW
Maximum core power in shaped burst	1000 MW
Maximum core power in natural burst	270 GW nominal for design burst[a]
Peak neutron flux in IPT	$\sim 7 \times 10^{17}$ nv at 270 GW
Maximum duration for steady power operation	48 hours
Maximum power for initiation of shaped burst	100 kW
Maximum power for initiation of natural burst	28 MW nominal
Maximum core fuel temperature for steady power operation	2573 K nominal at 28 MW
Maximum core fuel temperature for burst operation	2623 K without coupling; 2733 K with coupling
Maximum core fuel enthalpy for steady power operation	7451 MJ/m^3 nominal at 28 MW
Maximum core fuel enthalpy for burst operation	8539 MJ/m^3 without coupling; 10 318 MJ/m^3 with coupling
Maximum reactivity insertion for natural burst operation	4.60$ nominal for design burst
Maximum transient rod speed for natural burst operation	9.52 m/s
Maximum transient rod speed for shaped burst or steady power operation	0.51 m/s
Minimum asymptotic period for natural burst operation	1.0 ms for design burst
Maximum energy release for natural burst operation	1350 MJ nominal for design burst; 1750 MJ nominal for design burst with coupling
Maximum experiment fission power	2 MW
Maximum experiment Pu inventory	147 g

TABLE 2. (continued)

Parameter or Variable	Design Capabilities and/or Limits
Maximum fission product inventory in test fuels	That resulting at end of following operation history; 2 MW for 558 days, 42 days decay time; 2 MW for 48 hours, 7 days decay time
Maximum loop operating temperature	616 K
Maximum loop operating pressure	15.6 MPa
Maximum transient source pressure within IPT	51.7 MPa

a. Design burst is defined as the natural burst initiated from zero power that results in 8540 MJ/m^3 at the core hot spot. Nominally, achieving 8540 MJ/m^3 at the core hot spot requires a 1.0-ms-period burst initiated by a 4.60$ reactivity step, with an energy generation of 1350 MJ.

to contain source pressures within the test cluster that are 51.7 MPa above the steady state pressure without yielding. Penetrations in the top head of the in-pile tube can accommodate instrumentation leads for measurement of approximately 100 test variables in test fuel rod clusters.

Coolant flow enters the in-pile tube through the lower nozzle and flows down the annulus between the in-pile tube wall and the flow tube. Flow reverses at the bottom of the flow tube, moves through the central region of the flow tube, and flows out the upper nozzle. The lower section of the flow tube contains a catch basket which protects the bottom of the in-pile tube from local overheating by providing a heat sink and collection basin for any fuel fragments that may settle to the bottom of the in-pile tube.

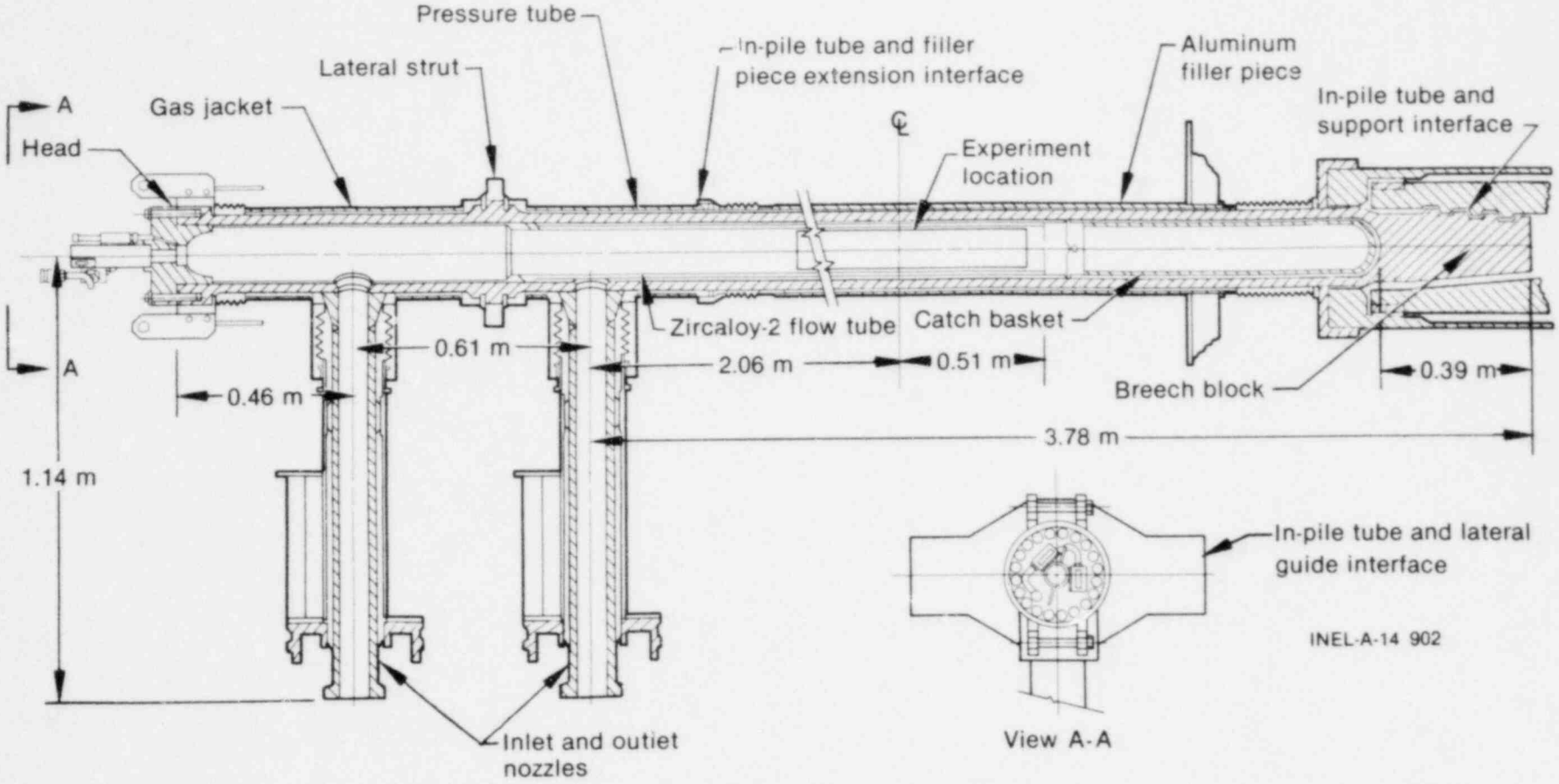

Figure 3. Axial cross section of PBF in-pile tube.

3. TEST DESIGN AND CONDUCT

Four, separate, single-rod tests were performed for the RIA Scoping Tests. Each test was configured with a test rod enclosed in a circular flow shroud to provide a uniform coolant flow cell with a water-to-fuel ratio similar to that of each rod in a commercial BWR rod bundle. A test train support structure assembly positioned the rod and shroud vertically in the IPT test space so that the radial centerline of the test fuel coincided with the centerline of the IPT and the PBF core and so that the active length of the test fuel rod coincided with the active length of the PBF core fuel. A power calibration was performed (in RIA-ST-1 and RIA-ST-4) for each of two rod types used in the four tests, and each test included one or more natural power bursts.

Detailed descriptions of the hardware and fuel rod designs, the instrumentation, and the test conduct are presented in the following subsections. Complete fuel rod characterization data can be found in Appendix A (provided on microfiche attached to inside of back cover).

3.1 Fuel Rod Design

Schematics of the RIA Scoping Tests rods are provided in Figure 4. The nominal design characteristics of the rods are given in Table 3. The rods were assembled using available unirradiated cladding of PWR design and unirradiated UO_2 fuel pellets which were ground to fit. The PWR-size test rods were not prototypical, but fuel rod behavior during an RIA was expected to be roughly equivalent for the BWR and PWR types. The RIA-ST-1, RIA-ST-2, and RIA-ST-3 rods were backfilled with helium gas to a cold pressure of 0.19 MPa, and the RIA-ST-4 rod was filled with helium to 3.79 MFa.

3.2 Test Train Hardware Design

Individual circular flow shrouds were fabricated from zircaloy-4 for each test rod. The shrouds for the RIA-ST-1, RIA-ST-2, and RIA-ST-3 rods had a nominal inner diameter of 16.3 mm and an outer diameter of 22.6 mm. The RIA-ST-4 flow shroud had a nominal inner diameter of 19.3 mm and an outer diameter of 25.4 mm. Fuel particle catch screens were installed at the inlet and outlet of the RIA-ST-4 flow shroud.

The PBF single-rod test train assembly was used for the tests. Figure 5 illustrates the test train and shows the positioning of the instruments. In this test assembly, the fuel rod was held rigidly at the top, free to expand axially downward. Coolant flow entered the in-pile tube near the top and passed down the annulus outside of the 0.12-m-outside-diameter flow tube. The flow then entered the lower region of the hardware where it divided. Part of the total flow passed through the turbine flowmeters and an orifice plate and entered the fuel rod coolant flow shroud. The remaining coolant flow bypassed the fuel rod shroud. The bypass ratio was fixed by the flow resistance of each path and was approximately 10 to 1. The coolant flow recombined above the flow shroud outlet and passed through the upper particle filter. The orifice above the flowmeters was sized to best model the thermal-hydraulic conditions expected during an RIA transient in a commercial BWR fuel rod bundle.

3.3 Instrumentation and Measurements

Instrumentation for the RIA scoping tests was selected to provide pressure pulse measurement, calorimetric determination of test rod power, and radiation sensitivity evaluation of the fuel rod instrumentation to be used in future RIA tests. No instruments were installed on the test fuel rods. The test train instrumentation measured the coolant temperature, pressure, and volumetric flow rate; the neutron flux; and the test fuel rod cladding elongation. In addition, several instruments were included in the test train for radiation sensitivity evaluation. Reactor and pressurized coolant flow loop instrumentation was used for reactor power and pressure pulse measurements.

The test train instrumentation, as shown in Figure 5, was as follows:

1. Two 69-MPa EG&G Idaho free field pressure transducers were located at the lower test train mounting plate. One was active for measuring large pressure pulses and the other was sealed and backfilled with helium to a cold pressure of 2.07 MPa for radiation sensitivity evaluation.

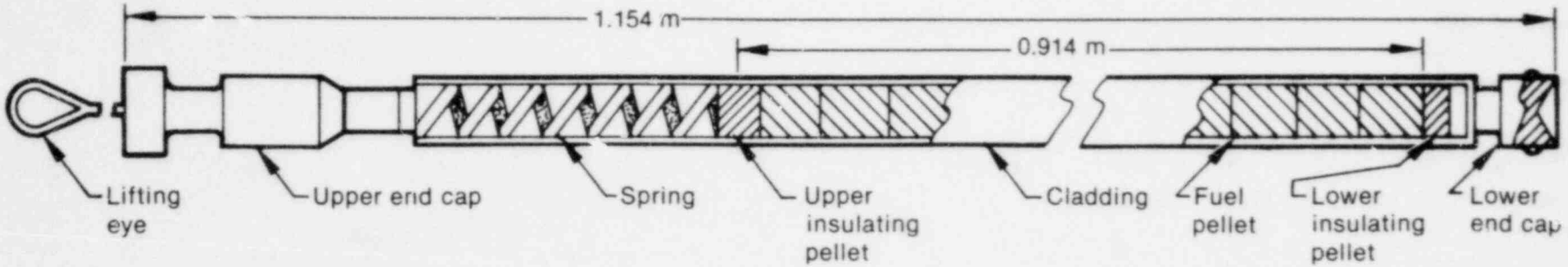

(a) RIA-ST-1,-2, and -3 rod design

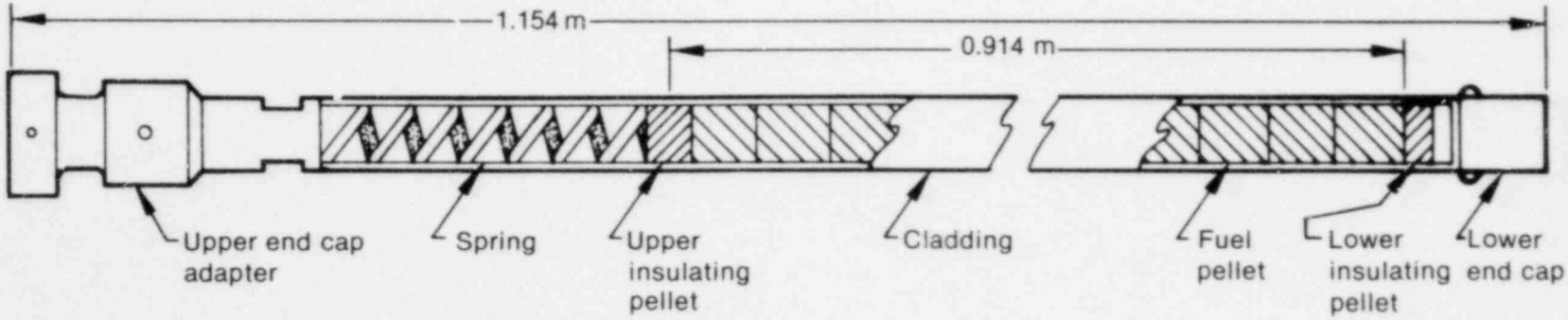

(b) RIA-ST-4 rod design

	Fuel Pellet outside diameter	Cladding outside diameter	Tube wall thickness
RIA-ST-1 -2,-3	8.23 mm	9.70 mm	0.64 mm
RIA-ST-4	9.3 mm	10.73 mm	0.61 mm

INEL-A-14 924

Figure 4. Illustrations of the RIA Scoping Tests rods.

TABLE 3. RIA SCOPING TESTS FUEL ROD DESIGN CHARACTERISTICS

Characteristic	RIA-ST-1, RIA-ST-2, and RIA-ST-3	RIA-ST-4
Fuel		
Material	UO_2	UO_2
Pellet OD (mm)	8.23	9.3
Pellet length (mm)	15.2	15.49
Pellet enrichment (wt%)	5.8	20
Density (% of theoretical)	94%	93%
Fuel stack length (m)	0.914	0.914
End configuration	Dished	Dished
Burnup	0	0
Cladding		
Material	Zircaloy-4	Zircaloy-4
Tube OD (mm)	9.70	10.73
Tube wall thickness (mm)	0.64	0.61
Fuel Rod		
Overall length (m)	1.0	.0
Fill gas	Helium	Helium
Initial gas pressure (MPa)	0.19	3.79

2. One 69-MPa EG&G Idaho free field pressure transducer was located on the upper test train hanger rod to measure large pressure pulses.

3. Two 17.2-MPa EG&G Idaho pressure transducers were located on the fuel rod upper shroud extension. One was active for measuring coolant pressure, and the other was sealed and backfilled with helium to a cold pressure of 2.07 MPa for radiation sensitivity evaluation.

4. One 17.2-MPa Schaevitz Engineering pressure transducer was positioned on the fuel rod upper shroud extension for radiation sensitivity evaluation. It failed prior to the first test, RIA-ST-1.

5. One 17.2-MPa Kaman Sciences Corp., pressure transducer was installed on the fuel rod upper shroud extension for radiation sensitivity evaluation. It was sealed to eliminate any response due to coolant pressure changes and was backfilled with helium to a cold pressure of 2.07 MPa.

6. One 17.2-MPa Bell & Howell pressure transducer was located on the lower end of the hanger rod for radiation sensitivity evaluation. For RIA-ST-4, this transducer was connected to a tube which penetrated the fuel rod flow shroud at the axial peak power elevation.

7. Two Flow Technology turbine flowmeters were mounted in tandem and located at

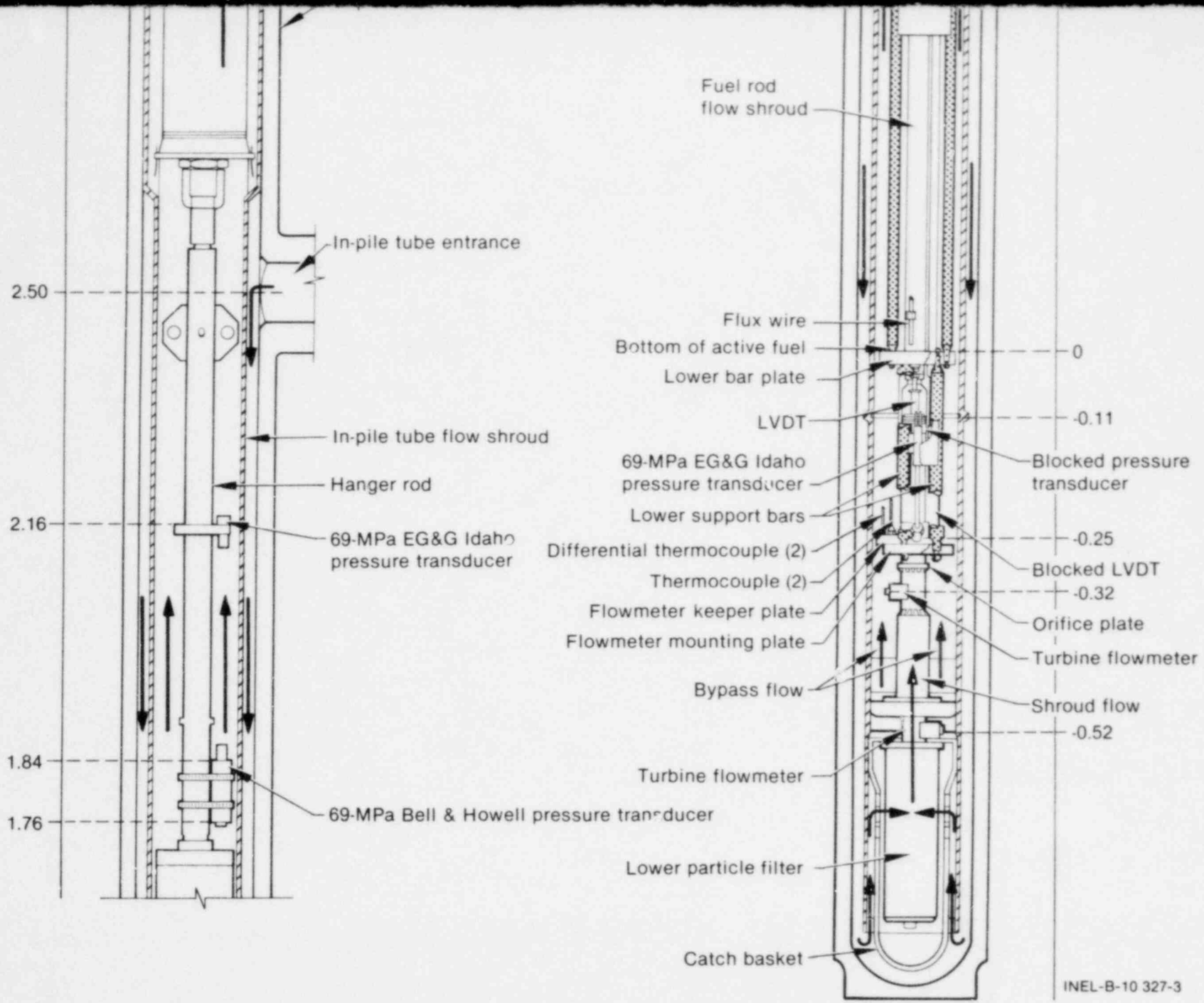

Figure 5. The RIA-ST test train assembly with instrumentation.

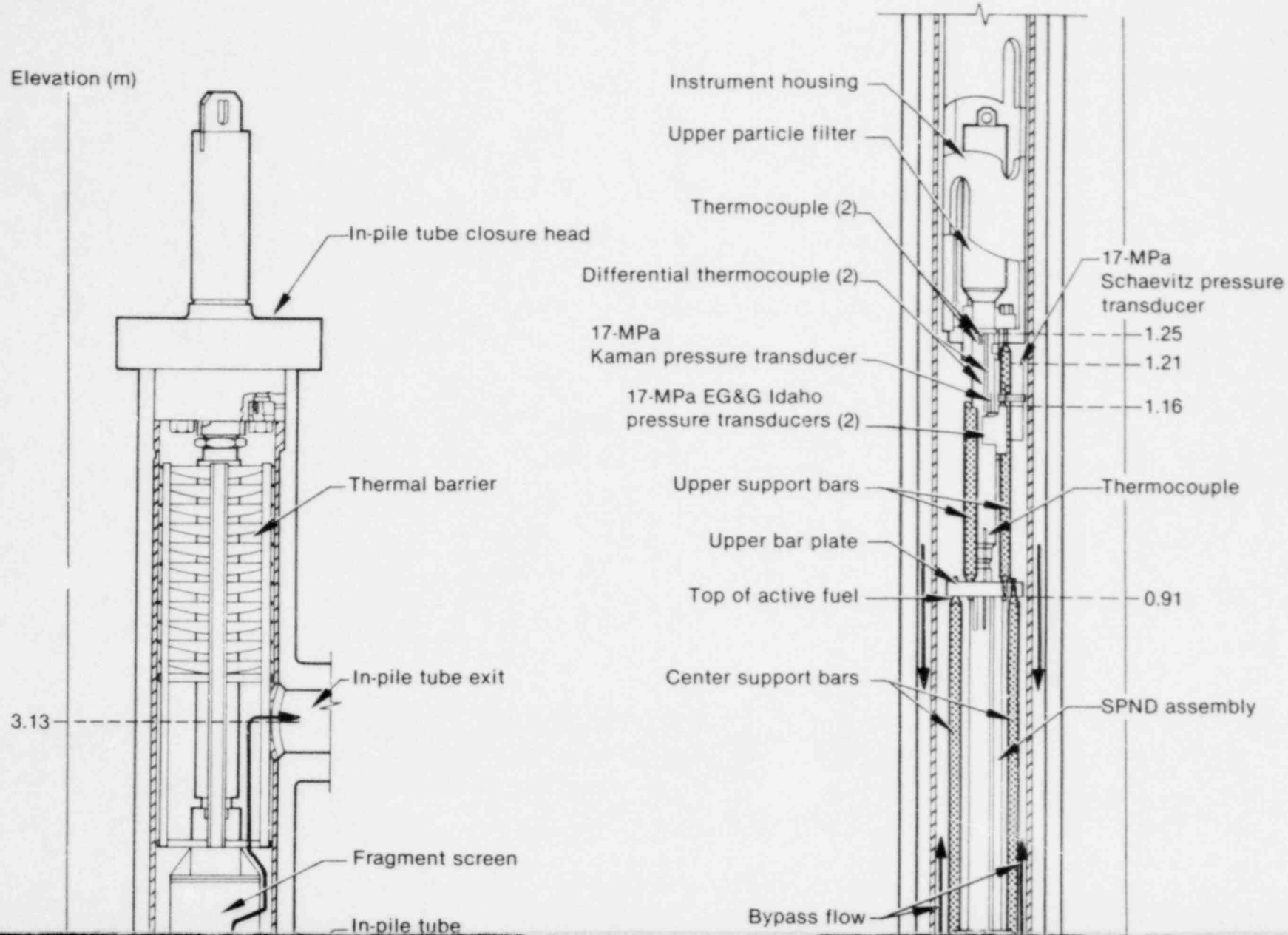
Elevation (m)
In-pile tube closure head
Thermal barrier
In-pile tube exit
3.13
Fragment screen
In-pile tube
Instrument housing
Upper particle filter
Thermocouple (2)
Differential thermocouple (2)
17-MPa Kaman pressure transducer
17-MPa EG&G Idaho pressure transducers (2)
Upper support bars
Upper bar plate
Top of active fuel
Center support bars
Bypass flow
17-MPa Schaevitz pressure transducer
1.25
1.21
1.16
Thermocouple
0.91
SPND assembly

the lower fuel rod shroud extension to measure the coolant flow rate at the test rod shroud inlet. Both flowmeters failed during the tests. One replacement was necessary.

8. Two pairs of EG&G Idaho stainless steel sheathed, magnesia insulated, Copper-Constantan (Type T) differential thermocouples were placed at the flow shroud inlet and outlet and connected to provide two independent measurements of the coolant temperature increase through the flow shroud. One of these was broken during a rod changeout.

9. Four EG&G Idaho stainless steel sheathed, magnesia insulated, Chromel-Alumel (Type K) thermocouples were installed; two at the inlet and two at the outlet of the flow shroud to measure coolant inlet and outlet temperatures. One inlet and one outlet thermocouple failed during the course of the tests.

10. One EG&G Idaho titanium sheathed, magnesia insulated, platinum-platinum, 10% rhodium (Type S) thermocouple was located on the outside of the fuel rod flow shroud for radiation sensitivity evaluation. It was connected only during RIA-ST-1.

11. Two EG&G Idaho linear variable differential transformers (LVDTs) were installed on the test train hardware. One was located in the lower flow shroud extension to measure fuel rod cladding displacement, but it failed prior to RIA-ST-1. Its housing was removed after completion of RIA-ST-2. The other LVDT, with a blocked armature, was located outside the flow shroud extension and was intended for radiation sensitivity evaluation.

12. Three Reuter-Stokes UC-2G cobalt self-powered neutron detectors (SPNDs) were located 0.229, 0.457, and 0.686 m above the bottom of the fuel stack array on a vertical support rod to measure the neutron flux at these elevations.

13. Two Ailtech strain gages, not shown in Figure 5, were located on the outside of the RIA-ST-1 test rod shroud for radiation sensitivity evaluation. One was mounted circumferentially and the other was mounted longitudinally.

14. One flux wire (0.51% cobalt and 99.49% aluminum wire for RIA-ST-1 and RIA-ST-4, and 100% cobalt wire for RIA-ST-2 and RIA-ST-3) was mounted on a reactor north orientation for each test.

Reactor core ionization chambers provided steady state and transient operating neutron flux information. They were sensitive to gamma and neutron radiation and produced current outputs proportional to the neutron and gamma flux that ionized the gas inside the chambers.

1. Two Westinghouse Electric Corp., nitrogen filled ionization chambers (TR-1 and TR-2), designed to measure power transients to 32 GW, were located outside the reactor core barrel.

2. Two Westinghouse Electric Corp., evacuated ionization chambers (EV-1 and EV-2), designed to measure high power transients to 200 GW, were located in the south and north corners of the reactor core support structure.

The remaining instrumentation used during the RIA Scoping Tests consisted of the coolant flow loop pressure transducers and the fission product detection system activity monitors. The test assembly and plant instrument data were recorded on the PBF Data Acquisition and Reduction System (PBF/DARS), the Surveillance System, and the Experiment and Analysis System.

3.4 Test Conduct

Table 4 summarizes the test procedures used for each single-rod test of the RIA Scoping Tests. Nuclear operation for each phase began after the coolant loop heatup and terminated immediately after the transient.

3.4.1 Power Calibrations and Fuel Rod Conditioning. Power calibrations were performed during RIA-ST-1 and RIA-ST-4 to calibrate the thermal-hydraulically determined test rod power with the reactor neutron detection chambers and the SPNDs mounted on the test train. The initial

TABLE 4. RIA SCOPING TESTS PLAN

RIA-ST-1	RIA-ST-2	RIA-ST-3	RIA-ST-4
Heatup	Heatup	Heatup	Heatup
Power calibration	Power burst (260 cal/g axial peak radial average fuel enthalpy; 290 cal/g peak fuel enthalpy; 350 cal/g UO_2 total energy deposition)	Power burst (225 cal/g axial peak radial average fuel enthalpy; 250 cal/g peak fuel enthalpy; 300 cal/g UO_2 total energy deposition)	Power calibration
Shutdown			Shutdown
Core flux wire change			Core flux wire change
Power calibration	Cooldown	Cooldown	Power burst (350 cal/g axial peak radial average fuel enthalpy; 530 cal/g peak fuel enthalpy; 695 cal/g UO_2 total energy deposition)[a]
Shutdown			
Core flux wire change			
Conditioning			
Shutdown			
Core flux wire removal			
Control rod worth check			
Trial transient			
Shutdown			
Core flux wire installation			

TABLE 4. (continued)

RIA-ST-1	RIA-ST-2	RIA-ST-3	RIA-ST-4
Power burst (185 cal/g axial peak radial average fuel enthalpy; 205 cal/g peak fuel enthalpy; 255 cal/g UO_2 total energy deposition)			
Core flux wire change			
Power burst (250 cal/g axial peak radial average fuel enthalpy; 275 cal/g peak fuel enthalpy; 335 cal/g UO_2 total energy deposition)			
Cooldown			

a. Axial peak radial average fuel rod enthalpy at the time of rod failure. Due to rapid heat transfer to the coolant upon fuel fragmentation, this is believed to be the peak radial average enthalpy.

coolant conditions for the power calibration were 538 K, 6.45 MPa, and 0.760 l/s. This temperature and pressure is representative of BWR hot-startup conditions. The flow rate was a factor of nine higher than the representative BWR hot-startup flow rate. The power calibration had to be performed at this elevated flow rate to avoid boiling transition. The test rod power was calculated from a thermal balance using measurements of coolant pressure, coolant inlet temperature, coolant temperature increase across the test rod shroud, and flow rate inside the test rod shroud. After each power calibration, the reactor was shut down and the core flux wire was replaced.

Fuel rod conditioning was performed during RIA-ST-1 to promote cracking and relocation of the fuel pellets and to build up the fission product inventory of the test rod for assurance of cladding failure indication by the fission product detection system during the transient testing. The conditioning phase consisted of four power cycles with coolant conditions again at 538 K, 6.45 MPa, and 0.760 l/s. During each cycle, the test rod peak power was increased slowly to about 52 kW/m and held constant for several minutes. Three of the power cycles were completed by a slow reduction of the test rod peak power to 3 kW/m, followed by steady state operation for several minutes. One cycle was terminated with a reactor scram. After completion of the fuel rod conditioning, the reactor was shut down, and the core flux wire was replaced.

3.4.2 Control Rod Worth Checks and Power Burst Testing Method. After the power calibration and fuel rod conditioning for RIA-ST-1, the control rods were calibrated against the transient rods by determining the control rod position required for reactor criticality with the transient rods inserted in the core to positions corresponding to reactivity worths of 0.75, 1.5, and 1.75$. A reactivity meter was used to measure the reactivity worth of the transient rods during their insertion. A trial power burst (1.7-s period, 13 MW peak power) was performed for the 0.75$ reactivity measurement to verify the control and transient rod worth measurements indicated by the reactivity meter. The accuracy of the reactivity meter measurements ($\pm$0.10$) proved to be inadequate, and PBF reactivity curves from previous lead rod tests were used to determine the control and transient rod positions for the subsequent power bursts.

Five power bursts were performed during the RIA Scoping Tests. A reactivity balance method was used to initiate each power burst. This method provides assurance that the control and transient rods have not been grossly malpositioned and no potentially dangerous reactivity addition has been made. The reactivity balance method included the following sequence of events, which is also graphically displayed in Figure 6.

1. The control rods were withdrawn from their scram positions (Figure 6a) until a reactor transient period of about 10 s was achieved. Then, the reactor power was increased until a reactor console panel light indicated the plant protection system was operating correctly. Immediately after verification that the plant protection system was operating, the control rods were inserted until the reactor was subcritical.

2. From that position, the control rods were slowly withdrawn until criticality was acheived at about 100 W and the low power critical position of the control rods was determined (Figure 6b).

3. The transient rods were inserted into the core to a position calculated to be worth a negative reactivity equivalent to the reactivity insertion required for the power burst (Figure 6c).

4. The control rods were then adjusted to the withdrawal position corresponding to the calculated increment for the desired reactivity insertion (Figure 6d). The control rod withdrawal increment was checked with the transient rod insertion increment to ensure that a gross error in the calculation of the required control rod increment had not been made.

5. The transient rods were fully inserted into the core (Figure 6e), leaving the control rods in a position corresponding to a calculated reactivity increment above the low power critical position that was equivalent to the reactivity insertion desired.

6. To initiate the power burst, all four transient rods were ejected at a velocity of

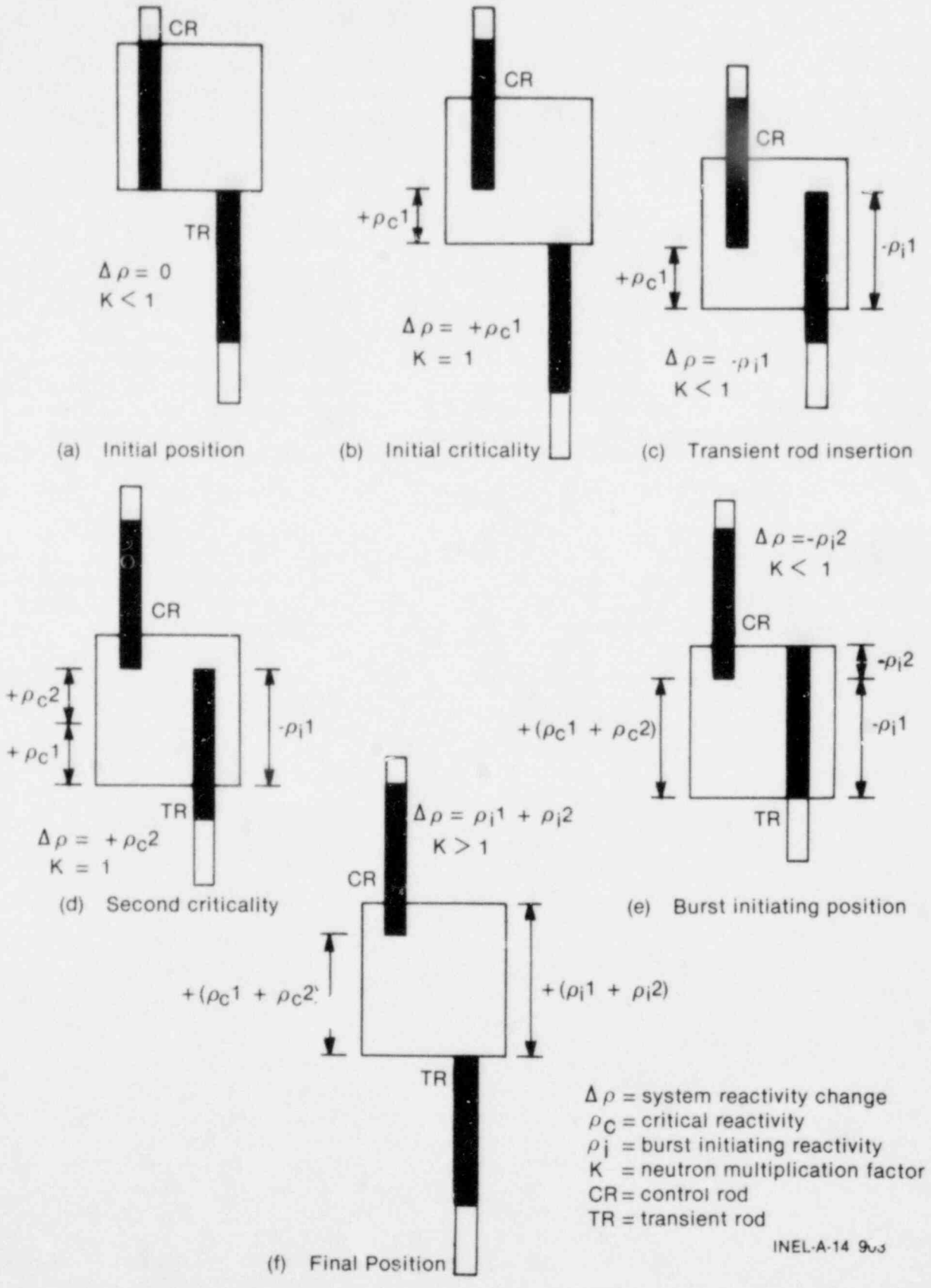

Figure 6. Power burst testing sequence.

about 9.5 m/s (Figure 6f). The burst was largely self-terminating because the PBF driver core and fuel were designed for a Doppler reactivity feedback capable of terminating the burst without primary dependence on mechanical systems.

7. All eight control rods were then completely inserted into the driver core to provide mechanical shutdown of the reactor.

3.5 Description of Power Bursts

The RIA-ST power bursts included two bursts during RIA-ST-1 and one burst each for RIA-ST-2, RIA-ST-3, and RIA-ST-4. The coolant conditions for each transient were nominally 538 K, 6.45 MPa, and 0.085 l/s, which are representative of BWR hot-startup conditions. The test rod peak fuel enthalpy data for the five power bursts are summarized in Table 5. Fuel rod failure occurred in RIA-ST-1, RIA-ST-2, and RIA-ST-4. A brief discussion of the power burst results is given below.

3.5.1 RIA-ST-1 Power Bursts. An axial peak radial average fuel enthalpy of 185 cal/g (205 cal/g peak fuel enthalpy near the pellet surface) was achieved in the first power burst (PB-1) of RIA-ST-1. This axial peak radial average fuel enthalpy corresponds to a total radial average energy deposition of 250 cal/g UO_2. No indication of fuel rod failure was observed. The second power burst of RIA-ST-1 (PB-2) resulted in an axial peak radial average fuel enthalpy of 250 cal/g (275 cal/g peak fuel enthalpy), corresponding to a total radial average energy deposition of 330 cal/g UO_2. The fuel rod failed. The first indication of fuel rod failure was observed, approximately 360 s following the power burst, on a plant radiation monitor located near the test loop piping in the basement of the reactor building. Rod failure was indicated by a sharp increase in the indicated radiation field. Failure was also indicated about 60 s later by the fission product detection system. None of the pressure transducers indicated the time of rod failure (indicating that no pressure pulse was generated); therefore, the exact time is uncertain due to the long time necessary for coolant to flow from the fuel rod to the radiation monitor locations.

TABLE 5. RIA SCOPING TESTS SUMMARY

Transient Number	Reactor Period (ms)	Axial Peak Radial Average Fuel Enthalpy[a] (cal/g)	Peak Fuel Enthalpy[a] (cal/g)	Total Radial Average Energy Deposition (cal/g UO_2)	Rod Failure
RIA-ST-1, PB-1	5.7	185	205	250	NO
RIA-ST-1, PB-2	4.4	250	275	330	YES
RIA-ST-2	4.6	260	290	345	YES
RIA-ST-3	5.2	225	250	300	NO
RIA-ST-4	3.85	350	530	695	YES

a. Best-estimate peak fuel enthalpies obtained, accounting for heat transfer from the fuel during the burst. The value for RIA-ST-4 corresponds to the calculated fuel enthalpy at rod failure.

3.5.2 RIA-ST-2 Power Burst. The RIA-ST-2 fuel rod was exposed to a single power burst, with no significant steady state operation. The axial peak radial average fuel enthalpy achieved from this single power burst, 260 cal/g (peak fuel enthalpy of 290 cal/g and total radial average energy deposition of 345 cal/g UO_2), resulted in fuel rod failure. The loop monitor indicated the failure after about 420 s, and the fission product detection system after about 450 s. Again, as in RIA-ST-1, none of the test train pressure transducers responded to the failure.

3.5.3 RIA-ST-3 Power Burst. The RIA-ST-3 fuel rod was subjected to a single power burst and achieved an axial peak radial average fuel enthalpy of 225 cal/g (peak fuel enthalpy of 250 cal/g and total radial average energy deposition of 300 cal/g UO_2). The rod did not fail.

3.5.4 RIA-ST-4 Power Burst. Following the power calibration for RIA-ST-4, the fuel rod was subjected to a single power burst which resulted in an axial peak radial average fuel enthalpy of 350 cal/g (peak fuel enthalpy of 530 cal/g and total radial average energy deposition of 695 cal/g UO_2) at the time of rod failure. A power transient of this magnitude is not considered to be possible in a commercial power reactor. As expected, this large energy deposition resulted in immediate fuel rod failure. A large pressure pulse (28.2-MPa increase) was recorded by the 69-MPa EG&G Idaho pressure transducer connected to the lower end of the flow shroud. The Bell & Howell pressure transducer, connected by means of a small-diameter tubing to the flow shroud at the axial flux peak elevation, indicated a pressure pulse (22.3 MPa total) that exceeded the 17-MPa rating of the transducer. The time of the pressure increase was about 3 ms after the time of peak power. Further discussion of the pressure pulse detected during RIA-ST-4 can be found in the section titled, "Consequences of Very High Energy Deposition in a Liquid Filled System (RIA-ST-4)." The fission product detection system indicated rod failure about 195 s after the power burst. The loop radiation monitor indicated rod failure within 120 s after the power burst.

4. TRANSIENT ENERGY DEPOSITION MEASUREMENTS

The first objective of the RIA Scoping Tests was to evaluate proposed methods for determining the energy deposition of the test rods during a PBF power burst. Previous power burst energy measurements for closed-capsule RIA tests performed at CDC and TREAT were based on calibrating the activation of a neutron flux monitor with radiochemical analysis of fuel rod samples irradiated during very low power steady state operation or during a low energy power burst. The activation of another flux monitor irradiated during the high energy power burst was then used to determine the fuel rod energy during high energy power bursts. Radiochemical burnup analysis of fuel samples irradiated during the high energy power bursts usually was not possible due to failure over the entire 127-mm length of the fuel rods. The CDC and TREAT energy data were reported in terms of total energy deposited during and after the power burst.[a] However, the test fuel rod and flux monitor remained in the reactor for several hours after each power burst, and the total fissions of the test fuel rod and the activation of the flux monitors included delayed neutron flux, which does not significantly affect rod behavior.

During a PBF RIA test, the reactor is operated in a natural burst mode in which a rapid increase in the core reactivity results in a large, rapid increase in the reactor power up to 100 000 MW. The power burst is self-terminated by Doppler reactivity feedback, without primary dependence on mechanical shutdown systems. A typical PBF power burst, shown in Figure 7, has a half-width of approximately 18 ms. Control rod scram initiation occurs about 70 ms after the reactor power peaks. The prompt neutron energy deposition during the actual power burst is followed by an extended period (several minutes) of delayed neutron depostion caused by the release of delayed neutrons into the subcritical PBF core after the control rods are scrammed to terminate the power burst. The delayed component of the deposited energy can be as much as 25% of the total energy.

For the PBF RIA tests, the unique capabilities of the facility (high steady state power, test loop with flow capabilities, and relatively long test rods) allowed the use of different techniques to measure power burst fuel energy than were possible with the previous closed-capsule RIA tests conducted at CDC, TREAT, and NSRR. Intercalibration of the calorimetrically measured fuel rod power with core chambers and SPNDs was performed at reactor powers up to about 22 MW. The output of the core power chambers and the SPNDs during a power burst was then used to determine the power burst test fuel rod energy. Since the test fuel rods were relatively long, radiochemical burnup analysis of fuel samples above and below the failed central region of the test rods was possible. Flux wire data calibrated with steady state fuel burnup were also used to measure power burst fuel energies, similar to the previous CDC and TREAT tests.

The NRC Regulatory Guide 1.77 licensing criteria for an RIA event limits the calculated axial peak radial average fuel enthalpy to 280 cal/g for power reactors.[2] The axial peak radial average fuel enthalpy is defined as the maximum radially averaged UO_2 enthalpy attained at the fuel rod axial flux peak during the power burst. Probably the most important parameter to fuel rod behavior during an RIA event is the peak fuel enthalpy near the fuel pellet surface, as this controls heat transfer from the fuel to the cladding and the resulting cladding temperature. The peak fuel enthalpy is defined as the maximum radial enthalpy attained at the fuel rod axial flux peak during the power burst. The FRAP-T5[b] computer code was used to determine the axial peak radial average and peak fuel enthalpies for the RIA Scoping Tests from the measured total energy depositions. For the PBF tests, the axial peak radial average and peak fuel enthalpies occur about 65 to 115 ms after the reactor power peaks.

4.1 Energy Measurement Methods

Five different methods were used for measuring the total radially averaged fission energy deposited in the RIA Scoping Tests fuel rods. These methods

a. The total fuel energy is defined as the integrated, radially averaged power produced per gram of UO_2 at the fuel rod axial flux peak from the initiation of the power burst until the rod is removed from the reactor, plus the energy equivalent to the initial fuel temperature.

b. FRAP-T5 (Fuel Rod Analysis Program-Transient) is the INEL fuel performance code. FRAP-T5, Version FL 1010, Configuration Control Number H000183B, was used for this study. See Appendix B, "FRAP-T5 Models and Input."

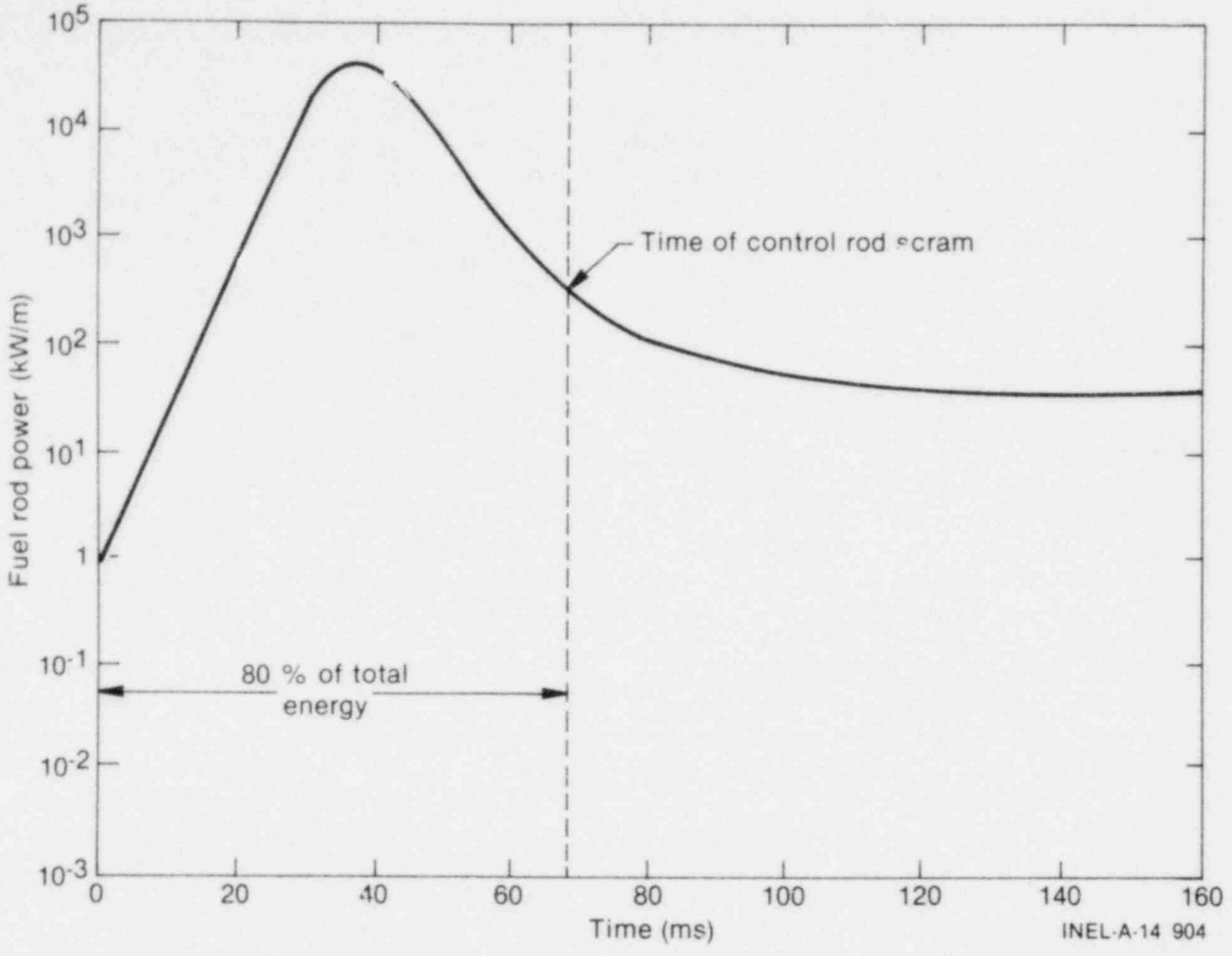

Figure 7. Typical PBF power burst time history.

are described and evaluated in the following subsections. The results of the energy measurements and the fuel enthalpy calculations are given, along with the estimated uncertainity associated with each measurement.

4.1.1 Method 1: Core Chambers. The indicated reactor power from uncompensated neutron detection chambers located on the periphery of the PBF core was related to the calorimetrically measured test rod power during steady state reactor operation. The ratio of test rod power to PBF reactor power was evaluated at the same control rod position that was used for initiating the power burst, since the ratio of test rod power to reactor power is slightly dependent on control rod position. The ratio of test rod power to reactor power was used to convert the measured power burst reactor energy to test rod energy deposited during the power burst up to the time of control rod scram. Appropriate values of energy per fission during steady state (183.8 MeV/f) and power burst operation (172.1 MeV/f) were included to account for the absence of delayed neutron and gamma radiation during the power burst. Reactor physics computer codes (SCAMP, SINBAD, GAMSOR, and QAD)[a] were used to calculate the neutron, gamma, and beta contribution to the energy absorbed per fission. The contribution of beta and delayed gamma radiation to heating in the power burst was neglibible, accounting for less than 0.1% of the total heating.

The core chamber output could not be used to determine the test fuel rod energy after the time of control rod scram because the reactor power decreased to very low levels. Reactor physics calculations using the TWIGL computer code[b]

a. SCAMP Configuration Control Number H000291B
SCAMP Configuration Control Number H001251B
SINBAD Configuration Control Number H006931B
GAMSOR Configuration Control Number H003451B
QAD Configuration Control Number H003461B.

b. TWIGL Configuration Control Number H009971B.

were therefore made to determine the fraction of energy generated by delayed neutrons after control rod scram. TWIGL solves the coupled time- and space-dependent neutron diffusion and thermal-hydraulic equations for a reactor in two dimensions, with rectangular geometry. The results of these calculations are given in Table 6.

The fraction of the total fuel energy deposited after scram was larger than the fraction of total fissions occurring after scram because the energy after scram includes a delayed contribution from the prompt portion of the actual power burst, in addition to the energy generated after scram due to delayed neutron multiplication.

4.1.2 Method 2: SPNDs. The outputs of cobalt self-powered neutron detectors (SPNDs) located on the test train were related to the calorimetrically measured test rod power during steady state operation. The ratio of test rod power to SPND output was evaluated at the same control rod position that was used for initiating the power burst. This ratio was used to convert the integrated SPND output to test rod energy deposited during the power burst up to control rod scram. Appropriate values of energy per fission during steady state and power burst operation were included. The SPNDs had cobalt emitters and Inconel sheaths. The detectors were sensitive to both neutron and gamma fluxes; the output current from the emitter being positive for neutron flux and negative for gamma flux. Since no delayed gammas were present during the power burst, a correction factor of 0.95 was included to account for the relative increase in the output of the SPNDs during the power burst. This correction factor was calculated from the neutron and gamma sensitivites of the SPNDs and the ratio of neutron-to-gamma flux in the PBF in-pile tube. The correction factor was less than unity because the gamma-induced output current of an SPND is negative with respect to the neutron-induced current. The delayed gamma flux amounted to about 40% of the total gamma flux during steady state operation.

The SPND output could not be used to determine the test fuel rod energy after control rod scram because the ratio of neutron-to-gamma flux continually changes after the power burst. The same correction factors for the energy deposited after control rod scram, discussed earlier for the core chamber data, were used to adjust the SPND data to obtain the total fuel energy deposition.

4.1.3 Method 3: Shroud Flux Wires. Cobalt flux wires were mounted on the flow shroud surrounding each fuel rod. Neutron activation of the cobalt wires was related to the radiochemically determined burnup of the RIA-ST-1 fuel rod. Over 99% of the total activation of the RIA-ST-1 fuel rod was due to the steady state portion of the test, and less than 1% of the total activation was due to power bursts. The ratio of the RIA-ST-1 shroud wire fluence to test rod burnup was used to convert the fluence, measured during the power bursts of RIA-ST-2 and RIA-ST-3, to test rod power burst energy. A reactor power of about 120 kW was required to verify that the core power chambers were operating properly before each power burst was performed. A correction factor of ~8 cal/g UO_2 was applied to account for the energy produced during the low power nuclear operation involved in checking the core power chambers and in determining criticality just prior

TABLE 6. RESULTS OF REACTOR PHYSICS CALCULATIONS FOR ENERGY DEPOSITION AFTER SCRAM

Power Burst Designation	Fraction of Total Fissions Occurring after Scram	Fraction of Total Fuel Energy Deposited after Scram
RIA-ST-1, PB-1	0.15	0.193
RIA-ST-1, PB-2	0.147	0.190
RIA-ST-2	0.148	0.191
RIA-ST-3	0.152	0.195

to conducting each power burst. This correction factor was obtained by integrating the SPND outputs during nuclear operation just prior to conducting each power burst. The integrated SPND output was converted to fuel rod energy using the ratio of test rod power to SPND output determined during the power calibration phase.

4.1.4 Method 4: Core Flux Wires. The activation of a cobalt flux wire (located in a holder on the periphery of the PBF reactor core) during the steady state portion of the test was related to the radiochemical burnup analyses of the RIA-ST-1 fuel rod. The ratio of RIA-ST-1 core flux wire fluence to RIA-ST-1 rod burnup was used to convert the fluence measured during the power bursts of RIA-ST-1, RIA-ST-2, and RIA-ST-3 to test rod power burst energy. The same correction factors discussed for Method 3 were applied.

4.1.5 Method 5: Burnup Analyses. Fuel samples from the RIA-ST-2 and RIA-ST-3 fuel rods, which were irradiated only during the low power criticality check and one power burst, were radiochemically analyzed to determine the fissions per gram of uranium. These data were converted to total power burst test rod energy by correcting for the energy generated during the low power criticality check (~8 cal/g UO_2) and applying the appropriate energy per fission values determined from reactor physics calculations. Independent radiochemical burnup measurements were performed by the Allied Chemical Corporation at the INEL and by the Hanford Engineering Development Laboratory at Richland, Washington.

4.2 Evaluation of Measurement Methods

The results of the five measurement methods are summarized in Table 7. These data represent the evaluated total radial average fission energy deposited at the axial flux peak of the test rods. The evaluations of the five energy measurement methods are discussed in the following paragraphs.

4.2.1 Method 1: Core Chambers. The accuracy of test fuel rod energies determined from core power chamber data depends primarily on the accuracy of the calorimetrically determined fuel rod power during the power calibration phase of the test and the linearity of the core chambers and associated electronics during the power burst. A study of the contributing error sources involved with steady state calorimetric measurements for tests prior to the RIA Scoping Tests identified a typical uncertainty in calorimetrically measured fuel rod power of ±6%. The calorimetric measurement of steady state fuel rod power can lead to larger errors if larger systematic or random errors are present.

Since the reactor power varies from about 22 MW during the steady state power calibration to peak powers of 25 000 MW during a power burst, slight errors in chamber linearity and associated electronics will affect the results. The four core power chambers are designated TR-1, TR-2, EV-1, and EV-2. Chambers TR-1 and TR-2 are of the same design and are located equidistant from the center of the core. The calculated steady state outputs from Chambers TR-1 and TR-2 have a 0.2% neutron component, a 96.7% prompt gamma component, and a 3.1% delayed gamma component. Chambers EV-1 and EV-2 are of a different design than chambers TR-1 and TR-2 and are located much closer to the center of the core. The calculated equilibrium steady state currents for Chambers EV-1 and EV-2 consist of a 98.3% neutron component, a 1.6% prompt gamma component, and a 0.1% delayed gamma component. Measurements of the reactor power and energy during a power burst with Chambers TR-1 and TR-2 were corrected by 3.1% to account for the absence of delayed gammas during a power burst, whereas measurements with Chambers EV-1 and EV-2 did not require correction because the delayed gamma component was negligible.

Since the two types of chambers have different neutron and gamma sensitivities, chamber linearity was evaluated by plotting the chamber output at the time of peak power for Chambers TR-1 and TR-2 as a function of the output of Chambers EV-1, as shown in Figure 8, and EV-2 as shown in Figure 9, during power burst core qualification tests prior to the RIA Scoping Tests. The linearity of the data points in Figures 8 and 9 indicates that the chambers are linear with respect to each other. This linearity of data points is also good evidence that the chambers are linear in their response to the power burst radiation. The data in the figures would also be linear if both sets of chambers were becoming nonlinear at the same rate, but it is improbable that the chambers would become nonlinear at the same rate. The four core

RIA SCOPING TESTS POWER BURST ENERGY DEPOSITION DATA

Test Phase	Total Axial Peak, Radially Averaged Fuel Rod Energy Deposition ($cal/g\ UO_2$)[a]					
					Burnup Analyses	
	Core Chamber	SPND	Shroud Flux Wire	Core Flux Wire	Allied Chemical Corporation	Hanford Engineering Development Laboratory
RIA-ST-1, PB-1	250	b	--	250	--	--
RIA-ST-1, PB-2	335	b	--	315	--	--
RIA-ST-2	330	b	320	325	380	355
RIA-ST-3	280	b	275	275	325	290
RIA-ST-4	650	725	--	720	--	--

a. Total energy deposition during and after power burst.

b. Data questionable.

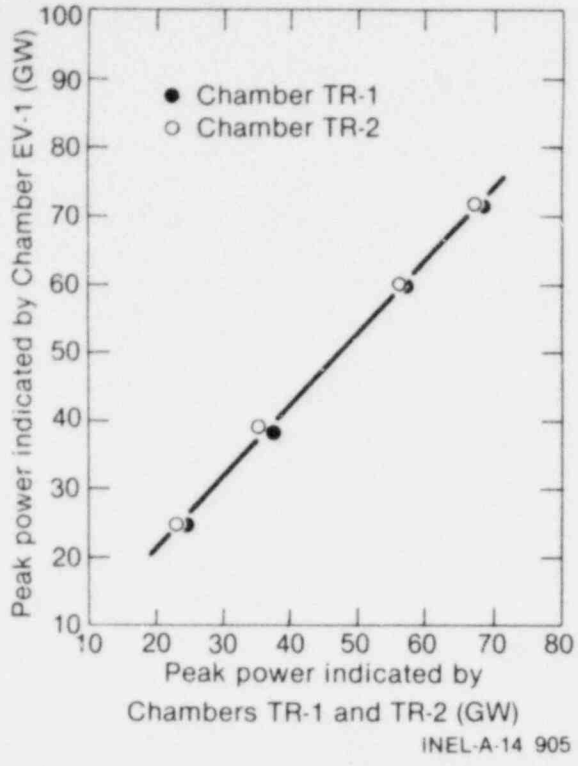

Figure 8. Peak power indicated by power Chambers TR-1 and TR-2 plotted against peak power indicated by Chamber EV-1 to illustrate chamber linearity.

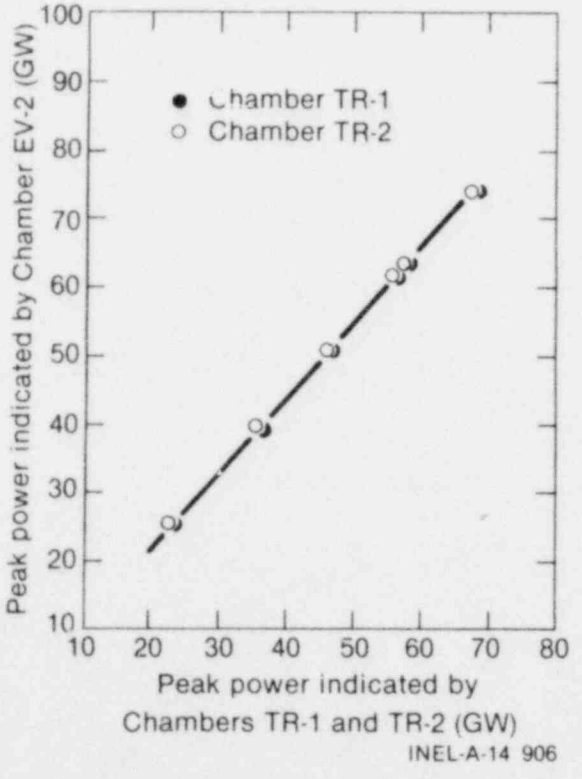

Figure 9. Peak power indicated by power Chambers TR-1 and TR-2 plotted against peak power indicated by Chamber EV-2 to illustrate chamber linearity.

power chambers, although linear, indicated reactor powers with a spread of ±10%. This spread is primarily caused by inaccurate calibration of the chambers with the PBF/Data Acquisition and Reduction System (DARS). Because of this ±10% spread in reactor power chamber outputs, an uncertainty of ±10% exists (associated with core chamber reactor power measurement) in the determination of test rod energy.

Another source of uncertainty in the determination of test rod power from the core chamber data is the calculation of the correction factor for fission energy due to delayed neutron radiation generated after control rod scram (Table 6). A ±2% uncertainty is associated with this TWIGL code calculation.

When the three components of uncertainty discussed previously for the determination of test rod power from core power chamber data are combined through use of the square root of the sum of the squares approach, an overall uncertainty of ±12% is obtained.

4.2.2 Method 2: Self-Powered Neutron Detectors. Fuel rod energy values based on the cobalt SPND data rely on the same calorimetric power measurements used in Method 1; therefore, a ±6% uncertainty component for calorimetric determination of rod power exists. In addition, the output of a cobalt SPND during equilibrium steady state operation is composed of prompt and delayed neutron, and prompt and delayed gamma components. The polarity of the gamma-induced output current for a cobalt SPND is the opposite of the neutron-induced output current. The output of an SPND for a given neutron flux is, therefore, higher during a power burst than during steady state operation due to the absence of a delayed gamma flux during the power burst. The SPND outputs during each power burst were adjusted by a calculated correction factor of 0.95 to account for the absence of delayed gammas during the power burst. The uncertainty in the calculation of this correction factor is ±2%.

As discussed in the evaluation of the core chamber data, another source of uncertainty exists; the calculation of a correction factor for fission energy due to delayed neutron radiation generated after control rod scram (Table 6). The uncertainty of this TWIGL calculation is ±2%.

Eight-decade logarithmic amplifiers are connected to each SPND. Problems were encountered

in accurately calibrating the SPND data channels due to drifting of the data system electronics during RIA-ST-1, RIA-ST-2 and RIA-ST-3. Since the logarithmic amplifiers cover eight decades of SPND output, small drifts in the data system electronics lead to relatively large errors in the indicated SPND output current. Because of the electronics problems, the fuel energy values based on SPND measurements for RIA-ST-1, RIA-ST-2, and RIA-ST-3 were disregarded in the evaluation of the best estimate of the fuel energy. Since the RIA-ST-4 burst was performed within a few hours following the steady state operation, the drift problem was not as critical. The uncertainty due to the logarithmic behavior of the SPND amplifies and the drift in the data acquisition system electronics is estimated to be ±12%.

The overall uncertainty for the RIA-ST-4 fuel energy determined from the SPND data, based on the square root of the sum of the squares approach to combining the uncertainty components, is ±14%.

4.2.3 Method 3: Shroud Flux Wires. Possible uncertainties related to the shroud flux wire method include:

1. The neutron spectrum may be different during a power burst than during steady state operation. According to reactor physics TWIGL computer code calculations, this error is negligible.

2. Since the ratio of thermal neutron to resonance neutron activation of cobalt is different than the ratio of thermal neutron to resonance neutron fission of ^{235}U, the ratio of cobalt-measured nvt values during steady state operation and during a power burst may be different. This error has not been measured, but is estimated to be ±4%.

3. The flux wire results were normalized to the radiochemical analyses of the RIA-ST-1 fuel rod. According to the Allied Chemical Corporation and the Hanford Engineering Development Laboratory, where the radiochemical analyses were done, there is an uncertainty of ±10% in the radiochemical analyses results.

4. The uncertainty in measuring the activation of the flux wires is about ±4%. This includes uncertainty in physical constants, detector calibration, counting statistics, the cobalt content of the wires, and the contribution of impurities in the wire.

5. A potential exists for positioning errors in relating the axial location of the flux wire to the location of the fuel stack in the rods. The uncertainty of flux wire position represents an estimated ±3% uncertainty in the fuel energy measurement.

The overall accuracy of the shroud flux wire fuel energy data, obtained by combining all of the uncertainties discussed previously, is ±12%.

4.2.4 Method 4: Core Flux Wires. The same uncertainties associated with the shroud flux wire measurements are present in the core flux wire data. In addition, the core flux wires are located on the periphery of the core where the relative neutron flux is a factor of ten lower than in the IPT where the shroud flux wires were located. This causes the uncertainty in measuring the flux wire activation discussed in the previous subsection to increase to ±5%.

Combining all the components of uncertainty, however, again establishes the overall accuracy of the core flux wire fuel energy data to be ±12%.

4.2.5 Method 5: Burnup Analyses. Possible uncertainties in determining test rod energy during a power burst from the radiochemical burnup analyses data include:

1. Contamination of fuel samples subjected to only a power burst may occur during sectioning and handling in the hot cell when higher burnup samples are also present, since the activation of fuel rods irradiated only during a power burst is much less than the activation during steady state operation. This problem was obvious from the burnup analyses results for several fuel samples. Results from these obviously contaminated fuel samples were rejected, and improved sample preparation techniques were implemented for later analyses. The uncertainty in radiochemically determined fuel energy due to contamination is about ±5% for the first set of samples and negligible for the later analyses.

2. There are potential errors in accurately cutting a sample from a specified section of a fuel rod, errors in the relative location of a fuel rod and the shroud flux wire, and errors in scanning the flux wire. These errors represent an estimated ±5% error in the evaluated fuel energy.

3. The radiochemical analysts (Allied Chemical Corporation and Hanford Engineering Development Laboratories) estimate the uncertainty in the radiochemical burnup analyses to be ±10%.

The overall estimated uncertainties in the burnup analyses, obtained by combining the uncertainty components, are ±12% for the first samples, which were possibly contaminated, and ±11% for the later samples obtained using improved preparation techniques. Fuel burnup analyses of a fuel rod exposed to only a power burst appears to be the best method of measuring the total adiabatic fuel energy during a power burst. The other methods must rely on thermal-hydraulic calorimetric measurements of the fuel rod power during steady state operation and, therefore, must be interrelated with other instruments to measure the fuel rod energy during a power burst. The burnup analyses method has the disadvantage of being limited to previously unirradiated fuel rods or to previously irradiated fuel rods with low residual activity for the fission product isotope used in the analyses.

4.2.6 Summary of Energy Measurement Methods. Best estimates of the energy depositions, obtained by averaging the results of the specific measurement methods, and the standard deviations are summarized in Table 8. The SPND data for RIA-ST-1, RIA-ST-2, and RIA-ST-3 were rejected because of electronics problems. Burnup analyses data of fuel samples that were suspect due to probable gross contamination were also disregarded.

The five energy measurement methods had estimated uncertainties ranging from ±11 to ±14%. Detailed independent review of the methods confirmed that none were unreliable. The standard deviation for the best-estimate energy deposition values (Table 8), obtained from a comparison of the results of the five methods, varies from 4 to 9% for the five power bursts. Fuel burnup analyses of a fuel rod exposed only to the power burst is considered to be the best method for measuring the total fuel energy deposition. The other methods must rely on calorimetric measurements of the fuel rod power during steady state operation and, therefore, must be interrelated with other instruments to measure the fuel rod energy during a power burst.

4.3 Fuel Enthalpy Results

The NRC licensing criteria for the acceptable analysis of an RIA event states that, "reactivity excursions will not result in a radial average fuel enthalpy greater than 280 cal/g (1170 J/g) at any axial location in any fuel rod."[2] Thus, axial peak radial average fuel enthalpy is an important RIA variable. In addition, peak fuel enthalpy near the fuel pellet surface is very important in terms of fuel rod cladding damage. Since, in both cases, enthalpy is the limiting parameter, allowance must be made for heat transfer from the fuel to the cladding and reactor coolant during the RIA power transient. Since direct measurement of fuel enthalpy during a power burst is impractical, the FRAP-T5 computer code was used to account for heat transfer in determining peak fuel enthalpies for the RIA Scoping Tests. Since gap closure is abrupt in RIA transients, the potential gap conductance uncertainty was minimized. The best-estimate measured total energy deposition was used as input to the FRAP-T5 code. These calculations are described in detail in Appendix B. (The appendixes to this report are provided on microfiche attached to the inside of the back cover.)

Approximately 80% of the total fuel rod energy deposition occurs before the control rods scram, ~70 ms after peak power is reached. The peak fuel enthalpy occurs about 65 to 115 ms after peak power is reached. Axial peak radial average fuel enthalpy is about 10% less than the total energy deposited before the control rods scram. It is about 25% less than the total fuel energy deposited. Peak fuel enthalpy near the fuel pellet surface is higher than axial peak radial average fuel enthalpy and is primarily dependent on the radial power profile of the fuel rod.

Best estimates of the peak fuel enthalpies for each power burst are listed in Table 9. The estimated uncertainty in calculating the peak fuel

TABLE 8. BEST-ESTIMATE FUEL ENERGY DEPOSITION SUMMARY

Test	Total Radial Average Fuel Energy Deposited (cal/g UO_2)	Standard Deviation		Number of Measurements
		(± cal/g UO_2)	(±%)	
RIA-ST-1, PB-1	250	10	4	5
RIA-ST-1, PB-2	330	15	5	5
RIA-ST-2	345	30	9	10
RIA-ST-3	300	25	9	12
RIA-ST-4	695	45	7	7

TABLE 9. BEST-ESTIMATES OF ENERGY DEPOSITION AND PEAK FUEL ENTHALPY

Test	Total Radial Average Fuel Energy Deposited (cal/g)	Calculated Axial Peak Radial Average Fuel Enthalpy (cal/g)	Axial and Radial Peak Fuel Enthalpy (cal/g)
RIA-ST-1, PB-1	250	185	205
RIA-ST-1, PB-2	330	250	275
RIA-ST-2	345	260	290
RIA-ST-3	300	225	250
RIA-ST-4	695	350[a]	530[a]

a. Fuel enthalpy at time of rod failure. Since fuel rod melting and fragmentation occurred about 3 ms after the time of peak power, peak fuel enthalpy cannot be calculated. Due to the rapid heat transfer from the fuel at failure, this value is possibly the peak fuel enthalpy.

enthalpies is ±5%. The RIA-ST-4 fuel rod failed about 3 ms after the time of peak power, and the total fuel energy deposited by the time of failure was about 365 cal/g UO_2. The FRAP-T5 calculated axial peak radial average fuel enthalpy at this time was 350 cal/g. The failure of this rod was severe and entailed extensive fuel fragmentation. The heat transfer from the fragmented fuel to the coolant was extremely rapid, as evidenced by the large pressure pulse detected at this time (3 ms after the power burst). The fuel enthalpy at rod failure was probably the peak value because of the magnitude of heat transfer from the fuel after failure. The RIA-ST-4 transient is discussed in more detail in the section titled, "Consequences of Very High Energy Deposition in a Liquid Filled System (RIA-ST-4)." The rod failures during RIA-ST-1 and RIA-ST-2 probably occurred after the control rods scrammed, so the peak fuel enthalpy values for these test phases are not influenced by rod failure.

The total uncertainty in the calculated peak fuel enthalpies is estimated at ±13%. This includes an uncertainty of ±12% for the determination of total energy deposition and ±5% for the FRAP-T5 calculation. The fuel rod failures during RIA-ST-1 and RIA ST-2 occurred for calculated axial peak radial average fuel enthalpies of 250 and 260 cal/g; less than the 280 cal/g NRC licensing limit. It should be noted that the NRC licensing criteria was intended to minimize the possibility of a core disruptive event or a core coolability problem due to fuel fragmentation. Fuel rod cladding failure was acknowledged to occur at a lower value.

5. FAILURE THRESHOLD OF UNIRRADIATED LWR FUEL RODS

The second objective of the RIA Scoping Test was to determine a peak fuel enthalpy failure threshold for previously unirradiated test fuel rods tested at BWR hot-startup conditions. This section reviews and contrasts the results of RIA-ST-1 and RIA-ST-2, with axial peak radial average fuel enthalpies of 250 and 260 cal/g (275 and 290 cal/g peak fuel enthalpies near the pellet surface) and rod failures, with the results of RIA-ST-3, which had an axial peak radial average fuel enthalpy of 225 cal/g (250 cal/g peak fuel enthalpy near the pellet surface) and no failure. The purpose of the comparison is to establish the failure threshold in terms of axial peak radial average and peak fuel enthalpies. The comparison also serves to contrast the fuel damage produced just beyond and prior to this failure threshold. The section titled "Consequences of Very High Energy Deposition in a Liquid Filled System (RIA-ST-4)" will review the consequences of energy insertions resulting in peak enthalpies substantially greater than the failure threshold.

This section begins with an overview of the fuel rod damage during RIA-ST-1, RIA-ST-2, and RIA-ST-3 and the identification of the failure threshold axial peak radial average and peak fuel enthalpies. The overview is followed by two subsections which address in detail the fuel rod damage and damage mechanisms in RIA-ST-1 and RIA-ST-2 (with axial peak radial average fuel enthalpies of 250 and 260 cal/g and peak fuel enthalpies of 275 and 290 cal/g, respectively), and RIA-ST-3 (with an axial peak radial average fuel enthalpy of 225 cal/g and a peak fuel enthalpy of 250 cal/g). Finally, a summary of the RIA-ST postirradiation examinations is provided; the details are presented in Appendix C (provided on microfiche attached to the inside of the back cover).

5.1 Overview of Rod Damage and Identification of the Failure Threshold

The posttest appearances of the RIA-ST-1, RIA-ST-2, and RIA-ST-3 fuel rods are shown in Figure 10 and described in Table 10. Visual examination of the rods revealed extensive cladding reaction and deformation, including oxide spalling and cladding collapse, fracture, and crumbling. The intact portions of the failed fuel rods and the unfailed RIA-ST-3 rod revealed that cladding oxidation occurred over 95% of the fuel stack length, indicating that film boiling extended over essentially the entire fuel rod length in all three cases.

The RIA-ST-1 and RIA-ST-2 fuel rods each failed in the high power region. Figure 10 shows massive oxidation, oxide spalling, cladding splitting and fracture, and cladding ridging on each rod. Approximately 10% of the fuel from the RIA-ST-1 rod and 15% of the fuel from the RIA-ST-2 rod passed through the fuel particle catch screens and into the PBF loop. Cladding fracture and breakup is illustrated in more detail in Figure 11, which shows the remnants of the fuel stack of the RIA-ST-2 rod between the 0.37- and 0.47-m elevations. Only a small portion of the original fuel inventory in this region remained within the flow shroud. A longitudinal split in the fuel rod cladding was observed between the 0.47- and 0.61-m rod elevations in the 0- to 180-degree plane. A large percentage of the fuel was also missing from this region, as shown in Figure 12. The cladding in this region was extremely brittle and the fracture appeared to result from oxidation-induced embrittlement. Cladding ridging was observed at the pellet interfaces between the 0.675- and 0.780-m rod elevations. Small, circumferentially oriented cracks were detected at the ridge locations. Cladding collapse or waisting (collapse into pellet interfaces) was not observed in the RIA-ST-2 rod. Metallographic specimens from this rod near the peak flux location revealed wall thickness variations and some fuel and cladding reaction, with partial melting of the reaction zone. The posttest condition of the RIA-ST-1 rod (250 cal/g axial peak radial average fuel enthalpy or 275 cal/g peak fuel enthalpy) was similar to that of the RIA-ST-2 rod.

Neither visual inspection nor internal gas pressure measurement showed evidence of cladding failure or incipient failure in the RIA-ST-3 rod. The PBF fission product detection system confirmed that the rod did not fail. However, the rod did experience severe oxidation and cladding deformation, as was shown in Figure 10.

Since the fuel rod in RIA-ST-3 remained intact (free of through-wall cracks in the cladding) throughout the test, and the RIA-ST-1 fuel rod

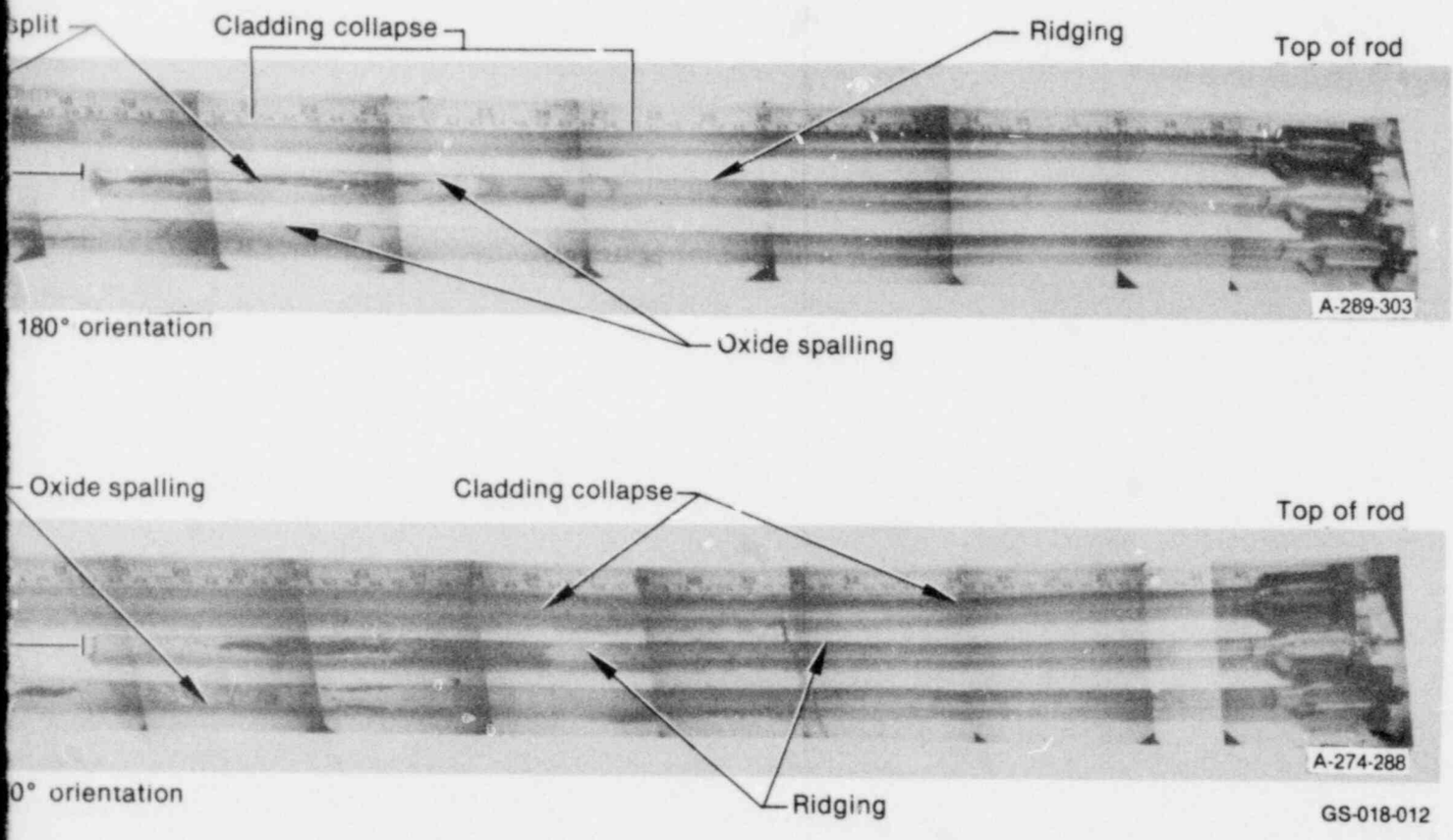

ppearances of the RIA-ST-1, RIA-ST-2, and RIA-ST-3 rods.

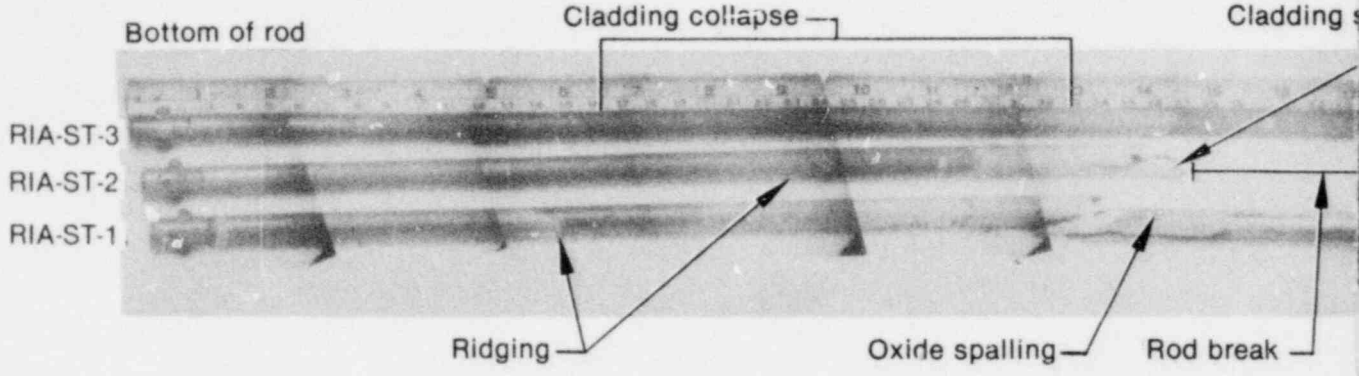

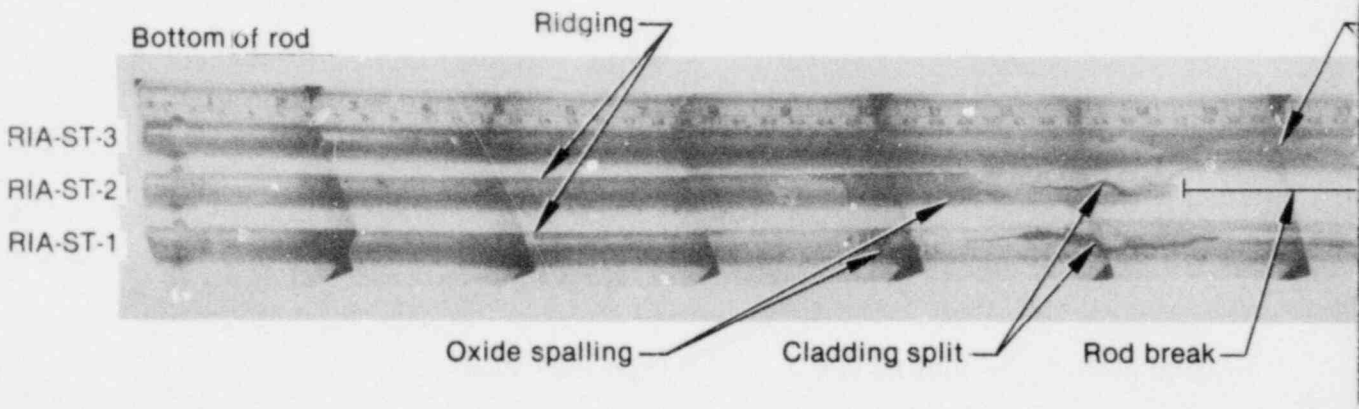

Figure 10. Posttest a

TABLE 10. SUMMARY OF TEST ROD DAMAGE FOR RIA-ST-1, RIA-ST-2, AND RIA-SI-3

Test	Peak Fuel Enthalpy (cal/g)	Axial Peak Radial Average Fuel Enthalpy (cal/g)	Total Radial Average Energy Deposition (cal/g UO_2)	Test Results	
				Condition	Posttest Description
RIA-ST-1, PB-1	205	185	250	Rod unfailed	--
RIA-ST-1, PB-2	275	250	330	Rod failed	Cladding wall thickness variations; severe oxidation, ridging, and waisting; brittle splitting of the cladding. Cladding fragmentation and loss; cladding embrittlement and local eutectic melting; fuel powdering, crumbling, and washout.
RIA-ST-2	290	260	345	Rod failed	Cladding wall thickness variations; severe oxidation, ridging, and waisting; brittle splitting of the cladding. Cladding fragmentation and loss; cladding embrittlement and local eutectic melting; fuel powdering,crumbling, and washout.
RIA-ST-3	250	225	300	Rod unfailed	Severe waisting over entire active length, and ridging at two pellet interfaces; oxide spalling; slight cladding wall thickness variations; fuel fracture.

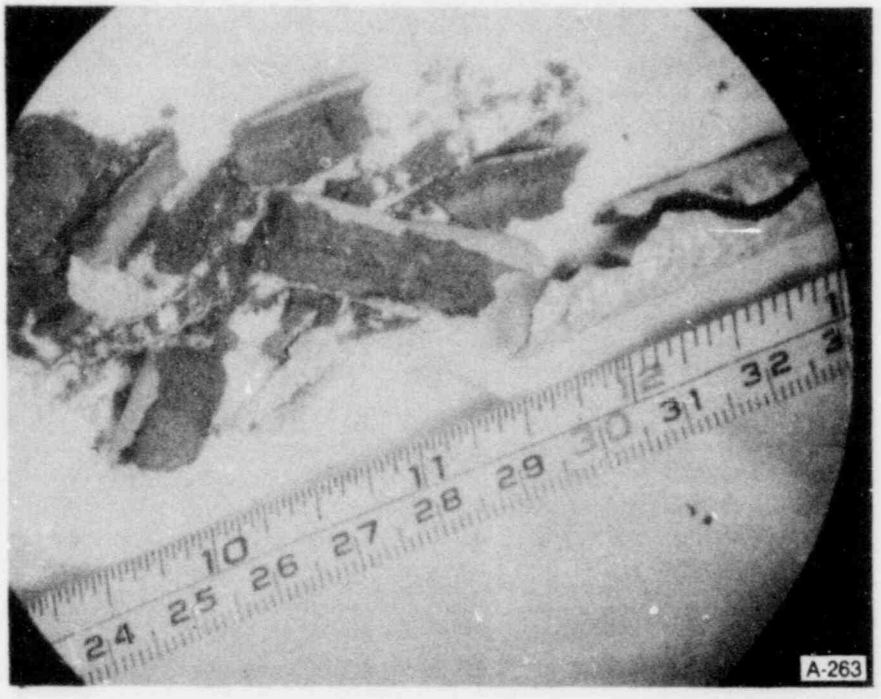

GS-018-042

Figure 11. Posttest photograph of RIA-ST-2 fuel rod between the 0.370- and 0.470-m rod elevations.

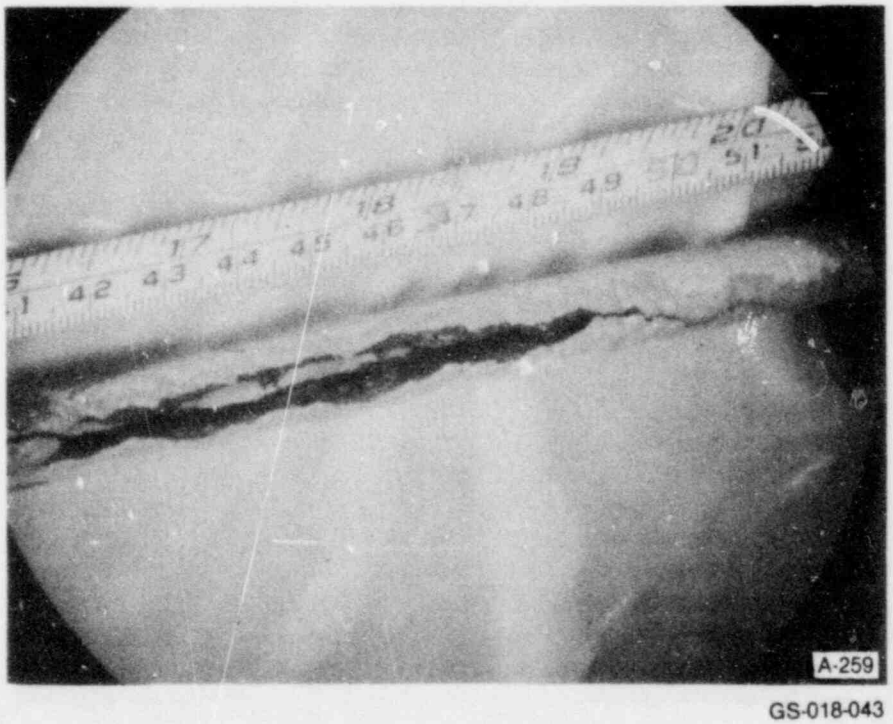

GS-018-043

Figure 12. Posttest photograph of RIA-ST-2 fuel rod between the 0.520- and 0.600-m rod elevations.

failed, the axial peak radial average fuel enthalpy failure threshold was concluded to be between 225 and 250 cal/g (250 and 275 cal/g peak fuel enthalpies); the values attained in those two experiments. The severity of failure of the RIA-ST-1 rod and the appearance of the RIA-ST-3 rod indicate that the axial peak radial average fuel enthalpy failure threshold is probably about 240 cal/g (265 cal/g peak); between the values of RIA-ST-1 and RIA-ST-3. In terms of the total radial average energy deposition at the peak power elevation, the failure threshold was about 315 cal/g UO_2.

5.2 RIA-ST-3 Fuel Rod Damage at 225 cal/g Axial Peak Radial Average Fuel Enthalpy (250 cal/g Peak Fuel Enthalpy)

This section details the RIA-ST-3 rod damage by describing the results of the posttest metallurgical examinations. The RIA-ST-3 rod reached an axial peak radial average fuel enthalpy of 225 cal/g, with a peak enthalpy near the pellet surface of 250 cal/g. The section begins with a summary of the calculated thermal boundary conditions for RIA-ST-3. The fuel rod thermal history during the transient was reconstructed using FRAP-T5.

5.2.1 Calculated Thermal Fuel Rod Boundary Conditions. The FRAP-T5 calculated transient temperature histories of the RIA-ST-3 rod are shown in Figure 13. According to FRAP-T5, the test rod fuel temperature increased nearly adiabatically following initiation of the power burst and reached a maximum of 3000 K near the end of the burst or at about 70 ms (as shown in Figure 13a). The fuel surface temperature followed the fuel centerline temperature to about 2100 K (50 ms), at which time hard pellet-to-cladding contact occurred, cooling the fuel surface. The fuel surface temperature paralleled the cladding surface temperature after 100 ms. This cooling of the fuel surface by the cladding accounts for most of the heat transfer from the fuel during the burst. The calculated maximum cladding surface temperature of 2098 K occurred shortly after the fuel temperature reached its maximum value (Figure 13b). Calculated fuel and cladding temperatures after about 1.5 s gradually decreased during the extended film boiling period. Cladding temperatures quenched when nucleate boiling was reestablished at about 21 s.

5.2.2 Cladding Deformation. The fuel-cladding gap, which closed shortly after initiation of the power transient, remained closed during the transient. At elevated temperatures, cladding is relatively soft and ductile, and cladding deformation results from stresses imposed on the cladding during the film boiling transient by the coolant hydrostatic pressure, by the thermal expansion of the fuel, and by thermal shock during quenching. The type of deformation produced on the RIA-ST-3 fuel rod consisted of rod bowing; cladding collapse, waisting, and ridging; and cladding thickening and thinning (wall thickness variations). These deformations are described subsequently.

Posttest measured fuel rod diameters indicated significant collapse of the cladding (Appendix C, "Posttest Fuel Rod and Shroud Deformation Measurements"). Only two of the pellet-to-pellet interfaces of this fuel rod, located 0.66 m from the bottom, exhibited ridging, as shown in Figure 14. Waisting (cladding collapse into pellet interfaces) was observed over the entire rod length, except in the middle part of the rod (from approximately 0.30 to 0.50 m). Rod bowing was also evident. Plastic deformation of the hot cladding produced wall thickness variations, as seen in the metallographic sample sectioned from near the axial midplane elevation, shown in Figure 15.

As discussed previously, FRAP-T5 calculations indicated that fuel temperatures increased rapidly during the power burst, but cladding temperatures required several seconds to reach maximum value. This behavior has been confirmed by data obtained in the extensive Japanese NSRR experiments.[9] The fuel-to-cladding gap closed immediately after initiation of the power burst, from a pretransient value of 0.092 mm. Therefore, the cladding expanded initially due to the thermal expansion of the fuel. The average diametral expansion during RIA-ST-3 was about 1%. Ridging was also expected at the pellet interfaces, because the pellets tend to assume an hourglass shape as they are heated during a rapid energy deposition. The ridging, observed at two pellet interfaces following RIA-ST-3, probably resulted from this fuel thermal expansion mechanism.

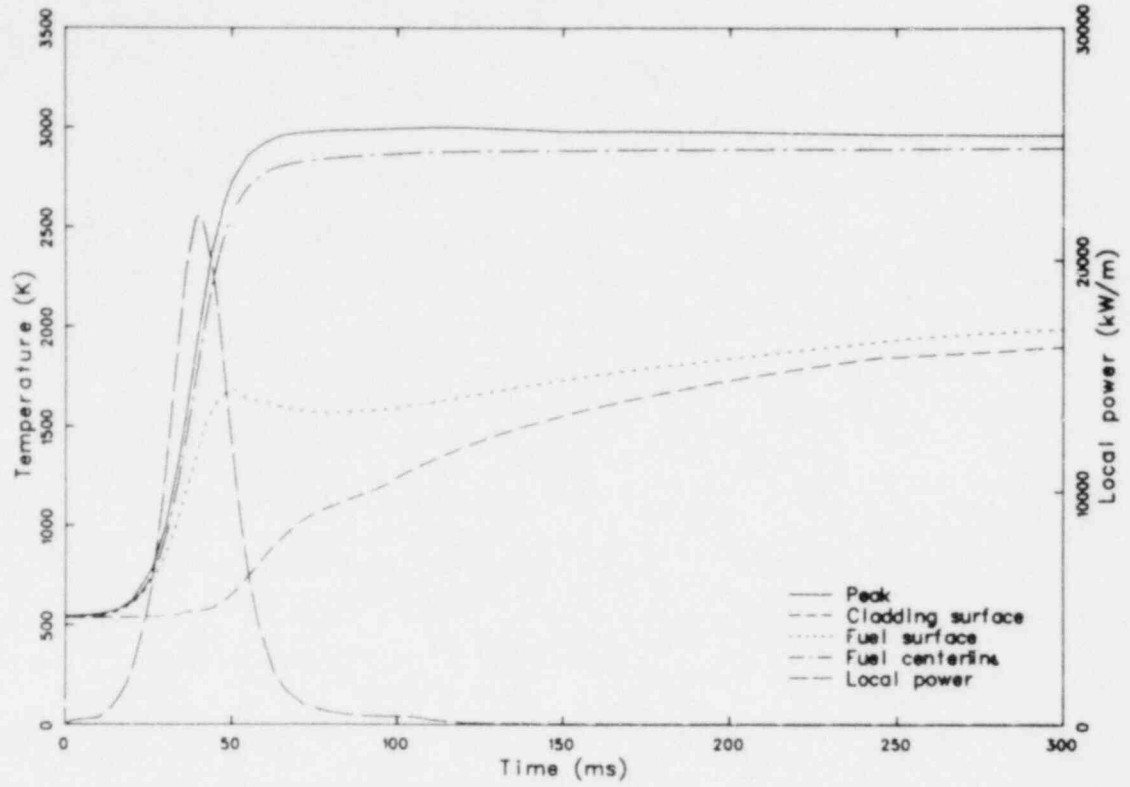

(a) 300-ms time scale showing temperature transients during the power burst

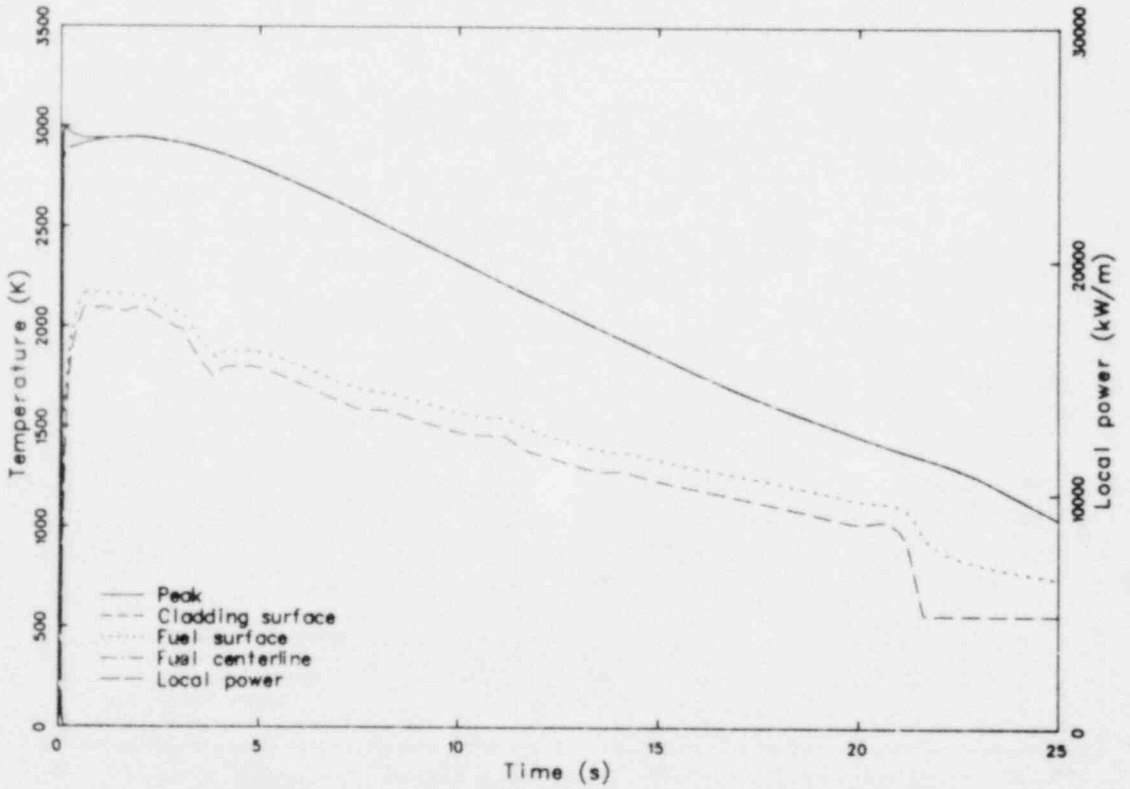

(b) 25-s time scale showing temperature transients over the full dryout range

Figure 13. Calculated fuel rod temperature histories at the axial peak power location for an axial peak radial average fuel enthalpy of 225 cal/g.

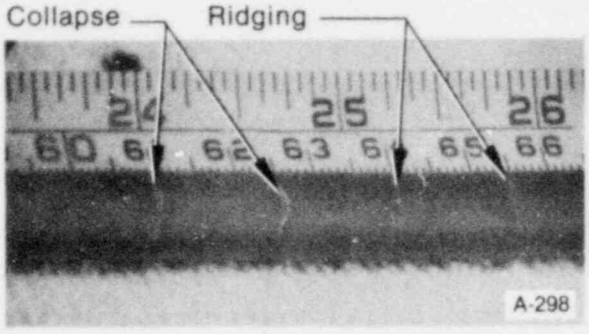

GS-018-044

Figure 14. Fuel rod ridging in the RIA-ST-3 rod.

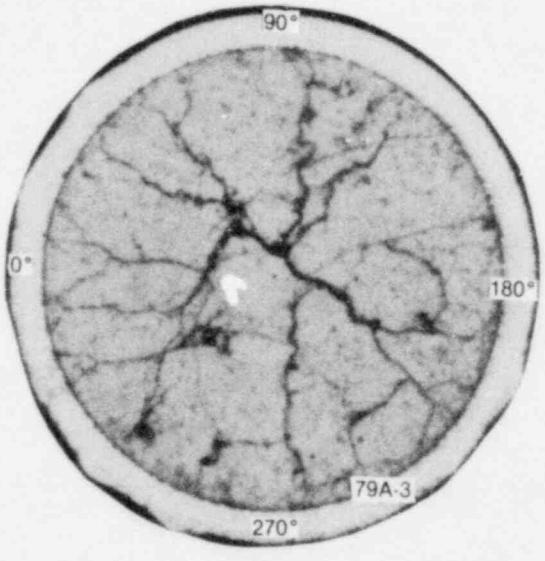

GS-018-047

Figure 15. Wall thickness variations in the RIA-ST-3 rod at 0.416 m from the bottom of the fuel stack.

5.2.3 Cladding-Water Reactions. At the elevated temperatures which occurred during film boiling operation, several forms of induced cladding chemical reaction occurred. The outer cladding surface oxidized as a result of the zircaloy-steam reaction, and the cladding reaction with the coolant produced a layer of oxygen-stabilized α-zircaloy and multiple layers of ZrO_2 on the cladding outer surface. The general features of the oxidized structure are illustrated in Figure 16, which is a magnified view of a metallographic sample from the RIA-ST-3 rod. The thicknesses of the layers of oxygen-stabilized α-zircaloy and ZrO_2 are summarized in Table 11. The multilayered (double) surface oxide had a grey-to-white appearance. The inner oxide layer typicaliy has been found to be hypostoichiometric (ZrO_{2-x}) in the NSRR experiments.[9] The outer oxide layer often fractures and separates from the inner oxide layer when mechanically stressed upon quenching. Significant hydriding was not observed in the specimen taken from the RIA-ST-3 rod. The oxide and oxygen-stabilized α-zircaloy layer thicknesses were fairly uniform on the circumference of the cladding, suggesting that azimuthal temperature variations were small. Local fracturing in the brittle outer layer of oxygen-stabilized α-zircaloy, presumably caused by thermal stresses upon quenching, is also shown in Figure 16. (All elevations noted are measured from the bottom of the fuel stack, unless specified otherwise.) Despite the local fracturing, fuel rod failure (generation of through-wall cracks) did not occur because of the presence of a relatively thick and ductile prior β-zircaloy cladding layer.

5.2.4 Cladding-Fuel Reactions. Cladding-fuel contact, either by fuel expansion or cladding collapse, occurred during the RIA-ST power transients. During this contact, a fuel-cladding reaction can occur if cladding temperatures exceed the α to $\alpha + \beta$ phase transformation temperature ($\sim$1085 K). In RIA-ST-3, the reaction resulted in the formation of an oxygen-stabilized α-zircaloy layer at the inner surface of the cladding and (U,Zr) alloy duplex layers at the pellet-cladding interfaces. As shown in Figure 17, the duplex zone consisted of two different layers which were similar to the UO_2-zircaloy reaction layers observed in other PBF experiments. On the basis of the metallographic appearance of the duplex layers, it is concluded that these layers consisted of a U-rich (U,Zr) alloy layer and a Zr-rich (U,Zr) alloy layer. These reaction layers were identical to those observed in the Japanese NSRR RIA experiments. The Zr-rich (U,Zr) alloy layer was essentially an oxygen-stabilized α-zircaloy layer with U or (U,Zr) alloy precipitates, mainly along the oxygen-stabilized α-layer grain boundaries. This type of reaction layer is illustrated in the photographs of an NSRR metallographic sample shown in Figure 18.

The U-rich (U, Zr) alloy layer probably resulted from the diffusion of uranium into the zircaloy cladding after the UO_2 was partially reduced by zircaloy at elevated temperatures. As was shown in Figures 17 and 18, the migration of the uranium component was not uniform, which is as expected in specimens subjected to very high temperatures for a short time.

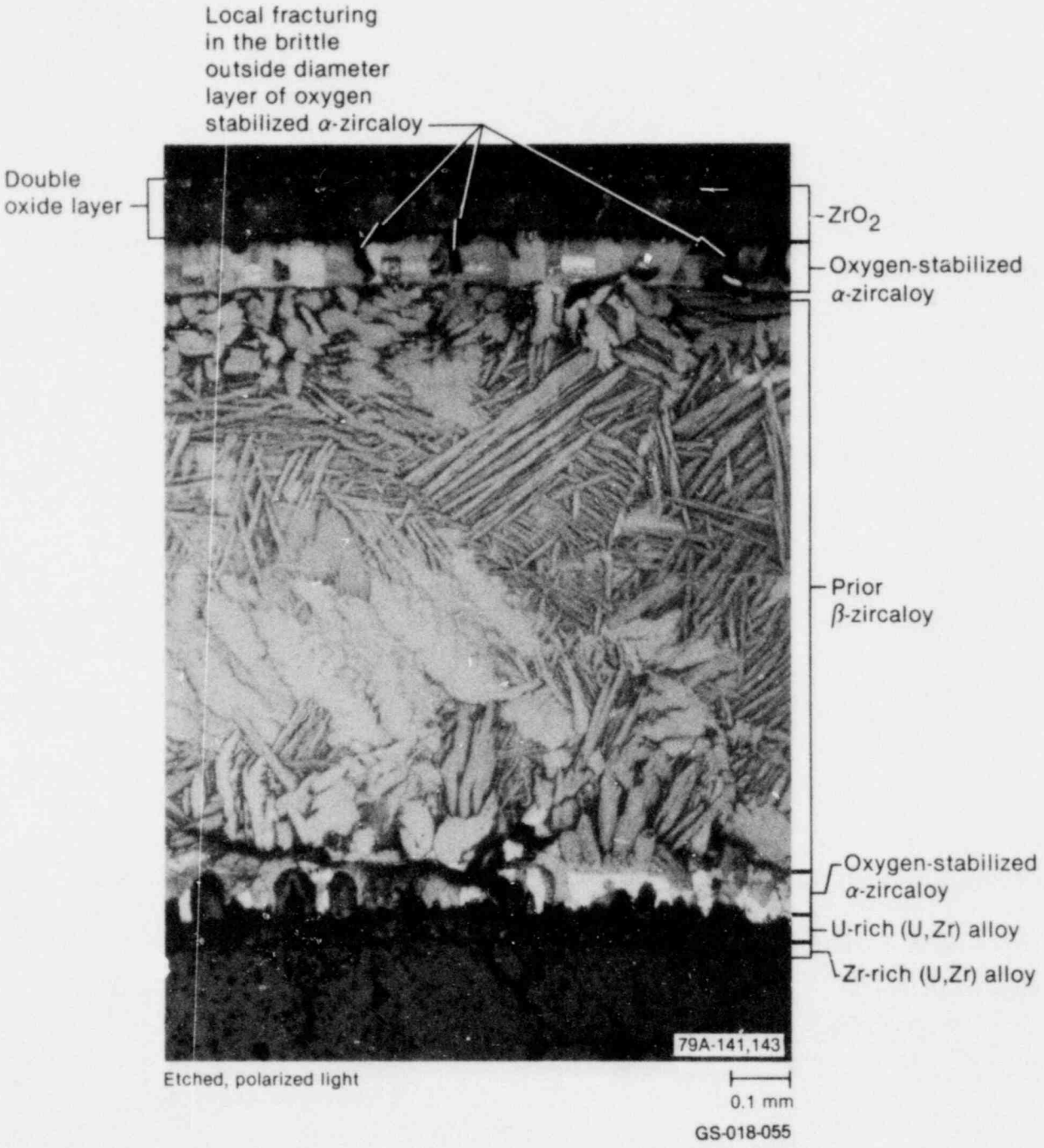

Figure 16. General features of oxidized cladding in the RIA-ST-3 rod (225 cal/g axial peak radial average fuel enthalpy) at the 0.416-m elevation and the 90-degree orientation.

TABLE 11. SUMMARY OF CHEMICAL INTERACTION LAYER THICKNESSES IN RIA-ST-3[a]

Orientation (degrees)	ZrO_2 (μm)	Outer Oxygen-Stabilized α-Zircaloy (μm)	Prior β-Zircaloy (μm)	Inner Oxygen-Stabilized[b] α-Zircaloy (μm)	Zr-Rich (U,Zr) Alloy (μm)	Cladding Wall[b] Thickness[c] (mm)
0	50	50	480	50	25	0.625
90	55	50	505	50	20	0.660
180	55	50	475	65	20 to 25	0.645
270	40[d]	50	505	55	20	0.650
300[e]	35[d]	50	480 to 605	60	20 to 25	0.625 to 0.750
Average	50	50	495	55	20	0.650

a. This specimen was located 0.416 m from the bottom of fuel stack.

b. Including U-rich (U,Zr) alloy layer.

c. Excluding Zr-rich (U,Zr) alloy layer.

d. These values may be slightly underestimated due to edge rounding during polishing.

e. Local thickening occurred at this angular orientation.

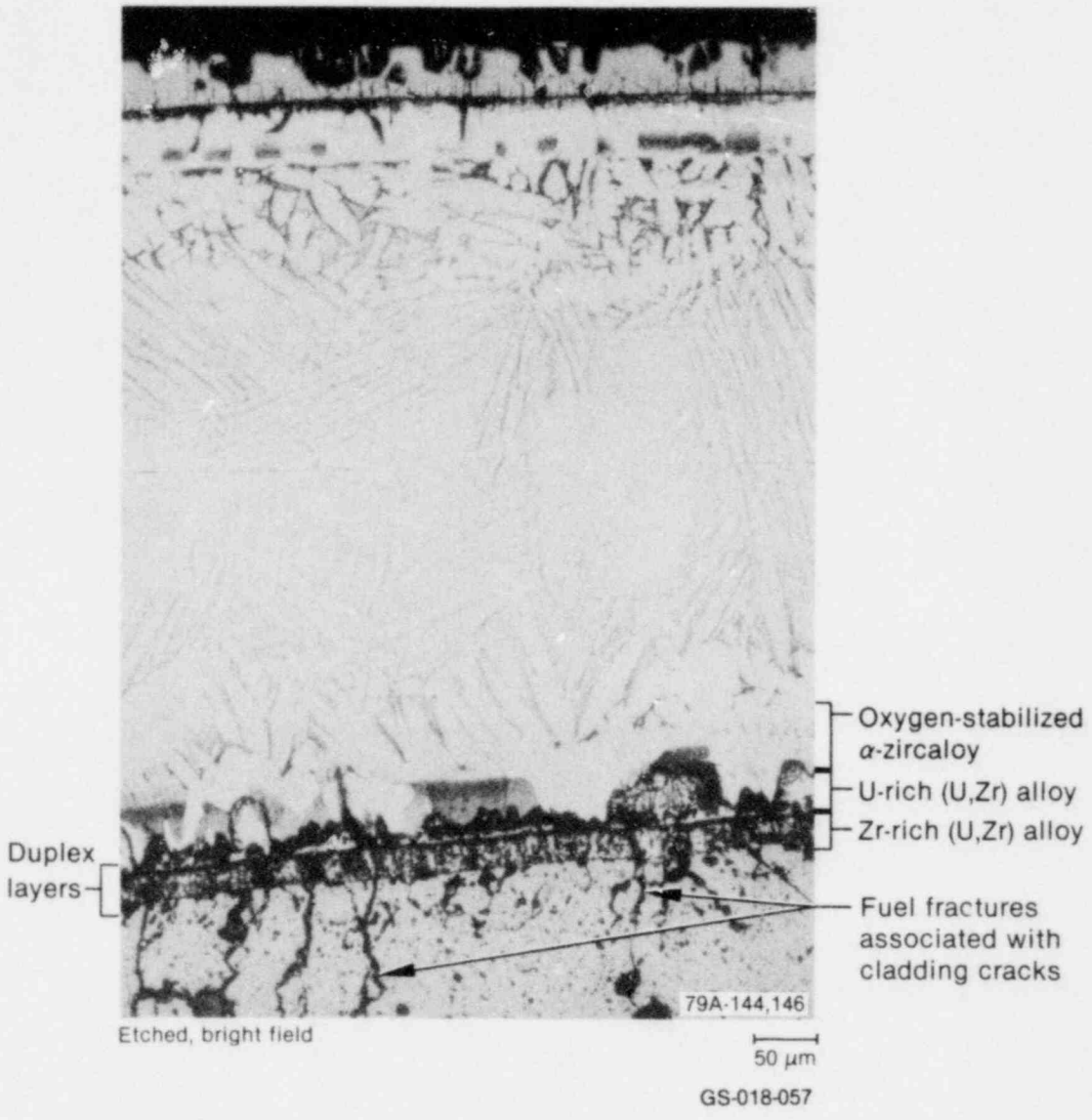

Figure 17. Cladding-fuel chemical reaction in the RIA-ST-3 rod (225 cal/g axial peak radial average fuel enthalpy) at the 0.416-m elevation and the 0-degree orientation.

As was shown in Table 11, the thickness of the inner oxygen-stabilized α-zircaloy layer (due to the UO_2-zircaloy reaction) was about the same as that formed at the outer surface (due to the zircaloy-steam reaction). This equivalence of inner and outer α-zircaloy layer thicknesses indicates that the inner cladding temperature was only slightly higher than the outer temperature during the power burst, since the extent of both oxygen-stabilized α-layers is primarily controlled by diffusion of oxygen into the β-phase zircaloy, as suggested by P. Hofmann et al.[10]

Figure 19 shows a zircaloy projection into the RIA-ST-3 fuel and zircaloy migration within the UO_2, suggesting cladding-fuel eutectic melting. The U-Zr alloys have a lower melting point than zircaloy. An unidentified phase, different from the Zr-rich (U,Zr) alloy phase, was found around the zones of isolated zircaloy migration.

The location of the original pellet-cladding interface was uncertain. P. Hofmann et al.,[10] have suggested that the orginal interface lies between the U-rich (U,Zr) alloy layer and the oxygen-stabilized α-zircaloy layer. However, the initial fuel-cladding interface was probably not there because of the nonuniform growth of the U-rich (U,Zr) alloy layer. Since the U-rich (U,Zr) reaction layer and the Zr-rich (U,Zr) reaction

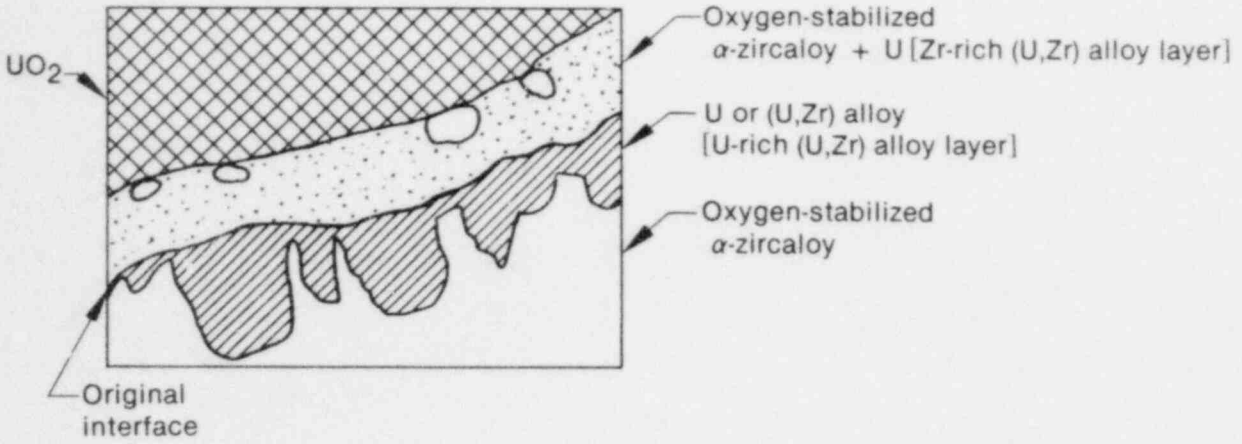

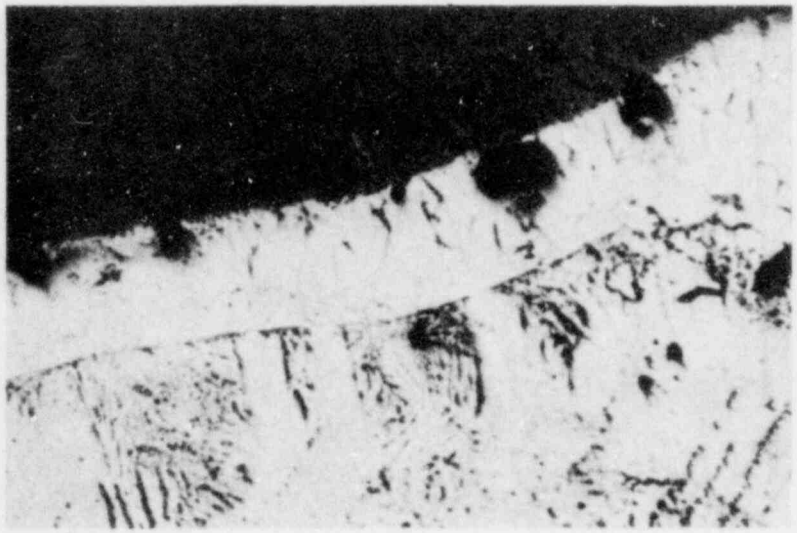

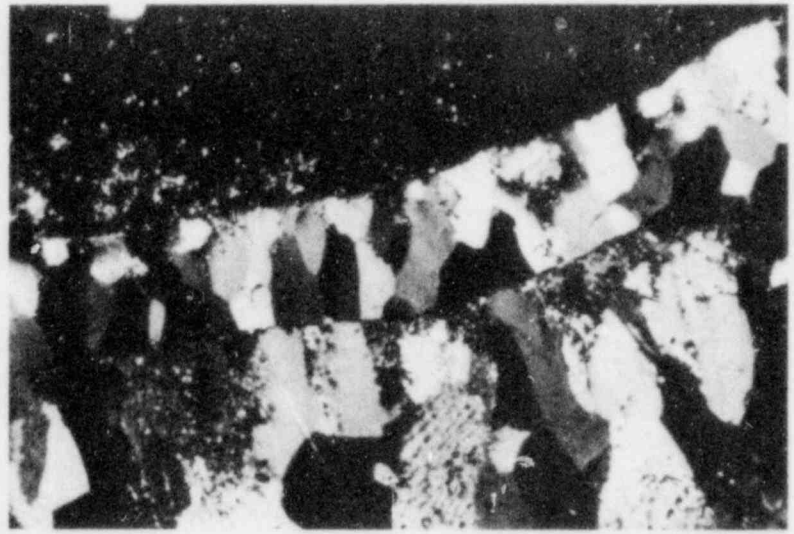

GS-018-069

Figure 18. Transverse section of an NSRR fuel rod, showing UO_2-zircaloy reaction layers (courtesy of the Japan Atomic Energy Research Institute).

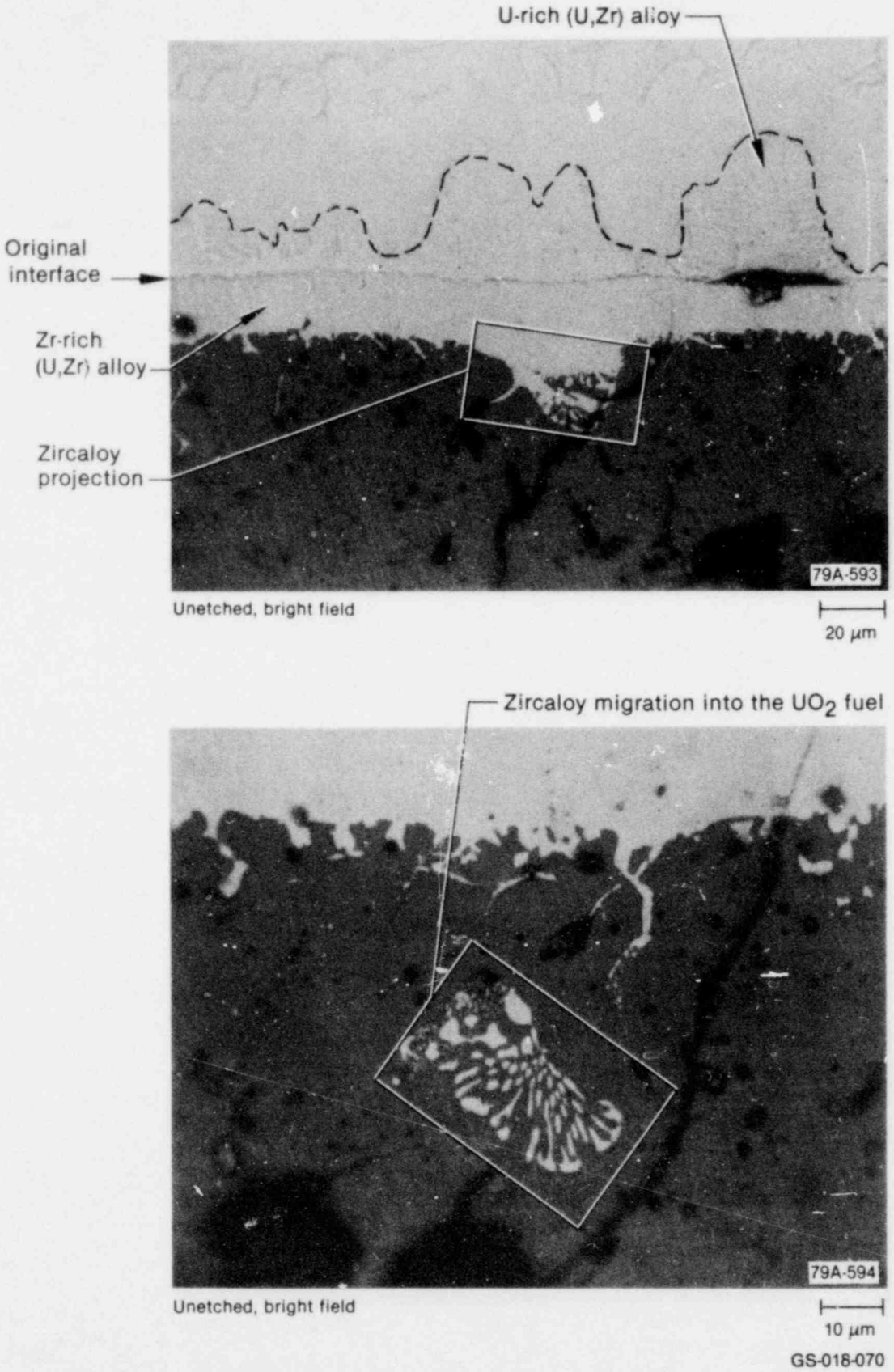

Figure 19. Zircaloy projection and migration into the fuel in the RIA-ST-3 rod (225 cal/g axial peak radial average fuel enthalpy) at the 0.416-m elevation and the 90-degree orientation, suggesting cladding-fuel eutectic melting.

layer probably resulted from the migration of uranium from the UO_2 fuel and zirconium from the cladding, respectively, the initial pellet-cladding interface was probably between the Zr-rich (U,Zr) alloy and the U-rich (U, Zr) alloy. Therefore, the thickness of the inner oxygen-stabilized α-zircaloy layer presented in Table 11 (which indicates the extent of oxygen diffusion from the UO_2 pellet into the cladding) includes the U-rich (U,Zr) alloy layer. For the same reason, the Zr-rich (U,Zr) alloy layer is excluded in the cladding wall thickness measurements in Table 11.

The UO_2-zircaloy interaction usually causes strong bonding between the UO_2 fuel and the zircaloy cladding. As is seen in Figures 17, 18, and 19, the UO_2 fuel remained in contact with the cladding. The FRAP-T5 calculation, in which the UO_2-zircaloy reaction is not modeled, predicted that the fuel-cladding gap would reopen upon fuel rod quenching or rewetting. The strong bonding that was observed in the RIA-ST-3 rod should be modeled in FRAP-T since it affects the fuel and cladding behavior during an RIA.

5.2.5 Scenario of Cladding Damage. The process of cladding damage for a power burst resulting in an axial peak radial average fuel enthalpy of 225 cal/g (250 cal/g peak) can be summarized as follows. Due to the rapid thermal expansion of the fuel, the cladding deformed early in the transient while it was still relatively cool. This deformation resulted in an overall rod diameter increase, ridging at the pellet interfaces, and probably bowing due to nonuniform circumferential deformation. As the cladding temperature increased and the cladding lost mechanical strength, significant collapse occurred over nearly the entire fuel region, especially at the pellet interfaces (waisting). The zircaloy then oxidized on both the inner and outer surfaces. The embrittlement due to oxidation was not complete; therefore, fuel rod failure did not occur as a result of the thermal stresses upon quenching.

5.2.6 Fuel Restructuring. Thermal restructuring of the UO_2 fuel occurred during the RIA-ST-3 transient. The restructuring was characterized by limited grain growth over the entire fuel pellet at the 0.416-m axial elevation (near the peak flux), with UO_2 grain sizes of approximately 28, 20, and 18 μm near the center, midradius, and edge, respectively. (Initial fuel grain size was less than 10 μm).

There was no evidence of fuel melting or columnar grain growth. The enthalpy required for initiation of UO_2 melting is 270 cal/g; approximately 20 cal/g greater than the peak fuel enthalpy near the pellet surface determined for RIA-ST-3 (250 cal/g).

Fuel fracturing accompanied rapid heating and cooling. Figure 20 indicates that most of the large fuel cracks were radial in orientation; relatively wide near the center of the pellet, and narrower toward the outer pellet periphery. Transgranular fracturing was common and did not necessarily follow lines of porosity. Fuel shattering and powdery fuel, defined as grain boundary separation in fine-grained fuel, did not occur. Results from the Japanese NSRR program indicate that radial and axial cracks are induced in a fuel pellet during a power burst which deposits an energy of only 50 cal/g UO_2. Therefore, although many of the small cracks around the pellet periphery may have been formed upon quenching of the rod, most of the large fuel cracks observed in RIA-ST-3 were probably induced by thermal stresses during heatup.

5.3 RIA-ST-1 and RIA-ST-2 Fuel Rod Damage at 250 to 260 cal/g Axial Peak Radial Average Fuel Enthalpy (275 to 290 cal/g Peak Fuel Enthalpy)

This section details the rod damage observed in RIA-ST-1 and RIA-ST-2 by describing the results of the posttest metallurgical examinations. The RIA-ST-1 and RIA-ST-2 rods reached axial peak radial average fuel enthalpies of 250 and 260 cal/g, respectively, or peak fuel enthalpies near the fuel pellet surface of 275 and 290 cal/g. The section begins with a summary of the calculated thermal boundary conditions for the two experiments.

5.3.1 Calculated Thermal Fuel Rod Boundary Conditions. As shown in Figure 21, the FRAP-T5 calculated time-dependent temperature responses for RIA-ST-2 are higher than those for RIA-ST-3 (shown previously in Figure 13), and partial melting of the fuel and complete melting of the cladding was predicted to occur. The FRAP-T5 calculated temperatures for RIA-ST-1

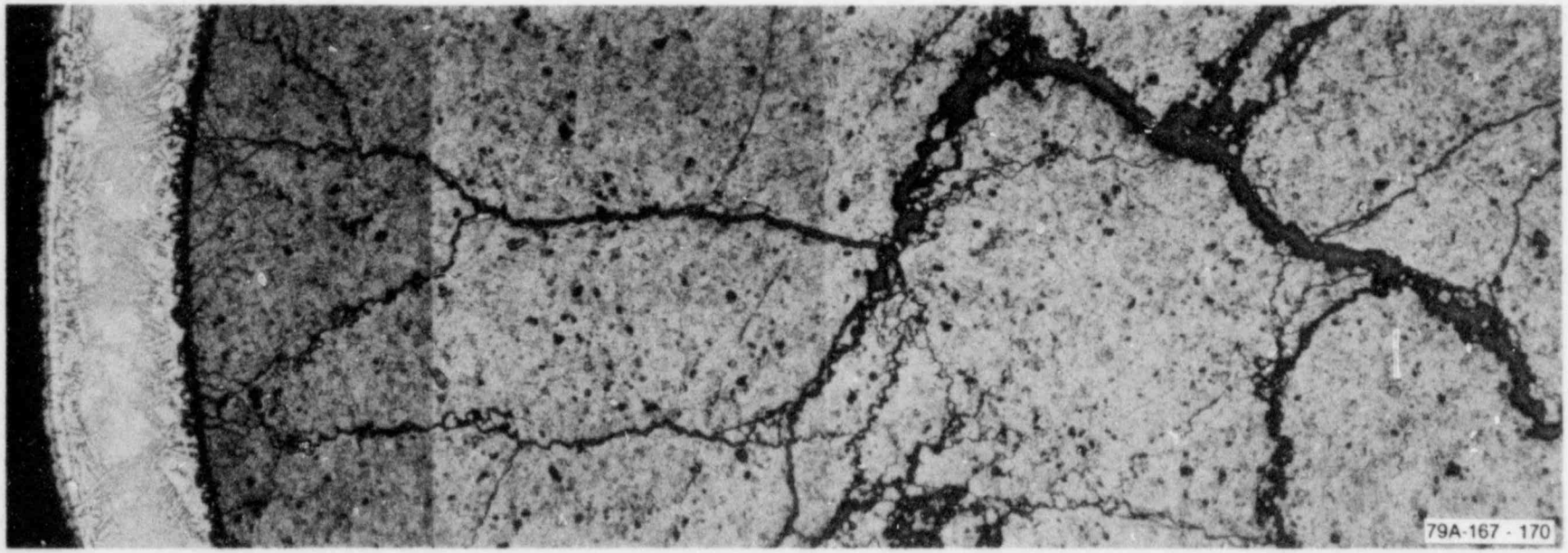

Etched, bright field

200 μm

GS-018-068

Figure 20. Fuel cracks in the RIA-ST-3 rod (225 cal/g axial peak radial average fuel enthalpy) at the 0.416-m elevation and the 0-degree orientation.

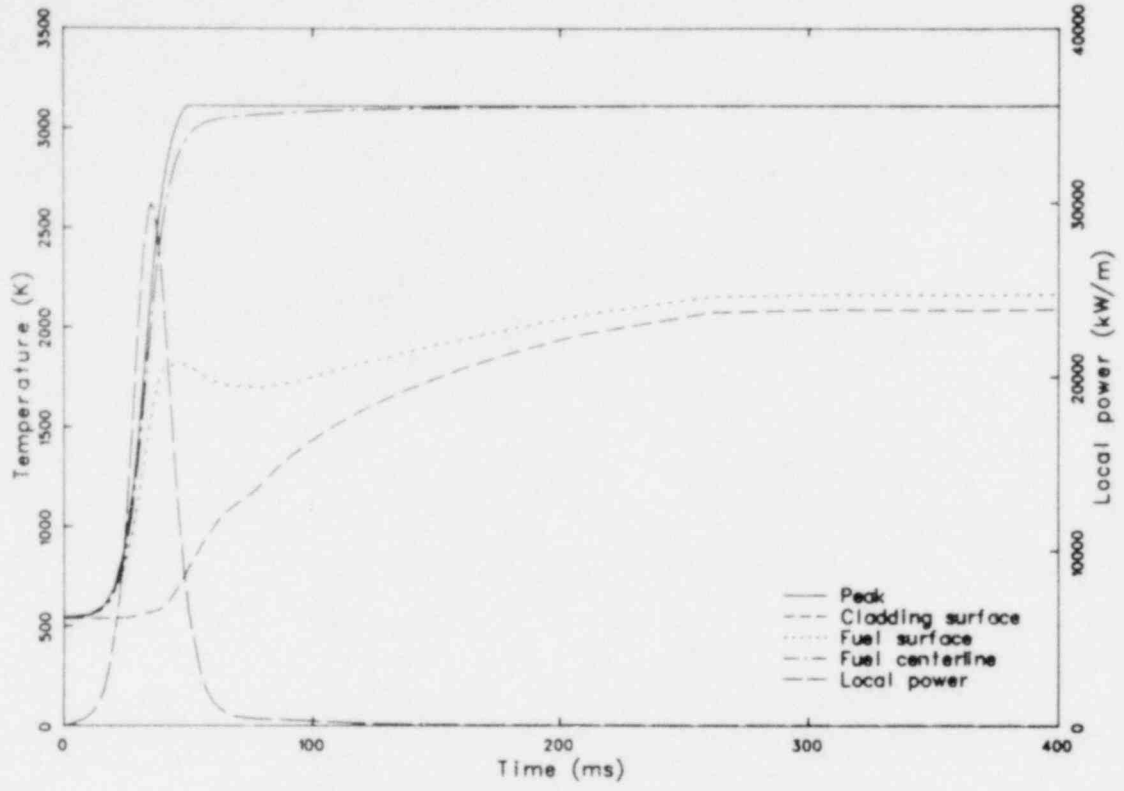

(a) 400-ms time scale showing temperature transients during the power burst

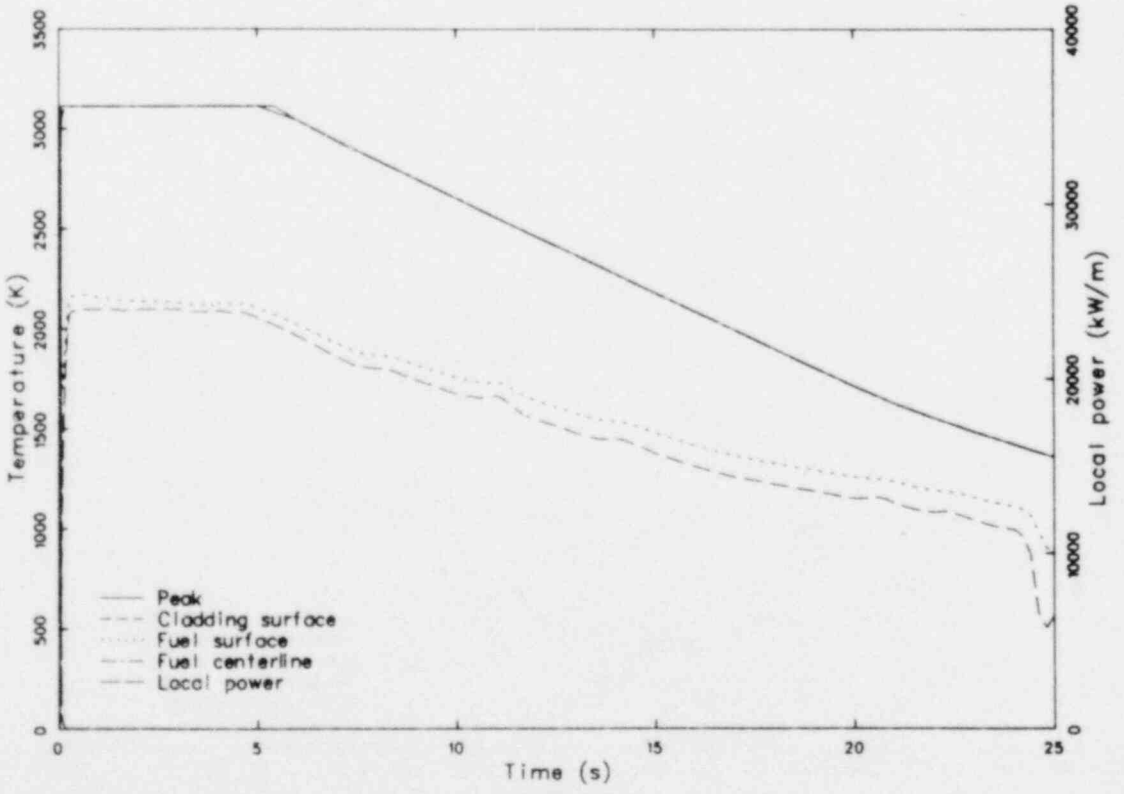

(b) 25-s time scale showing temperature transients over the full dryout range

Figure 21. Calculated fuel rod temperature histories at the axial peak power location for an axial peak radial average fuel enthalpy of 260 cal/g.

are nearly identical to those shown in Figure 21, except that only partial melting of the cladding is calculated. Posttest microstructures showed no evidence of fuel pellet melting, although partial melting of the fuel-cladding interaction zone was observed. The enthalpy required for initiation of fuel melting is ~270 cal/g. The BUILD5 computer code calculation[a] suggests a cladding peak temperature sufficient to ensure the complete melting of the cladding. Gap closure behavior similar to that for the RIA-ST-3 transient was calculated by FRAP-T5, but more severe fuel-cladding mechanical interaction (earlier closure and greater contact stress) was predicted.

5.3.2 Cladding Wall Thickness Variations. Metallographic examination of the fuel rod cross sections from RIA-ST-1 and RIA-ST-2 showed radial cladding ovality changes and twisting, as well as extensive wall thickness variations. All cracks observed in the cladding were in the thinner regions. An example of these circumferential wall thickness variations is illustrated in Figure 22 with a sample from the failed RIA-ST-1 fuel rod. Figure 23 shows the variations in cladding wall thickness, oxide thickness, and prior β-phase thickness for all of the RIA-ST-1, RIA-ST-2, and RIA-ST-3 specimens. The oxidation layer thicknesses[b] were nearly uniform around the circumference of the cladding and did not follow the wall thickness variations; whereas the variations in prior β-zircaloy layer thickness corresponded perfectly to the variations in wall thickness. As shown in Figure 23, no prior β-phase existed in the regions of cladding wall thinning; that is, complete through-wall oxidation from both the inner and outer cladding surfaces was observed. This complete through-wall oxidation suggests that cladding wall thickness variations occurred prior to significant oxidation. Similar wall thickness variations have been observed in the NSRR experiments at energy depositions of ~200 cal/g UO_2, in which the maximum cladding surface temperature was greater than 1500 K.

Gross wall thickening and thinning probably occurred as a result of extensive plastic flow of the hot cladding. This plastic flow was probably assisted by either variations in the local coolant pressure associated with the rapid heating of the coolant during the transient, by surface tension, by residual stresses in the cladding, or by fuel thermal expansion. The effect of wall thinning is important to fuel rod failure, as evidenced by the observation that all of the cladding cracks or fractures occurred in the thinner cladding regions, presumably because the extent of oxidation and, therefore, of embrittlement, was greater in the thinner cladding regions. Cladding embrittlement and fracturing are discussed in a subsequent subsection.

5.3.3 Cladding-Water Reactions. In both RIA-ST-1 and RIA-ST-2, the fuel rod cladding reacted with coolant water vapor to produce layers of ZrO_2 and oxygen-stabilized α-zircaloy on the outer surface of the cladding. A similar reaction would be expected to occur on the cladding inner surface if the fuel rod had failed during the power burst when the cladding was hot. No inner cladding surface oxide or UO_2 fuel oxidation was observed in this study.

The RIA-ST-2 rod exhibited oxide thicknesses at the failure location of 95 to 125 μm, with oxygen-stabilized α-zircaloy layer thicknesses ranging from 80 to 180 μm, depending on the circumferential orientation. In general, the oxygen-stabilized α-layer was thicker in the regions of wall thinning, since the oxygen concentration was higher in these regions. The thickness of the oxygen-stabilized α-zircaloy layer averaged 85 μm in the thicker cladding regions and 135 μm in the thinner regions. Table 12 summarizes the layer thickness measurements taken from the specimens of the RIA-ST-2 fuel rod. The amount of oxidation observed on the RIA-ST-1 rod was greater than that on the RIA-ST-2 rod, presumably because the RIA-ST-1 rod was subjected to two power bursts; the first resulting in a peak fuel enthalpy near the pellet surface of 205 cal/g and the second in 275 cal/g. Duplex oxide layers and local fracturing of the oxide and oxygen-stabilized α-layers were present in both the RIA-ST-1 and RIA-ST-2 rod specimens.

5.3.4 Cladding-Fuel Reactions. UO_2 fuel-zircaloy cladding reactions similar to those in the RIA-ST-3 fuel rod were observed in the failed RIA-ST-1 and RIA-ST-2 fuel rods. The individual

---

a. The BUILD5 computer code was developed by R. Pawel at the Oak Ridge National Laboratory to predict oxygen uptake at high temperatures. Details are described in Appendix C, "Cladding Surface Temperature Estimates." The cladding temperatures reached were greater than the upper limit (1750 K) for the correlation used in BUILD5; however, good results have been obtained by extrapolating cladding temperatures beyond that upper limit.

b. Zirconium oxide and oxygen-stabilized α-zircaloy by steam reaction, and oxygen-stabilized α-zircaloy by fuel reaction.

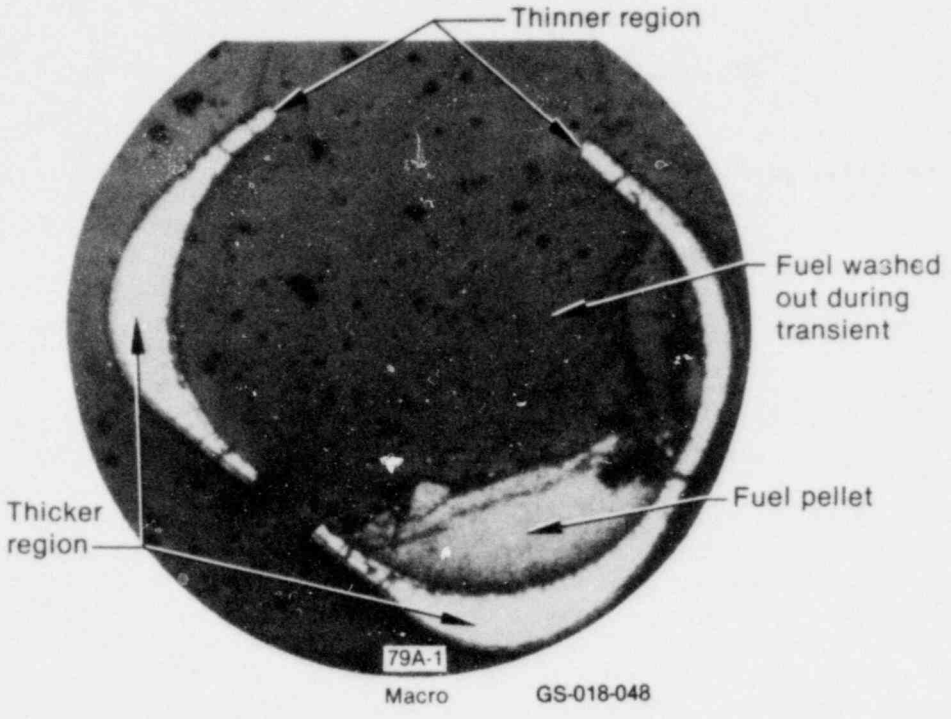

Figure 22. Wall thickness variations in the RIA-ST-1 rod (250 cal/g axial peak radial average fuel enthalpy) at the 0.354-m elevation.

phases can be represented as follows: $[UO_2]$→ [Zr-rich (U,Zr) alloy; that is, oxygen-stabilized α-zircaloy including U and/or (U,Zr) alloy precipitates]→[U-rich (U,Zr) alloy] → [oxygen-stabilized α-zircaloy]→[zircaloy]. The number of phases and their sequence was generally the same over the range of the energy depositions investigated; only the extent of the reaction layers differed greatly. The thicknesses of each layer are shown in Table 12 for RIA-ST-2. Again, the inner oxygen-stabilized α-zircaloy layer was somewhat thicker than the outer layer. A typical UO_2-zircaloy interaction layer photomicrograph is presented in Figure 24.

In the higher energy deposition RIA-ST-1 and RIA-ST-2 fuel rod samples, the ratio of the U-Zr alloy layer thickness to the inner oxygen-stabilized α-zircaloy [α-Zr(O)] layer thickness was greater than the same ratio for the low energy deposition fuel rod samples, as indicated by comparison of the values in Tables 11 and 12. That is, for similar values of oxygen-stabilized α-zircaloy layer thickness, the lower energy (lower temperature) samples had a thinner U-Zr alloy layer than the higher energy (higher temperature) samples. Since the thickness of a layer (ξ) is expressed as,

$$\xi = K_o \exp\left[\frac{-Q}{RT}\right],$$

where K_o is the diffusion constant, Q is the activation energy, R is a gas constant, and T is the temperature in K.

Then,

$$\frac{\xi_{(U,Zr)}}{\xi_{\alpha(O)}} = \frac{K_{o,\,(U,Zr)} \exp\left[\frac{-Q_{(U,Zr)}}{RT}\right]}{K_{o,\alpha(O)} \exp\left[\frac{-Q_{\alpha(O)}}{RT}\right]}$$

$$= \frac{K_{o,\,(U,Zr)}}{K_{o,\alpha(O)}} \left(\exp -\left\{\frac{1}{RT}\left[Q_{(U,Zr)} - Q_{\alpha(O)}\right]\right\}\right)$$

where

ξ = reaction layer thickness

K_o = diffusion constant

Q = activation energy.

Thus, the observation that the (U,Zr) alloy to α(O) ratio increases with temperature, indicates

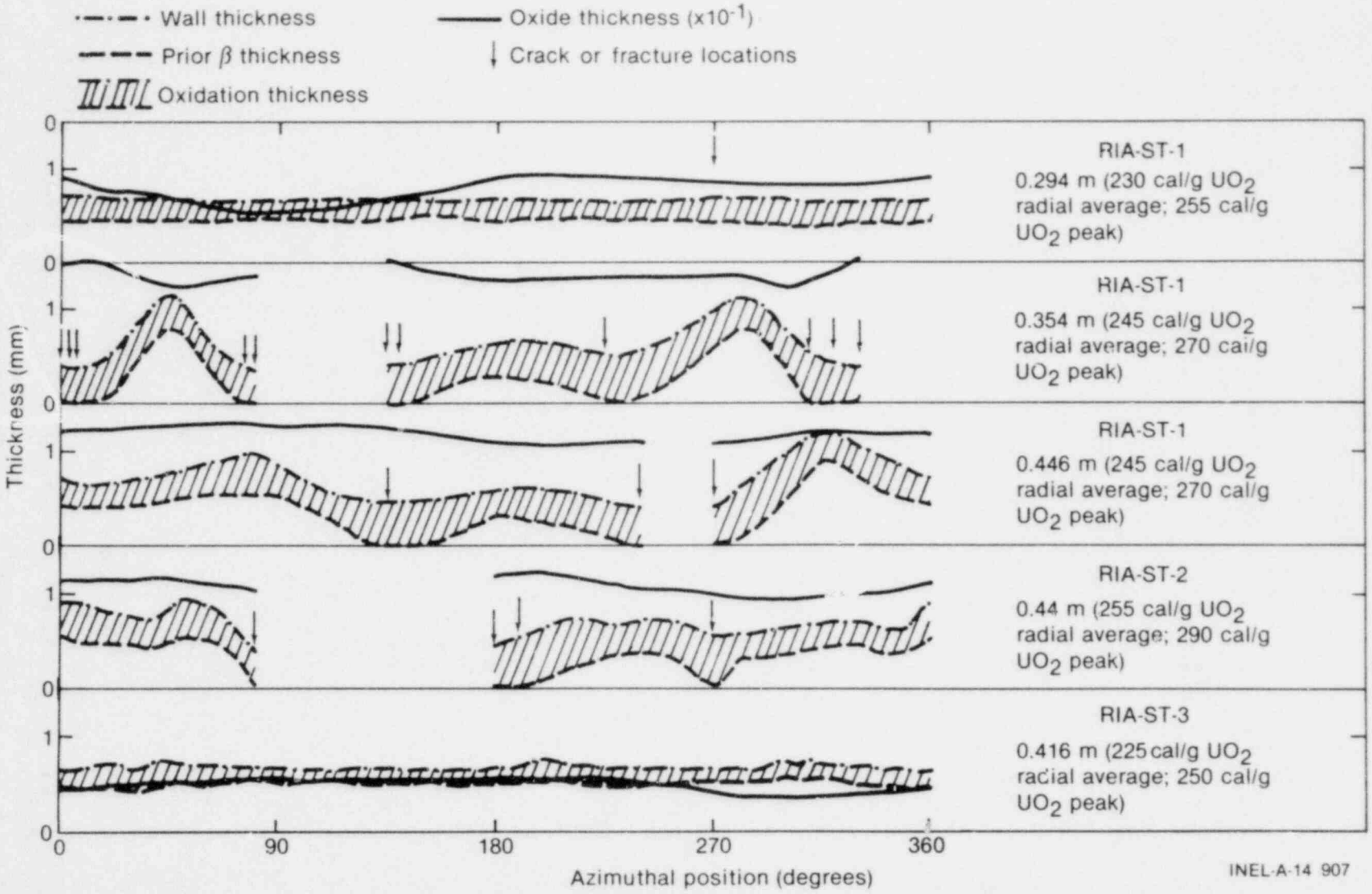

Figure 23. Thickness variations of cladding wall, prior-β layer, and oxide layer for the RIA-ST-1, RIA-ST-2, and RIA-ST-3 fuel rods.

TABLE 12. SUMMARY OF CHEMICAL INTERACTION LAYER THICKNESSES IN RIA-ST-2[a]

Orientation (degrees)	ZrO_2 (μm)	Outer Oxygen-Stabilized α-Zircaloy (μm)	Prior β-Zircaloy (μm)	Inner Oxygen-Stabilized α-Zircaloy[b] (μm)	Zr-Rich (U,Zr) Alloy (μm)	Cladding Wall Thickness[c] (mm)
30	115	85	465	90	110	0.755
68	125	95	420	105	110	0.745
72	110	90	350	105	85	0.655
80	105	120	0	185	110	0.410
180	125	120	40	155	d	0.440
190	125	125	0	275	d	0.525
230	110	90	330	115	105	0.665
270	100	180	0	255	d	0.535
280	95	80	325	75	75	0.575
330	100	80	445	85	130	0.710

a. This specimen was located 0.44 m from the bottom of the fuel stack.

b. Including U-rich (U,Zr) alloy layer.

c. Excluding Zr-rich (U,Zr) alloy layer.

d. Not measured.

that the activation energy (Q) for U diffusion is greater than the activation energy for oxygen diffusion. This result is in agreement with Hofmann's out-of-pile experiments.[10]

A posttest gap between the UO_2 fuel and the cladding was observed at some circumferential locations in the higher energy deposition samples, as shown in Figure 24. However, the UO_2-zircaloy reaction was evident around the entire circumference, and the reaction layers were almost constant in thickness, independent of the presence of a posttest fuel-to-cladding gap. Because the UO_2-zircaloy reaction will not occur without solid-to-solid contact, the UO_2 fuel and zircaloy cladding must have been in contact around the entire circumference when elevated temperatures were present. The fuel separation probably occurred due to thermal contraction of the fuel pellets during cooling. In general, the reformation of the gap occurred at the interface between the UO_2 pellet and the duplex layer, rather than at the original cladding interface. The fact that fuel separation was rare in the lower energy deposition RIA-ST-3 fuel rod supports the hypothesis of the fuel separation mechanism mentioned previously, since larger thermal contraction would be expected in the higher energy deposition RIA-ST-1 and RIA-ST-2 fuel rods.

Brittle fractures of the reaction layers were observed even in unfailed regions of the test rods (regions without through-wall cracks). Reaction layer fractures are often associated with fractures in the fuel pellet periphery. The association is obscured in Figure 24 because of fuel shattering, but was illustrated from the RIA-ST-3 fuel rod in Figure 17. The presence of reaction layer fractures in unfailed regions of the rods suggests that the cracks were induced after the fuel rods cooled

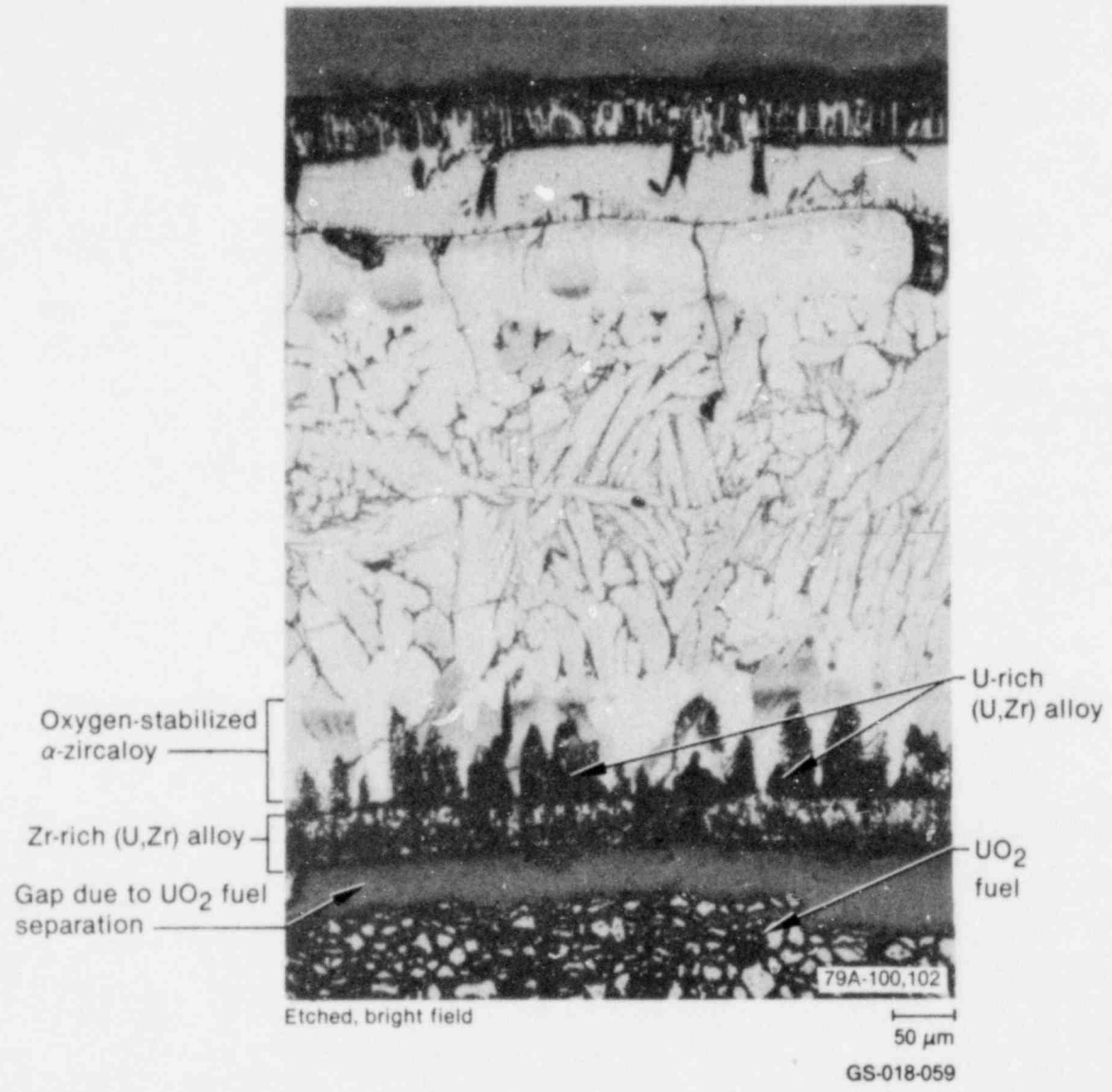

Figure 24. Typical UO_2-zircaloy interaction layers in the RIA-ST-1 rod (250 cal/g axial peak radial average fuel enthalpy) at the 0.446-m elevation and the 180-degree orientation.

down, possibly upon quenching, because fuel fractures which run toward the pellet center generally do not occur during the heatup process or during stable film boiling. Similar fuel fractures might be expected in the higher energy deposition fuel rods, but the fuel separation and gap reformation induced after quenching (after fuel rod failure) and fuel shattering obscure this type of fuel fracture.

Some abnormal and unusual reaction layers were found in the samples from the RIA-ST-1 and the RIA-ST-2 rods. Figures 25 through 27 show these samples. In Figure 25, a Zr-rich (U,Zr) alloy was not observed on the cladding inner surface. Unidentified phases were observed in Figure 26. In Figure 27, the apparent Zr-rich (U,Zr) alloy layer appears thick, and a grey-colored phase seems to exist between each duplex layer. These anomalous or unidentified layers may be produced by extremely high temperatures which change the reaction layer formation.

5.3.5 Cladding Embrittlement and Fracturing. The RIA-ST-1 and RIA-ST-2 fuel rods were severely oxidized and embrittled. The zirconium oxide and oxygen-stabilized α-zircaloy layers reduced the cladding ductility, and the embrittled cladding was readily fractured by the thermal stresses that occurred during quenching. The

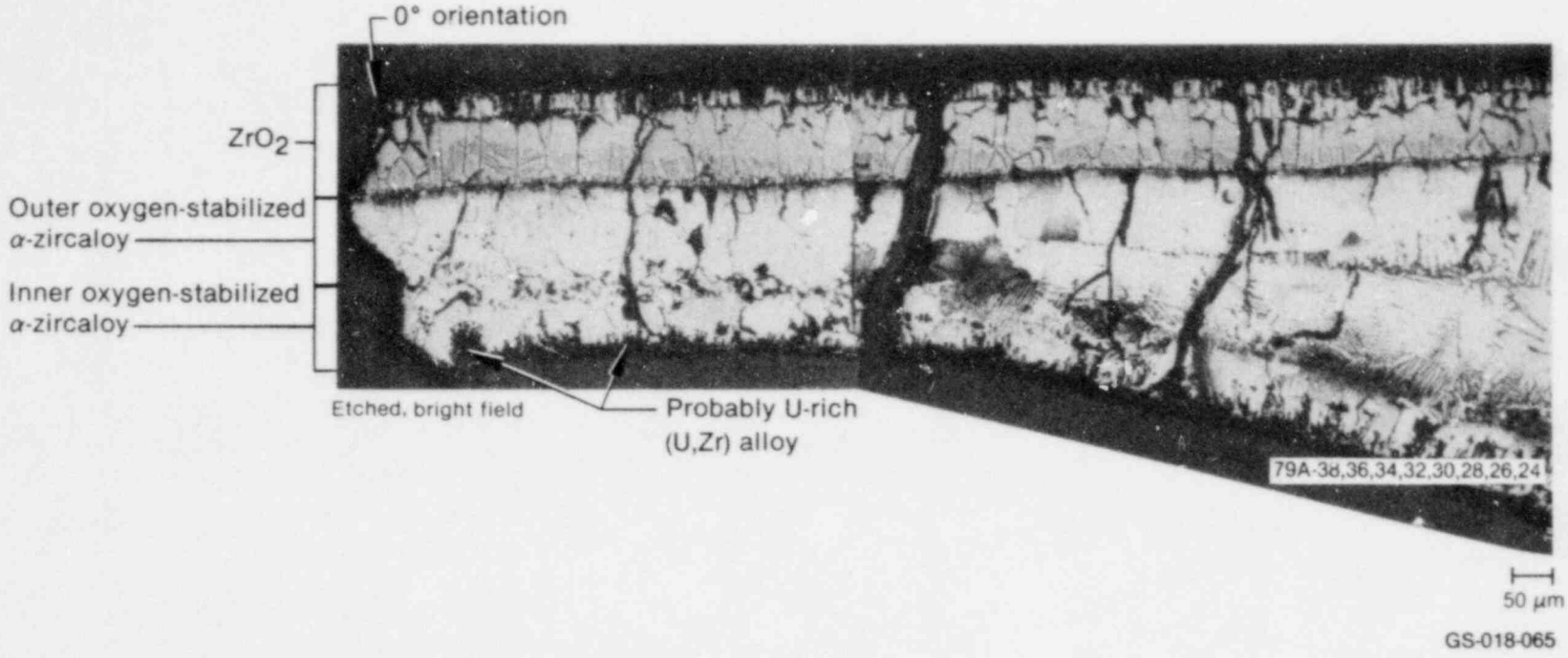

Figure 25. Cladding microstructure at the fracture tip in the RIA-ST-1 rod (250 cal/g axial peak radial average fuel enthalpy) at the 0.354-m elevation and the 0- to 20-degree orientation.

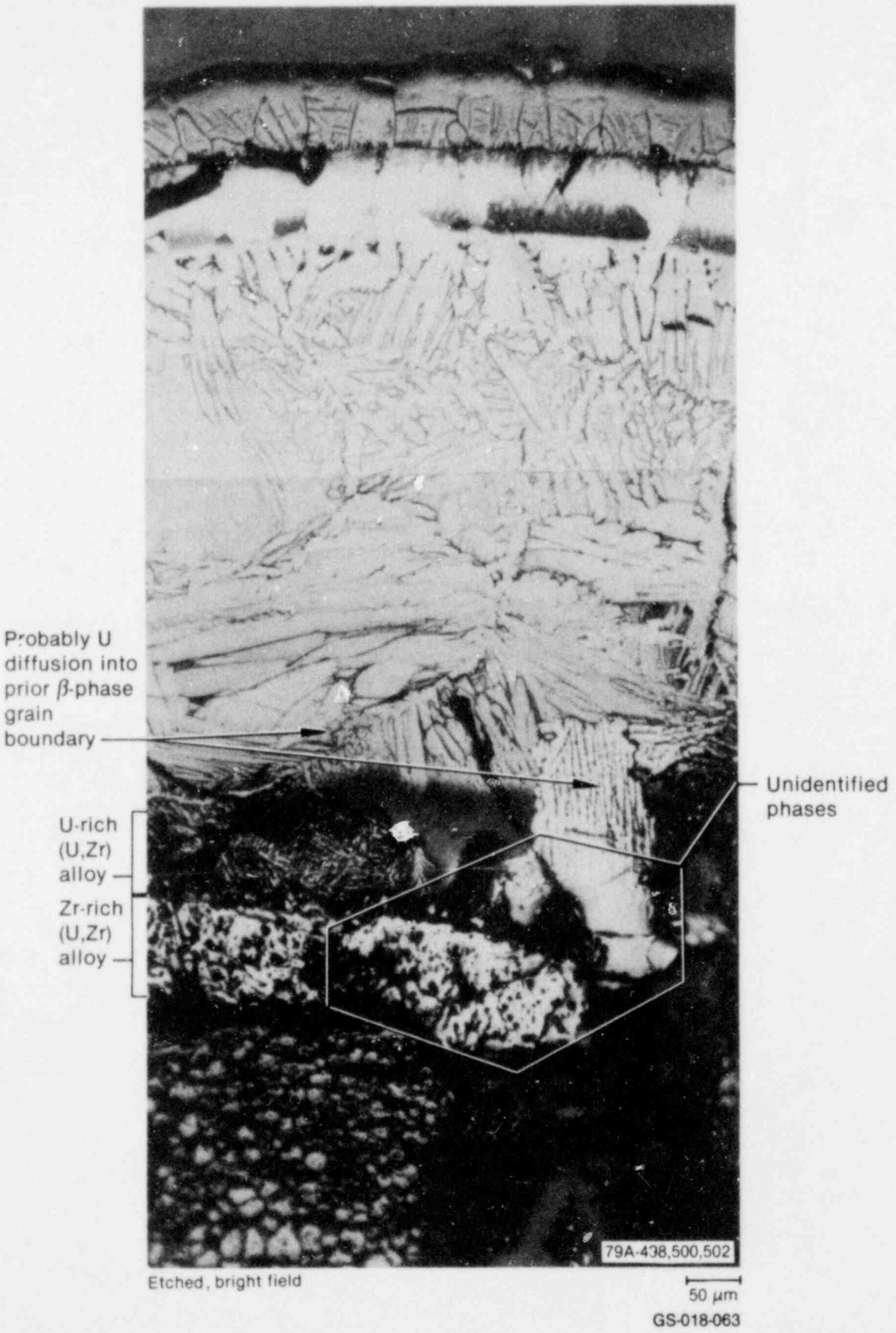

Figure 26. Cladding microstructure in the RIA-ST-2 rod (260 cal/g axial peak radial average fuel enthalpy) at the 0.33-m elevation and approximately the 0-degree orientation, showing abnormal UO_2-zircaloy reaction layers.

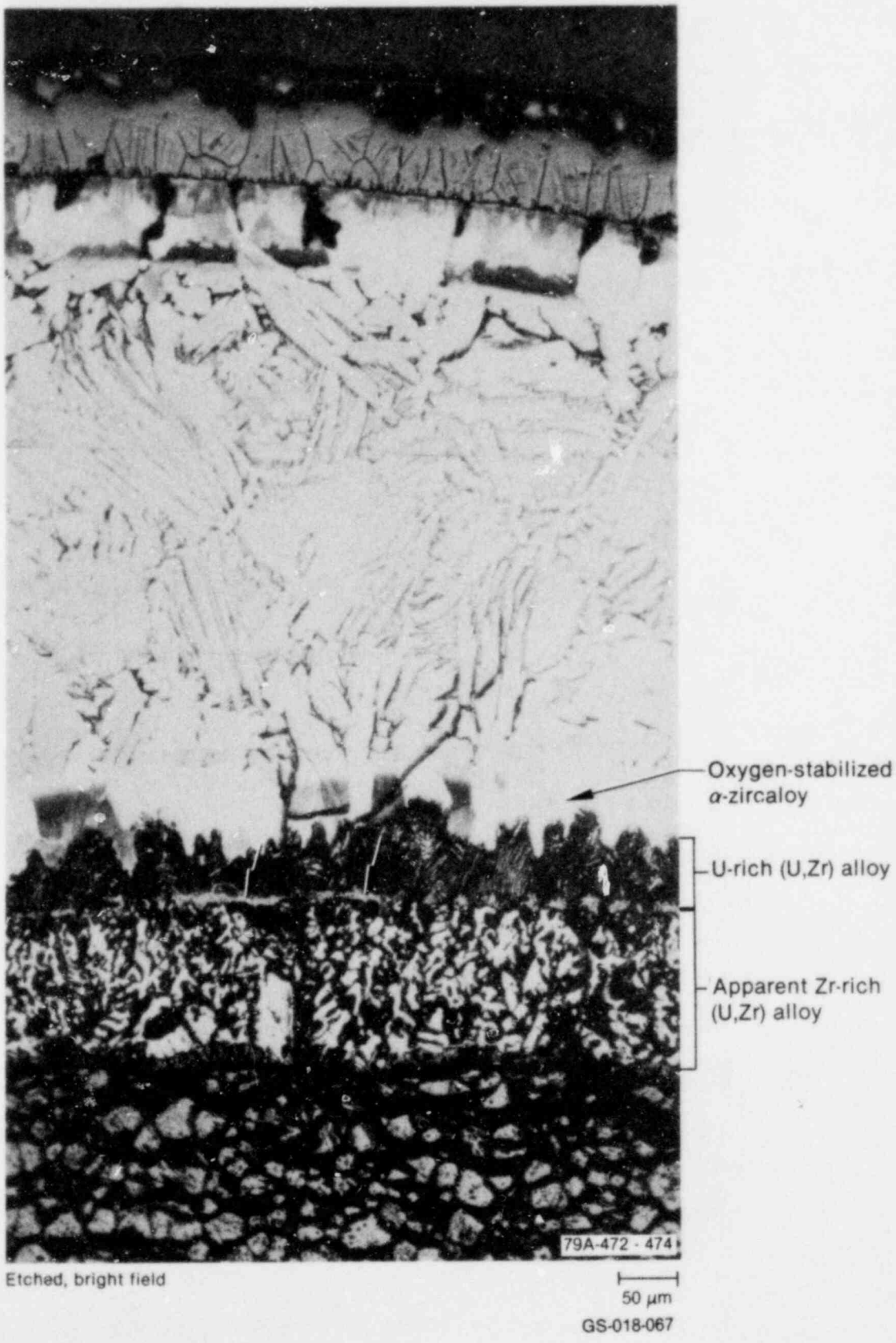

Figure 27. UO_2-zircaloy reaction layers in the RIA-ST-2 rod (260 cal/g axial peak radial average fuel enthalpy) at the 0.44-m elevation and the 330-degree orientation, showing abnormal reaction layer formation.

UO_2-zircaloy reaction produced cladding embrittlement to nearly the same extent as the zircaloy-steam reaction. Moreover, the UO_2-zircaloy reaction created a strong bond between the cladding and fuel, and prevented relative cladding-fuel movement. The resultant differential thermal strains and the temperature gradient that developed as the rod cooled contributed to the mechanical failure of the embrittled zircaloy. The data suggest that the cladding cracks formed as extensions of radial cracks in the UO_2 pellets, thus supporting the hypothesis of a fuel rod failure mechanism, due in part to a strong pellet-to-cladding bond. However, extensive fuel shattering and fuel washout prevented confirmation of this hypothesis.

Wall thinning is important to fuel rod failure by cladding embrittlement because oxygen pickup, and therefore embrittlement, is greater in the thinner regions. (As mentioned previously, the wall thickness variations occurred prior to significant oxidation.) If significant wall thickness variations did not occur, the ratio of oxide thickness to wall thickness would remain <0.2. On the basis of the existing cladding embrittlement criteria,[11] this ratio would indicate that complete cladding embrittlement should not occur. Thus, the quenching thermal stresses and the thermal differential strains between the bonded cladding and fuel could be accommodated in the ductile cladding.

The fuel rod failures in RIA-ST-1 and RIA-ST-2 occurred during or after the cladding quenched, as evidenced by the facts that (a) the fractures were brittle, (b) oxidation of the cladding fracture surfaces or the UO_2 fuel was not observed, and (c) SEM fractrographs revealed brittle, ceramic appearing fracture surfaces with transgranular cracking (Appendix C, "SEM Fractography").

5.3.6 Scenario of Cladding Damage. The process of cladding damage for the test rods subjected to power bursts producing axial peak radial average fuel enthalpies of 250 to 260 cal/g (275 to 290 cal/g UO_2 peak enthalpy near the fuel surface) can be summarized as follows. Plastic flow of the cladding produced regions of wall thickening and thinning. The zircaloy was then oxidized by steam and UO_2 and completely embrittled in the thinner regions. Upon quench from film boiling, cracks were produced in the embrittled cladding due to thermal stresses and differential cladding and pellet thermal strains.

5.3.7 Fuel Restructuring. The RIA-ST-1 and RIA-ST-2 fuel rods exhibited limited equiaxed fuel grain growth, as quantified in Table 13. Figure 28 shows the relationship between grain size and fuel enthalpy as a function of pellet radial position determined from these scoping tests. In general, grain growth depends on time and temperature and, assuming the fuel temperature histories are similar in each case, larger grains mean higher fuel temperature.

Fuel melting and columnar grain growth were not observed in these rods, although the peak enthalpies were estimated to be near or greater than the enthalpy required for UO_2 melting. That melting and grain growth were not observed does not necessarily mean that the fuel temperatures did not exceed the UO_2 melting point. FRAP-T5 indicated that the UO_2 melts, but the molten fuel resolidifies in less than 5 s. This may be an insufficient time to produce the typical fuel restructuring that is characteristic of molten fuel, such as central void formation and the formation of large, nearly pore-free grains upon solidification.

Fuel shattering (UO_2 grain boundary separation) was observed in some specimens, as shown in Figure 29. The data in Table 13 indicate that complete fuel shattering occurred for axial peak radial average fuel enthalpies of >230 cal/g (>255 cal/g axial peak), and that partial shattering was observed for axial peak radial average fuel enthalpies greater than ~185 cal/g (205 cal/g peak). Although some fracturing and fragmenting of the fuel was expected to occur during preconditioning and during the power burst, most of the granular shattering was caused by the rapid cooling as the rods quenched. This time sequence is supported by the correlation in Figure 28 between grain growth, which would have to occur prior to fragmentation, and fuel enthalpy. The NSRR data indicate that shattering occurs only in regions where fuel-cladding chemical interaction results in bonding between the pellets and cladding. This hypothesis indicates that the fuel shattering observed in the RIA-ST rods resulted from the thermal stresses induced by rapid cooling upon quenching from film boiling, the same mechanism discussed by Cronenberg and Yackle.[12]

Figure 29 (previously discussed) and Figure 30 show representative porosity distributions from the RIA-ST-3 and RIA-ST-1 rods, respectively. The largest pores were located on the grain boundaries, especially at grain boundary intersections

TABLE 13. UO_2 FUEL RESTRUCTURING IN RIA-ST-1, RIA-ST-2, AND RIA-ST-3

Test	Location (m from bottom of fuel stack)	Radial Average Local Fuel Enthalpy (cal/g)	Radial Peak Local Fuel Enthalpy (cal/g)	Grain Size (μm)			Extent of Grain Boundary Shattering
				Edge	Middle	Center	
RIA-ST-1	0.294	230	255	18	24	28	Complete
RIA-ST-1	0.446	245	270	20	30	40	Complete
RIA-ST-1	0.354	245	270	21	40	a	Complete
RIA-ST-2	0.44	260	290	20	30	a	Complete, but not in the central region
RIA-ST-3	0.416	225	250	18	20	28	None
RIA-ST-2	0.72	185	205	15	17	20	Partial (within 0.5 mm from periphery)

a. Not measured.

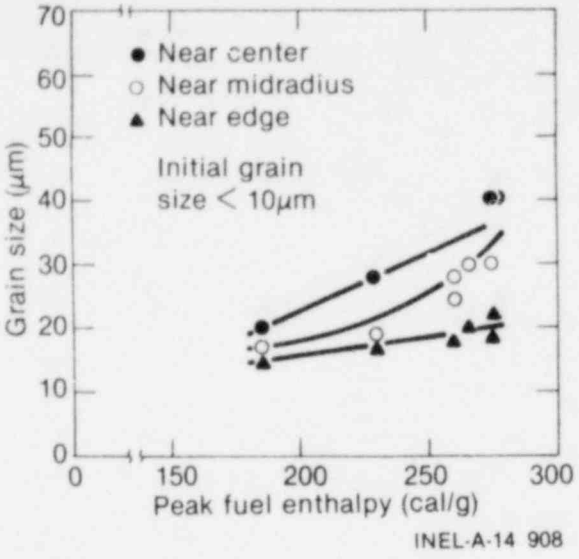

Figure 28. Relationship between UO_2 grain size and peak fuel enthalpy as a function of radial location in the fuel for RIA-ST-1 and RIA-ST-2.

(triple points), which are energetically favorable sites. Pore migration was not extensive because of the short period of high temperature operation in these RIA tests. Pore-free grains were not observed. Fairly large pores were probably scattered along the grain boundaries, thereby contributing to the loss of grain boundary strength, but such pores were no longer visible because of the grain boundary shattering discussed previously.

5.4 Summary of Postirradiation Examination of RIA-ST-1, RIA-ST-2, and RIA-ST-3 Fuel Rods

FRAP-T5 calculations indicated that the RIA-ST-3 fuel rod (225 cal/g axial peak radial average fuel enthalpy, 250 cal/g axial and radial peak) reached a peak fuel temperature of about 3000 K and a peak cladding temperature of about 2098 K, or very near the melting point. The rod was calculated to be in film boiling for about 21 s. As a result, the rod exhibited bowing, cladding collapse, waisting, and ridging. The outer surface of the rod had an apparent double oxide layer over 95% of the fuel stack length, with some oxide spalling of the outer layer. The inner cladding surface had an alloy duplex layer consisting of a U-rich layer and a Zr-rich layer. Partial melting of the inner alloy layer was indicated.

The hypothesized scenario of the cladding deterioration for RIA-ST-3 is as follows. The cladding expanded initially due to thermal expansion of the fuel prior to significant cladding temperature increases. This resulted in an overall rod diameter increase, ridging at the pellet interfaces, and probably bowing due to nonuniform circumferential deformation of the cladding. As the cladding heated up and lost mechanical strength, there was significant collapse over nearly the entire fuel region, especially at the pellet interfaces (waisting). The zircaloy oxidized on both the inner and outer surfaces; however, the embrittlement due to oxidation was not complete, and fuel rod failure did not occur as a result of the thermal stresses upon quenching.

Fuel restructing in RIA-ST-3 was characterized by limited grain growth throughout the fuel. Radial fuel fracturing occurred upon fuel rod quench.

FRAP-T5 calculations for the axial peak radial average fuel enthalpies reached in RIA-ST-1 and RIA-ST-2, 250 and 260 cal/g (275 and 290 cal/g UO_2 axial and radial peak), indicated that the peak fuel and cladding temperatures for these transients were the respective melting temperatures. As a result of the transients, the rods, in addition to the damage experienced by the RIA-ST-3 rod, exhibited radial cladding ovality changes, waisting, and extensive wall thickness variations. The RIA-ST-1 and RIA-ST-2 rods failed in the central high power region, showing massive oxidation, spalling, cladding splitting and fracture, and cladding ridging. A large amount of fuel was absent from these two rods (~10% from RIA-ST-1 and ~15% from RIA-ST-2), and wall thickness variations were indicated near the peak flux regions.

The inner and outer cladding reaction layers were similar to those of the RIA-ST-3 rod, but more extensive. In the thin-wall regions, the oxygen stabilized α-layer was extensive, and complete embrittlement occurred in these regions. The through-wall cracks were determined to have occurred during or after the rods quenched.

The hypothesized scenario of cladding deterioration for the RIA-ST-1 and RIA-ST-2 fuel rods is as follows. Plastic flow of the cladding produced regions of wall thickening and thinning. The zircaloy was then oxidized by steam and UO_2 and completely embrittled in the thinner regions.

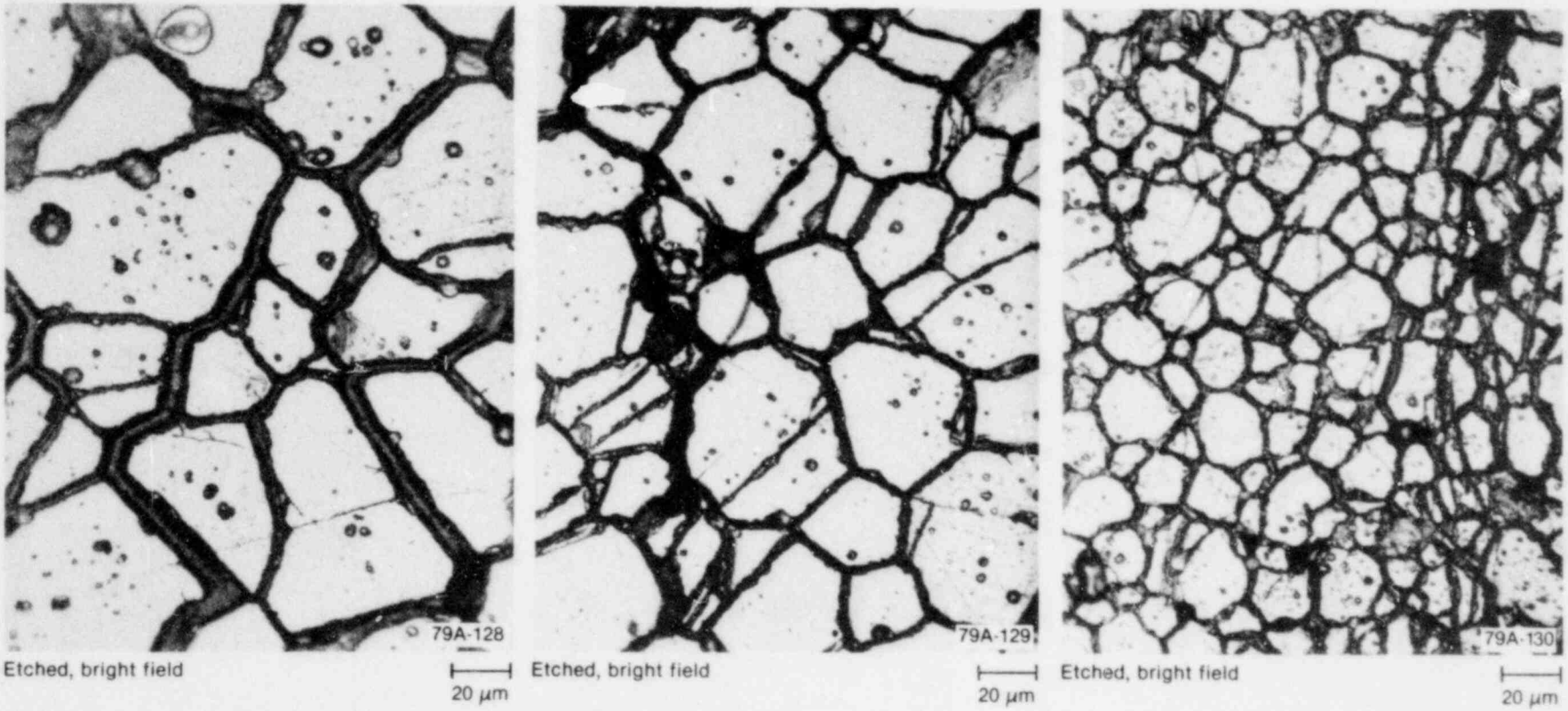

Figure 29. Fuel restructuring in the RIA-ST-1 rod (250 cal/g axial peak radial average fuel enthalpy) at the 0.446-m elevation and the 0-degree orientation, showing grain growth, fuel shattering, and porosity distribution.

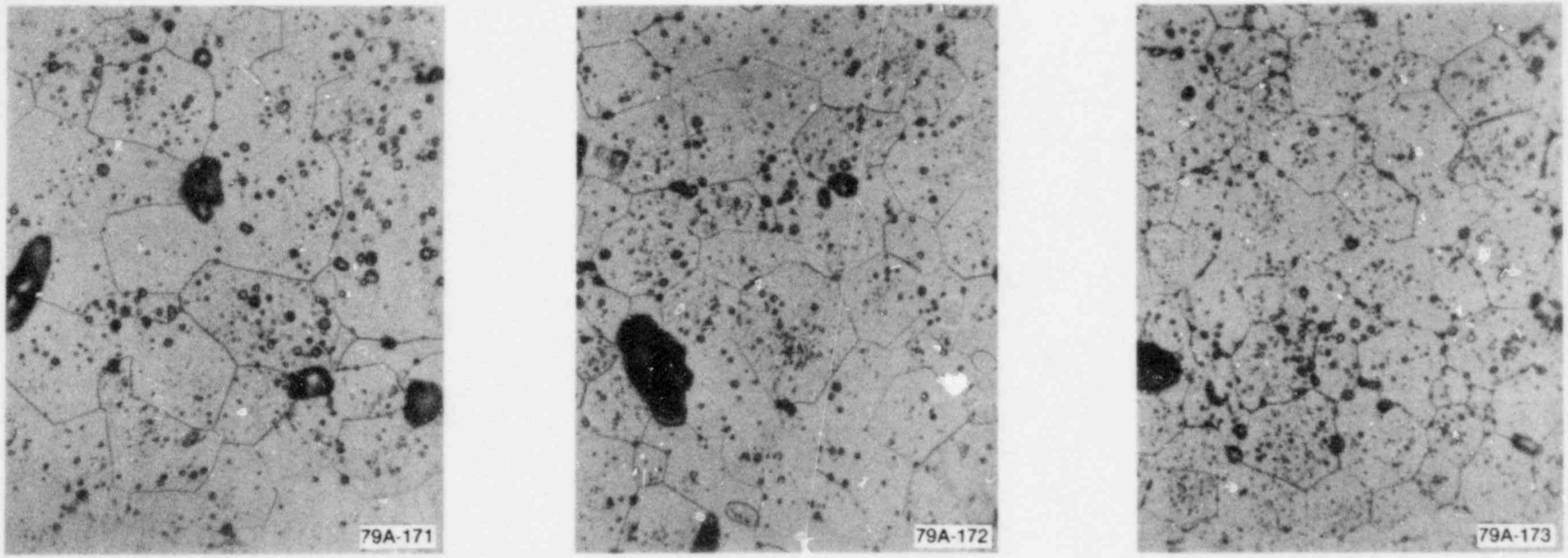

Figure 30. Fuel porosity distribution in the RIA-ST-3 rod (225 cal/g axial peak radial average fuel enthalpy) at the 0.416-m elevation and the 0-degree orientation.

Upon quench from film boiling, cracks were produced in the embrittled cladding due to thermal stresses and differential cladding and pellet thermal strains.

Fuel restructuring in RIA-ST-1 and RIA-ST-2 was characterized by limited equiaxed grain growth. There was no evidence of fuel melting, although the fuel may have reached the melting temperature of UO_2 for a short time. Fuel shattering was observed in the higher energy deposition specimens. Large pores were apparently present on grain boundaries and triple points, although they were obscured by fuel shattering. Pore migration was not extensive, however, and no pore-free grains were observed.

On the basis of the relative appearances of the three fuel rods, the axial and radial peak fuel enthalpy threshold for cladding failure was judged to be ~265 cal/g (240 cal/g axial peak radial average fuel enthalpy).

6. INSTRUMENT SENSITIVITY TO HIGH RADIATION BURSTS

The third objective of the RIA Scoping Tests was to determine the relative sensitivities of test instrumentation to high radiation exposure during a power burst. Several environmentally isolated instruments were added to the test train specifically for instrument sensitivity evaluation.

1. The 69-MPa EG&G Idaho pressure transducer was a bellows-strain post type device which is normally used to measure coolant pressure in the area of the test train, as well as large pressure transients in the in-pile tube. When pressure is applied to the bellows of this transducer, the attached strain post compresses slightly, causing the geometry of the strain gages bonded to the strain post to change. This compression induces a change in resistance, proportional to the pressure applied to the transducer.

   The 69-MPa EG&G Idaho free field pressure transducer was located at the lower test train mounting plate. It was sealed and backfilled with helium to a cold pressure of 2.07 MPa. The signal output of the instrument was recorded on two channels of the PBF/DARS at different frequencies: a narrow band (10 Hz) and a wide band (5 kHz). The instrument provided data for the first three bursts of the RIA Scoping Tests, but failed prior to the remaining experiments. Figure 31 illustrates the typical output of the instrument recorded on the narrow band. The typical output recorded on the wide band was similar.

   The expected response of a sealed transducer to temperature variation of the enclosed gas is given by

   $$P_2 = P_1 (T_2/T_1)$$

   where P_1 is the backfill pressure and T_2/T_1 is the ratio of gas temperature to room temperature. Prior to the transient, with an internal gas pressure at the coolant temperature of 538 K, this transducer should read about 3.75 MPa based on a cold backfill pressure of 2.07 MPa. An offset in the output was observed both on the wide band and the narrow band. The offsets were different in each, which suggests that they were due to errors in the PBF/DARS calibrations and were not malfunctions or errors in the transducer. Figure 31 shows an offset of ~4.3 MPa.

   At transient peak power (zero seconds), there was only a small indication of radiation burst sensitivity effects, as indicated by the figure (a total variance of ~0.13 MPa). This indicated change in pressure was probably due to a combination of temperature response and the response of the instrument and wiring to the intense gamma and neutron flux. The heating effect is indicated by the change in the baseline before and after the power burst. The EG&G Idaho 69-MPa free field pressure transducer appears to be suitable for use in future RIA testing.

2. The 17.2-MPa EG&G Idaho pressure transducer, like the 69-MPa EG&G Idaho transducer, was a bellows-strain post type. This 17.2-MPa transducer is normally used to measure coolant pressure in the in-pile tube. One 17.2-MPa EG&G Idaho pressure transducer, located on the upper support bars of the test train, was sealed and backfilled with helium to a cold pressure of 2.07 MPa and used in the RIA Scoping Tests.

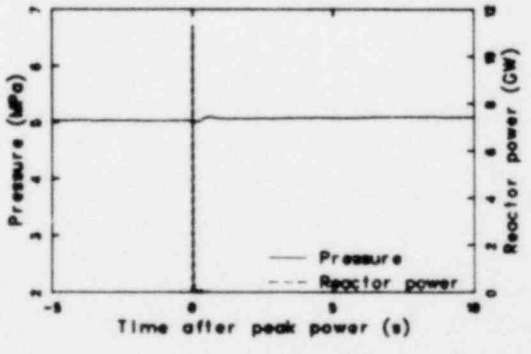

Figure 31. Narrowband output for the 69-MPa EG&G Idaho pressure transducer (10 Hz) during RIA-ST-1, Burst 2, showing sensitivity to radiation burst.

The signal from this instrument was recorded on a narrowband channel. Figure 32 shows the typical response of this transducer. The expected initial output of this transducer at 538 K was 3.75 MPa. There is an indicated offset of approximately 10 MPa, which occurred prior to the instrument being exposed to a high radioactive environment. This shift is most probably due to an error in the calibration of the PBF/DARS. The instrument output during each burst was influenced by the high radiation fluxes, but the radiation effects were nonhysteretic. The apparent change in pressure due to each burst was on the order of 0.25 MPa. This was probably caused by the intense gamma and neutron flux bombarding the transducer and wiring. The indicated change in transducer output could be caused by various electrical charges produced in the transducer and wiring.

3. The 17.2-MPa Kaman Sciences Corp., pressure transducer is normally used to measure plenum gas pressure in test fuel rods and coolant pressure. It uses a principle of impedance variation. This variation is dependent on the generation and decay of eddy currents within a conductive plate suspended at the end of the sensor. The eddy currents are generated by an active coil near the sensing diaphragm. As pressure is applied to the sensing diaphragm, the distance between the sensor and the active coil decreases, and the magnitude of the eddy current increases. In order to compensate for undesired environmental effects, an inactive coil is used; with both coils as components of the impedance bridge. The manufacturer claims this transducer is very insensitive to radiation and temperature effects. "Temperature causes changes of most physical properties of the materials used in the sensor and cabling, but both halves of a symmetrical design respond to these changes in a similar manner." This self-compensation is only attained once thermal equilibrium within the sensor is reached.

   A 17.2-MPa Kaman Sciences Corp., transducer was installed on the fuel rod upper shroud extension. It was sealed to eliminate any response due to coolant pressure changes and backfilled to a cold pressure of 2.07 MPa. Its signal was recorded on a narrowband channel during RIA-ST-1 and is shown in Figure 33. Although this sensor's expected signal was about 3.75 MPa at 538 K prior to the burst, not enough data are available to determine whether the offset to 11.5 MPa occurred because of a PBF/DARS calibration error or an error in the sensor itself. The small change (on the order of 0.1 MPa) observed during the transient, is probably due to the high neutron and gamma fluxes.

4. The 17.2-MPa Bell & Howell pressure transducer was a sputtered strain gage

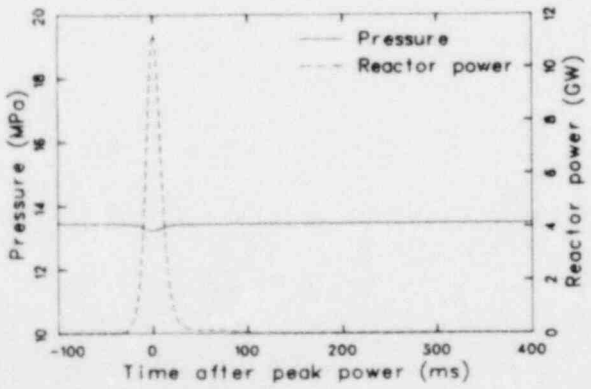

Figure 32. Narrowband output for 17.2-MPa EG&G Idaho pressure transducer (10 Hz) during RIA-ST-1, Burst 2, showing sensitivity to radiation burst.

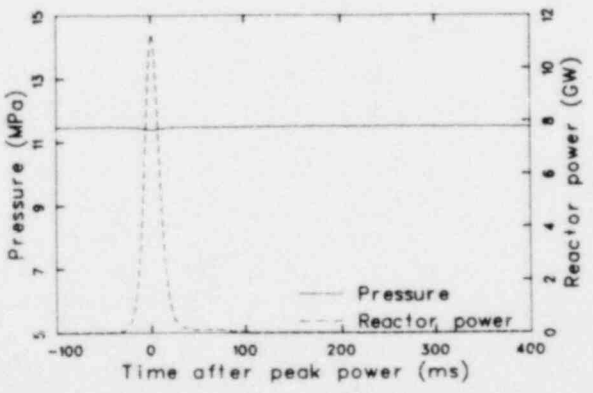

Figure 33. Narrowband output for 17.2-MPa Kaman Sciences Corp., pressure transducer (10 Hz) during RIA-ST-1, Burst 2, showing sensitivity to radiation burst.

type which would normally be used to measure coolant pressure. Strain gages are sputtered (a metal deposition process) directly onto the pressure diaphram of the transducer. External pressure deflects the diaphragm, producing a resistance change in the strain gage bridge.

One 17.2-MPa Bell & Howell pressure transducer was located at the lower end of the hanger rod for the RIA Scoping Tests. The radiation-induced signal of this instrument was recorded on a wideband channel for the first four bursts. Its typical output is shown in Figure 34. Again, the instrument shows an offset in the initial pressure indication. This offset may be due to an error in the PBF/DARS calibration. The pressure transducer shows a slight response to the burst (< 0.1 MPa), but appears to behave predictably in the radiation environment.

5. The 17.2-MPa Schaevitz Engineering pressure transducer was installed at the fuel rod upper shroud extension. It was added to the test train for evaluation, although the LVDT-type pressure transducer had not been previously used in the PBF. For RIA-ST-1, the pressure transducer was connected via a small-diameter tube to the source pressure region inside the flow shroud. A damaged transducer lead resulted in water intrusion which rendered the device useless; therefore, no data were obtained to evaluate it.

6. The EG&G Idaho linear variable differential transformer is normally used to measure cladding elongation. In future RIA tests it will also be used to measure fuel stack elongation. The EG&G Idaho LVDT is an electro-mechanical device which produces an electrical output proportional to the displacement of a movable magnetic core. This output is generated by the changes in the coupling between the primary and secondary windings of a transformer. Gamma heating in the LVDT can cause change in sensitivity, phase shift, zero shift, magnetic field breakdown, and melting or structural failure.[13]

In the RIA Scoping Tests, an EG&G Idaho LVDT with a blocked armature was located outside the flow shroud extension in the flow bypass region at approximately the same elevation as the active LVDT. The blocked armature of this device eliminated the possibility of observing change in sensitivity or phase shift due to gamma heating, since these effects are functions of the input to the LVDT.

Figure 35 shows the typical response of this device, recorded on a wideband channel. Although there seems to be a zero shift in its output, it cannot be attributed to radiation and/or temperature change since it occurs before the burst and it remains the same throughout the test. Again, the zero offset must be assumed to

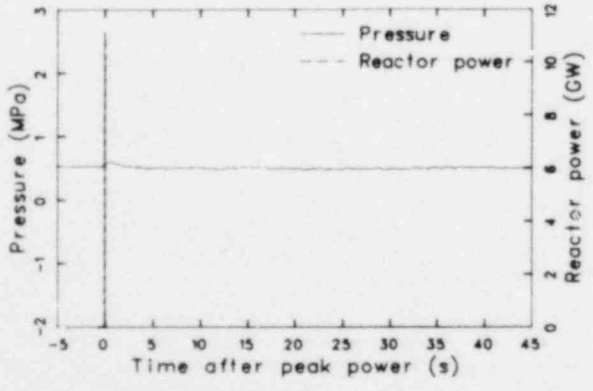

Figure 34. Wideband output for 17.2-MPa Bell & Howell pressure transducer (5 kHz) during RIA-ST-2, showing sensitivity to radiation burst.

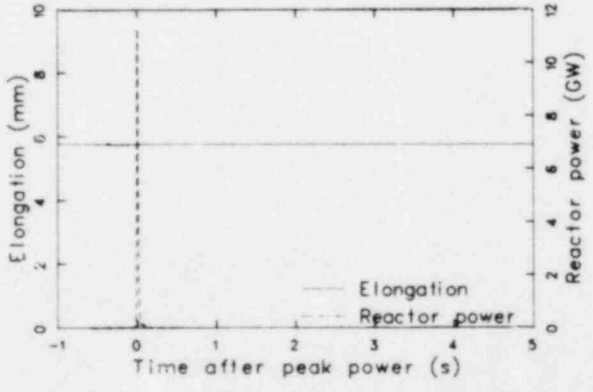

Figure 35. Wideband output for EG&G Idaho LVDT (5 kHz) during RIA-ST-1, Burst 2, showing sensitivity to radiation burst.

be to due an error in the PBF/DARS calibration. During the burst, the LVDT shows no radiation sensitivity.

7. Two Ailtech Type MG125 strain gages were welded directly onto the shroud of the RIA-ST test train. One was mounted circumferentially, and the other was mounted longitudinally. Strain gages are not often used in PBF testings. They are basically wire or foil devices which experience a change in electrical resistance under strain. These devices are usually fastened to a structure so that they exhibit a change in resistance in proportion to the changes in structural shape under stress. The strain gage measurement system consists of a transducer, a bridge completion unit, a power supply, and an amplifier. The strain gages in the RIA Scoping Tests were three-wire units which were connected to a function module where bridge completion was made. The output of the function module went to a Newport Model 80 signal conditioner which was operated in a constant voltage mode.

   The signal outputs of these strain gages were recorded on narrowband channels for RIA-ST-1 only. Figure 36 illustrates the response to a radiation burst for the longitudinally oriented gage. The response of each gage was nominally identical. The magnitude of the strain response for each transducer corresponded to the radiation intensity of each burst. The large magnitude of the responses and the fact that the responses of the circumferential and longitudinal gages were identical indicates that they were a measure of the gage radiation sensitivity and not shroud strain. The response was probably due to the intense gamma and neutron bombardment of the gages. The manufacturer reports a significant change in resistance related to radiation exposure, and suggests the use of special thermally aged, matched pairs of gages, which will track one another for radiation-induced changes.

8. One EG&G Idaho titanium sheathed, magnesia insulated, platinum-platinum, 10% rhodium thermocouple was located outside the flow shroud, at the axial power peak during RIA-ST-1. The Type S thermocouples are normally used to measure test fuel rod cladding temperatures. A thermocouple consists of two wires of different metals fastened together at the ends. The voltage measured across a break in one of the wires is a function of the temperatures of the two junctions and of the types of metal used in the wires. The general procedure is to hold one of the junctions at a fixed reference temperature (~340 K) and use the voltage across the other junction as an indication of its temperature. The response times of thermocouples depend strongly on junction size, heat transfer, and the particular application of the thermocouple.

   The data recorded by this device, shown in Figure 37, are mainly responses to

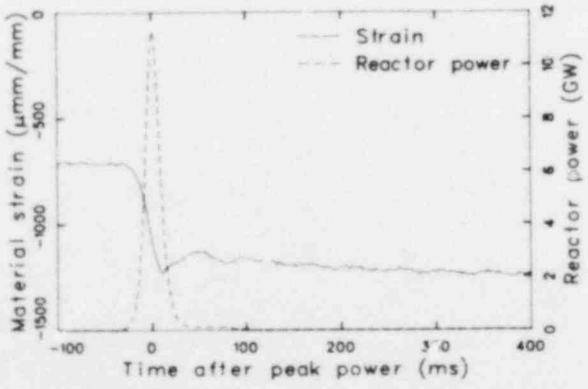

Figure 36. Narrowband output for longitudinally oriented Ailtech strain gage (10 Hz) during RIA-ST-1, Burst 2, showing sensitivity to radiation burst.

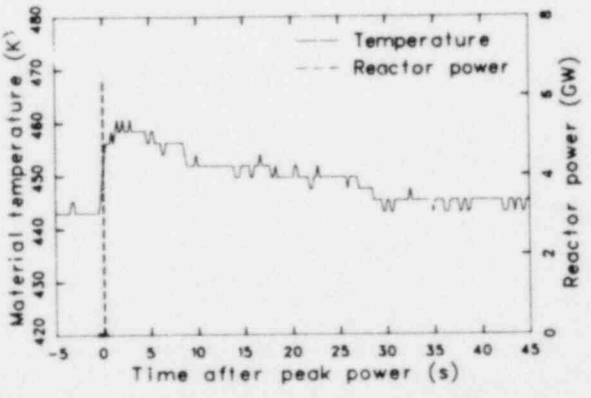

Figure 37. Output for EG&G idaho Type S thermocouple during RIA-ST-1, Burst 1, showing sensitivity to radiation burst.

temperature because the trend they follow is typical of the test train temperature. No radiation effects were detectable.

9. In addition to the instruments intended primarily for radiation sensitivity evaluation, information was obtained on the behavior of two Flow Technology turbine flowmeters during each burst. These flowmeters are primarily used to monitor flow shroud or bundle coolant volumetric flow rates. Turbine flowmeter operation is based on the reluctance principle. According to this principle, reluctance of the flux path between a magnet and a coil changes when a ferrous object approaches the pole face of a magnet. In the turbine flowmeter, the reluctance detector is located near the rotating blades of the turbine. As each blade passes the detector, the reluctance flux path between the magnet and coil of the detector is reduced, and a voltage is induced in the coil. As the blade moves away, the flux path increases, and the induced voltage decreases, producing a voltage sinusoid. The number of voltage peaks is directly proportional to the rotation rate of the turbine. The flowmeter signal conditioning counts the number of peaks over a given time interval to establish the rate of turbine rotation and, therefore, coolant flow. Validity of the volumetric flow measurement is largely dependent on flow conditions. With homogeneous, single-phase flow, the flowmeter measures volumetric flow with minimal uncertainty. Two-phase flow conditions greatly increase that uncertainty.

   The typical response of the shroud inlet flowmeter to the RIA power transients is shown in Figure 38. The coolant flow was expected to reverse at the shroud inlet, passing through stagnation and reaching a negative flow rate significantly higher than the positive peak indicated in Figure 38. The flow response is shown positive in the figure because the flowmeter was unidirectional and negative flow was indicated as positive. That the response does not reach zero flow at any time or peak at the expected flow rate is due to the long time constant for the signal conditioning which averages flowmeter rotor pulses to determine flow rates. The response of this instrument during an RIA test could be improved by shortening the time constant of the signal conditioner.

To summarize the results of the instrument sensitivity investigation, all the pressure transducers behaved well in the RIA transient environment. The EG&G Idaho LVDT and Type S thermocouple showed no indication of radiation sensitivity. Because of gamma heating in the coolant and the gamma radiation bombardment of the instrument elements, the strain gages displayed significant transient sensitivity. A problem with flowmeter output was also observed, but this was because of the relatively slow transient response of the flowmeter signal conditioning. No indication of radiation sensitivity was identified.

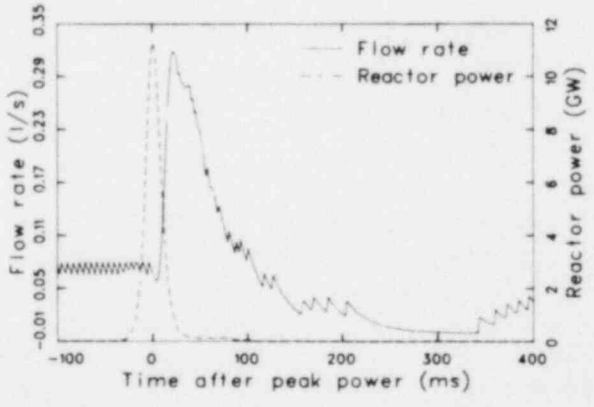

Figure 38. Wideband output for shroud inlet flowmeter (20 kHz) during RIA-ST-1, Burst 2, showing sensitivity to radiation burst.

7. CONSEQUENCES OF VERY HIGH ENERGY DEPOSITION IN A LIQUID FILLED SYSTEM (RIA-ST-4)

The fourth objective of the RIA Scoping Tests was to determine the magnitudes of potential pressure pulses and the potential for molten fuel-coolant interaction (MFCI) resulting from inadvertent high energy rod failure in the PBF liquid filled test loop. The test consisted of a power transient with a total energy deposition of 695 cal/g UO_2 at the axial flux peak, which is at least 2.5 times more energy deposition than is possible in a commercial reactor during an RIA. The RIA-ST-4 fuel rod failed approximately 3 ms after peak power when the radial average energy deposited to the fuel was 360 cal/g. The axial peak radial average fuel enthalpy calculated by FRAP-T at this time was 350 cal/g. Preliminary analyses of the large magnitude pressure pulse obtained when the test rod failed indicate that a molten fuel-coolant interaction may have been the cause of pressurization and expansion of the coolant, resulting in a severe hydraulic transient. The analyses indicated that neither fuel vapor pressure nor the work potential of the helium fill gas could account for the impulse transient required to sustain the maximum pressurization measured at the axial peak power elevation and at the flow shroud inlet.

7.1 RIA-ST-4 Pressure Measurements and Introduction to the Analyses

RIA-ST-4 is the only known UO_2-water, high energy deposition, fuel failure experiment performed at system pressures and coolant flows typical of present-day boiling water reactors. Therefore, it is of particular interest to the ongoing discussion of MFCI potential. A few UO_2-water MFCI experiments have been reported in the literature in which molten UO_2 was dropped into a pool of subcooled water at atmospheric pressure. Of particular importance here is the fact that because of redundant safety features in present commercial LWRs, the probability of a reactivity initiated accident occurring with energy depositions similar to those of RIA-ST-4 is negligibly small. However, the performance of such high energy experiments certainly enhances the understanding of MFCIs.

The time-dependent response of the four RIA-ST coolant pressure transducers, together with reactor power, illustrates simultaneous pressurization ~4 ms after peak power occurred. The location of the four pressure transducers on the test train for RIA-ST-4 is illustrated in Figure 39. The transducer responses are shown in Figure 40. The peak pressure, pressure increase, and rise time results from the four pressure transducers used in the experiment are summarized in Table 14. The 17-MPa Bell & Howell pressure transducer, connected by a 3.2-mm-diameter tube to the flow shroud at the axial location of peak power, should have yielded the best indication of source pressure resulting from rod failure. However, this transducer saturated at 22.3 MPa and therefore did not indicate the actual peak pressure. The best indication of the source pressure was that obtained from the 69-MPa EG&G Idaho pressure transducer located in the inlet section of the flow shroud; it indicated a maximum pressure of 34.6 MPa. The source pressure, however, would be larger than the pressure measured at the shroud inlet, depending on the propagation characteristics of the pressure pulse in the flow shroud. Therefore, the system had to be modeled analytically, and both the experimentally measured results and the calculated behavior had to be used to estimate the source pressure-time history in the molten fuel-coolant interaction zone. The peak pressure measured by the upper plenum and flow bypass transducers was less than 9 MPa, which indicates that significant attenuation of the pressure pulse occurred due to the propagation from the shroud to the upper plenum and bypass regions.

Knowledge of the pressurization characteristics in the source region is of primary interest in (a) evaluating possible damage to the PBF flow tube in which the RIA-type tests are performed and (b) extrapolating test results to other systems such as actual reactor vessels. Accurately extrapolating test results in a quantitive manner to other systems is not straightforward. For example, pressure pulse characteristics are geometry dependent and, therefore, cannot usually be translated to another system. The usual practice is to first estimate the mechanical work done on the system, and then estimate the associated

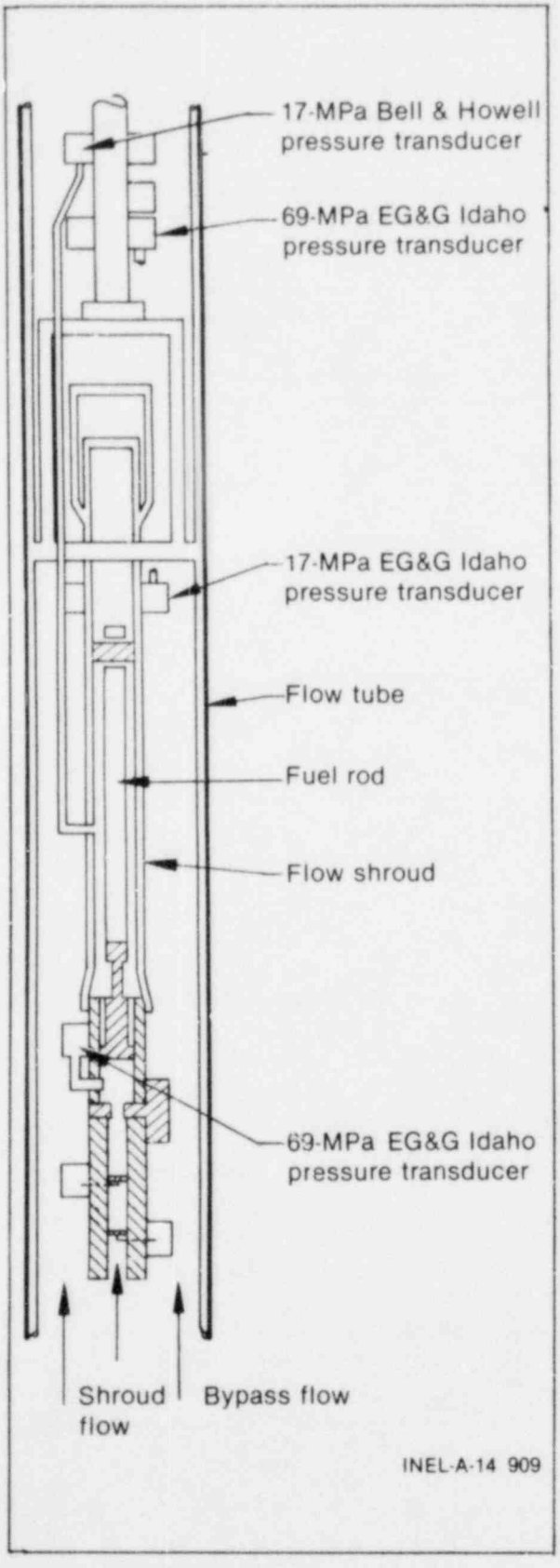

Figure 39. Illustration of the RIA-ST test train.

mechanical-to-nuclear conversion ratio. The conversion ratio can then be used to better extrapolate the test results to other systems. Normally, for an RIA, the nuclear energy deposition is equated to the fuel rod enthalpy rise, and the mechanical work done on the system is estimated from the change in coolant kinetic energy upon rod failure, interpreted from inlet and outlet flowmeter data or from the piston motion of a linear motion transducer. Since RIA-ST-4 was not instrumented to determine changes in coolant kinetic energy, analysis of the pressure-time history was required to determine this quantity from the following equation:

$$A\int P(t)dt = I$$

$$\Delta KE = \frac{I^2}{2m}$$

where

I = impulse of pressure = $\int F(t)dt$

F = force

ΔKE = change in kinetic energy

A = cross-sectional area upon which pressure is acting

$P(t)$ = pressure time history

m = mass of coolant acted upon.[a]

The change in kinetic energy determined from the pressure history was then divided by the average nuclear energy deposited in the fuel element by the time of failure to obtain the mechanical-to-nuclear conversion efficiency for comparison with similar conversion efficiencies from other experiments.

The consequences of molten fuel-coolant interactions can be either (a) benign if a significant fraction of the interaction region is a compressible void (noncondensable gases or vapor),[14,15] or (b) severe if the heat transfer process is sufficiently rapid (for example, due to coherent fine-scale fuel fragmentation and intermixing with the coolant) that a significant fraction

a. The mass of the coolant acted upon is an assessed variable, based on acoustic relief considerations.

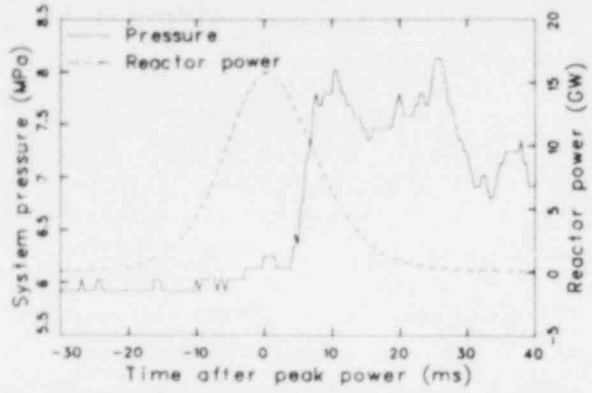

(a) Time-dependent response to power transient of 69-MPa EG&G Idaho upper plenum pressure transducer

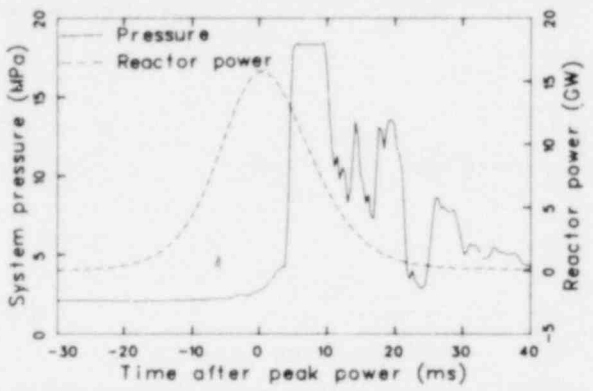

(b) Time-dependent response to power transient of 17.2-MPa Bell & Howell source region pressure transducer

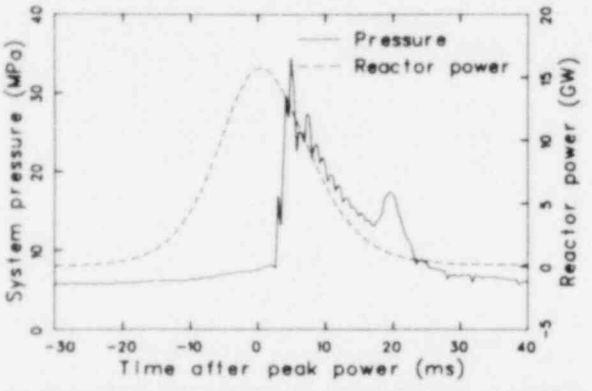

(c) Time-dependent response to power transient of 69-MPa EG&G Idaho shroud inlet pressure transducer

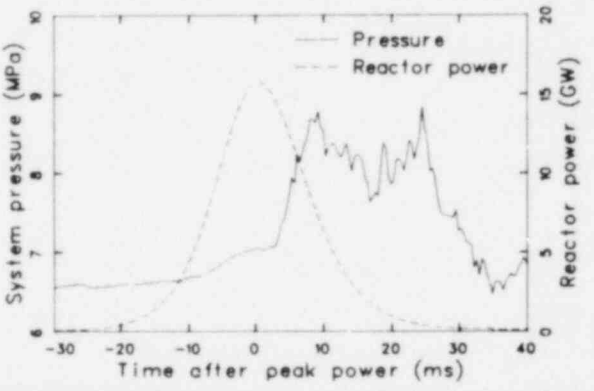

(d) Time-dependent response to power transient of 17.2-MPa EG&G Idaho flow bypass pressure transducer

Figure 40. Illustration of simultaneous pressurization at 3 ms after peak power.

of the fuel thermal energy is transferred to the coolant.[16,17,18] If such a rapid heat transfer process indeed results before the system responds (that is, pressure relief by coolant expansion), the potential exists for a thermally induced destructive event. In general, such a process has been termed a vapor explosion, since coolant vapor is considered to be the working fluid.

Although the details of various vapor explosion model concepts may differ, a consensus of opinion is emerging on the necessary condition for triggering a vapor explosion, namely,[19,20]

1. Initial coarse intermixing of fuel with coolant, characterized by a period of stable film boiling

2. Destabilization of film boiling

3. Intimate contact between molten fuel and coolant

4. Extensive fine-scale fuel fragmentation and intermixing with liquid coolant, resulting in a large effective heat transfer area causing rapid, coherent coolant vaporization

5. Sufficient system constraint such that pressurization occurs.

Thus, the fuel rod thermal conditions at the time of rod failure (for example, amount of molten fuel and cladding), the thermodynamic condition (that is, vapor or liquid) of the working fluid at the time of failure, and the amount of fuel fragmentation occurring as a result of rod failure in a flowing coolant environment must be known to assess whether the above-mentioned initial conditions favoring an energetic MFCI are met.

An assessment of the pressure-time history in the MFCI zone, an estimate of the kinetic energy from the time of fuel rod failure, an assessment of

TABLE 14. PRESSURE DATA FROM RIA-ST-4 POWER BURST

Pressure Transducer	Location	Pressure Increase (MPA)	Total Peak Pressure (MPa)	Rise[a] Time	Comments
17-MPa B&H	Source region	15.9	22.3	20 MPa/ms[b]	Saturated; most direct measurement
69-MPa EG&G Idaho	Shroud inlet	28.2	34.6	1.6 ms	Second most direct measurement
69-MPa EG&G Idaho	Upper plenum	2.1	8.5	3 ms	Second least direct measurement
17-MPa EG&G Idaho	Flow bypass	1.8	8.2	4 ms	Least direct measurement

Approximate pressure in test section region = 6.4 MPa

Coolant critical pressure = 22.1 MPa

a. Defined as the time from 10% to 90% of transient response.

b. The 90% value could not be determined accurately, so the rate of change of pressure has been given.

the conditions of the working fluid at the time of failure, a discussion of the posttest metallurgical analysis which yields information on fuel fragmentation, and, finally, a discussion of the results are provided in the following sections.

7.2 Assessment of the Source Pressure

The pressure transducer connected to the inside of the flow shroud at the position of maximum neutron flux (that is, source region) appeared to have saturated at 22.3 MPa. Thus, the actual pressure in this region must have been greater than 22.3 MPa, and somewhat above the critical pressure of water (22.1 MPa). To assess the pressure wave propagation from the source region, WHAM, a numerical code for calculation of pressure transients in complex liquid filled piping networks, was used. A discussion of the fluid dynamics model and the associated simplifying assumptions used in the WHAM code is presented in Appendix D (provided on microfiche attached to the inside of the back cover).

To accurately assess the pressure wave propagation, one must adequately model the piping network, taking into consideration all flow bypasses and changes in area and flow stream directions, understanding whether and where compressible and incompressible regions exist. The essential feature of the pressure propagation problem is that in the axial center of the test section (where failure and initial pressurization are assumed to have occurred) there is a source region from which the pressure wave originates and travels outward. At constricted downstream areas, pressure waves are reflected and travel back toward the source region, as illustrated in Figure 41. Two different bounding situations can be envisioned, however,

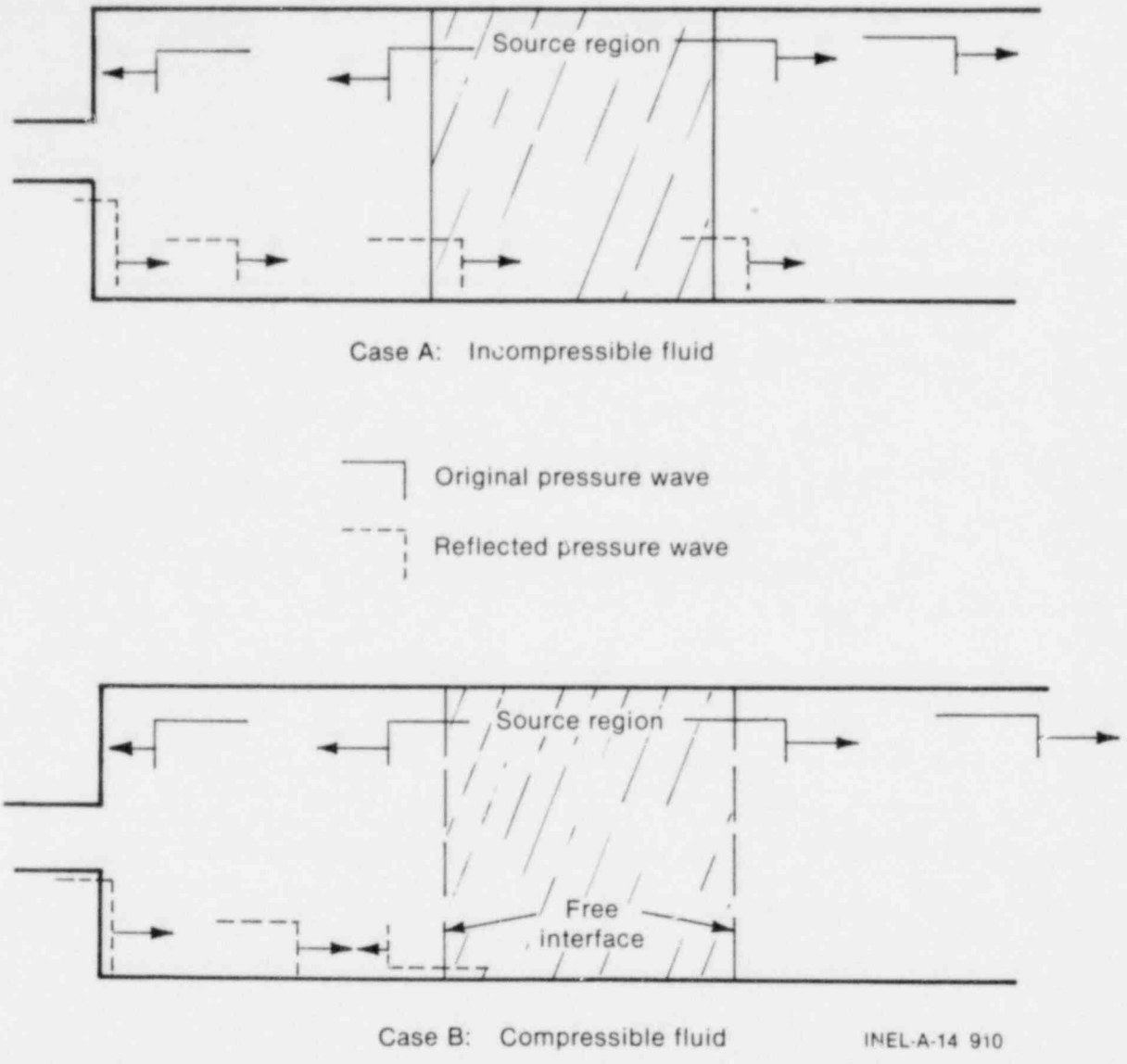

Figure 41. Illustration of pressure wave propagation and reflection characteristics for incompressible and compressible source regions.

depending on whether the source region is considered compressible (either vaporized fuel, coolant, He-bond gas, or a gaseous critical fluid) or incompressible (liquid coolant or a dense critical fluid). In the latter case, in which the source region is a dense fluid, the reflected waves propagate through the source region, as illustrated in Figure 41(a). However, if it is postulated that the source region is compressible, then the reflected waves that reach the boundaries of the gaseous region are re-reflected. The boundaries of the compressible region can be approximated as a free interface. Thus, there are two bounding situations, depending on the compressibility of the source region, that can be expected to give different pressurization results. Since the thermodynamic phase of the working fluid in the test section is unknown, the two bounding situations were considered.[a]

The WHAM code piping network is illustrated in Figure 42. The WHAM model of the RIA-ST-4 test train incorporates the actual lengths and flow cross-sectional areas of all the piping elements, out to the inlet and exit thermal swell accumulators (TSAs). Since fluid density cannot vary with pipe region in the WHAM code, the density of the entire modeled piping network was

a. Although a free surface can be modeled at the end of a fluid column with the WHAM code, an intermediate compressible fluid leg cannot.

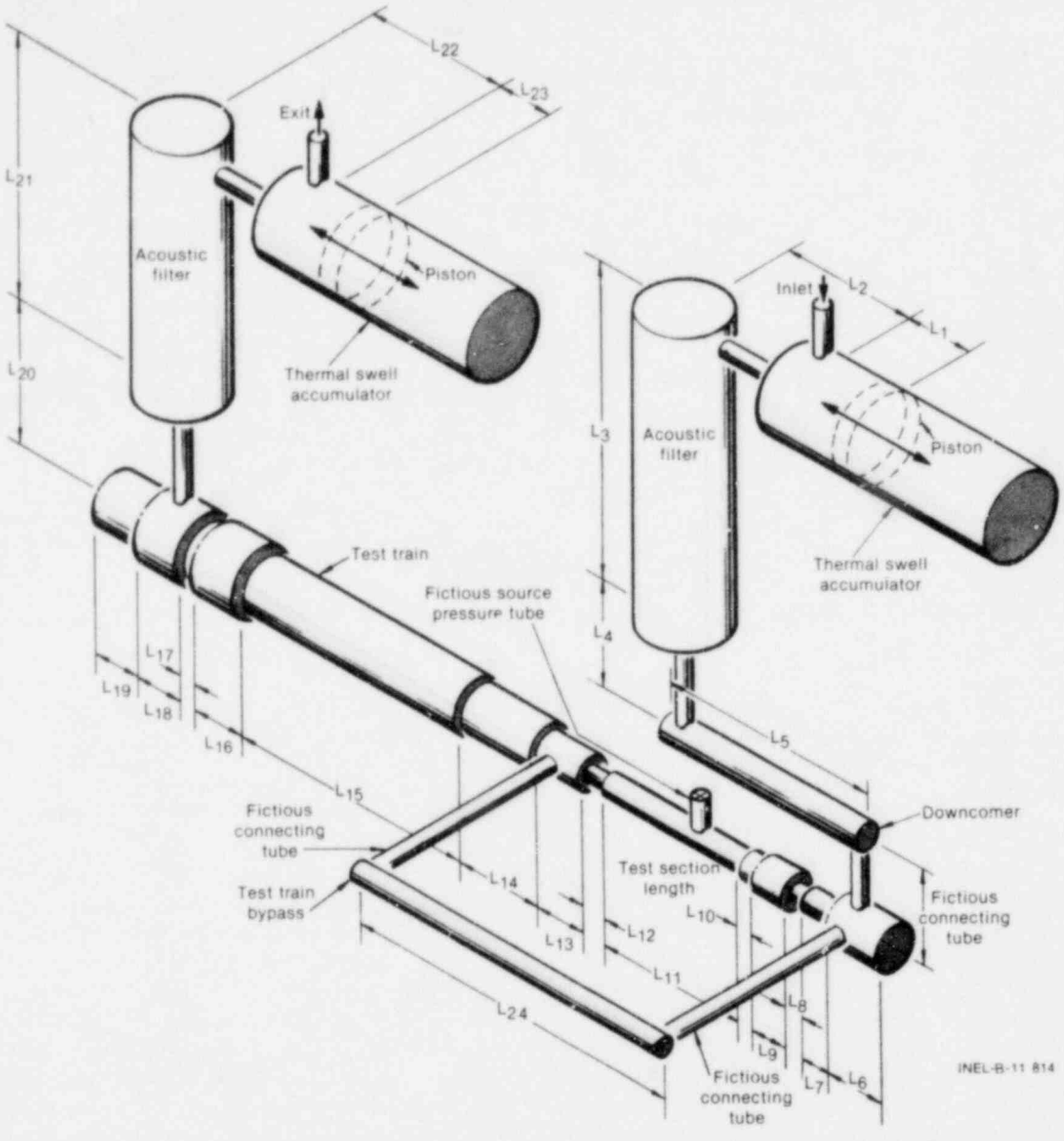

Figure 42. Mockup of the RIA-ST-4 piping network.

considered liquid in both cases, and the source region either ideally incompressible or compressible. The piston in each TSA is designed to respond to a minimum pressure differential of about 0.07 to 0.14 MPa. In WHAM, the TSA piston was simply modeled as a massless piston with a backpressure of 6.55 MPa. The piston was free to respond in either negative or positive directions.

7.2.1 Incompressible Fluid in Source Region. Considering the source region to be incompressible (Figure 41), thus allowing for communication of reflected pressure waves through the source region, the estimated source pressure characterization that gave the closest comparison to the recorded pressure data at the upper and lower pressure transducers is as illustrated in Figure 43. The assumed source pressure, which peaked at 37 MPa, had a rise time of 2 ms, and a decay to system pressure time of 20 ms, resulted in favorable comparison between the calculated and measured response pressures. This good agreement is illustrated in the comparison between the actual measured pressure histories at the upper and lower pressure transducers and their calculated histories for the assumed source pressure pulse shown in Figure 44.

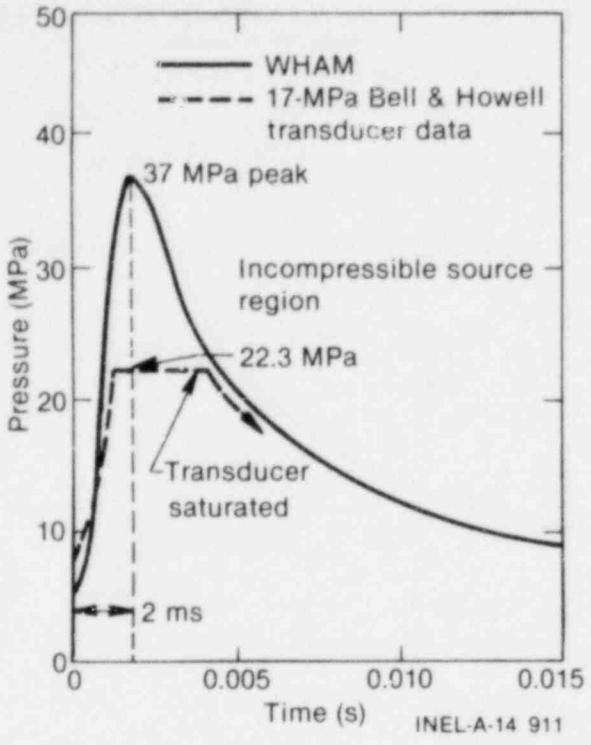

Figure 43. Comparison of the assumed source pressure pulse characteristics (WHAM) and those obtained from pressure transducer data (incompressible case).

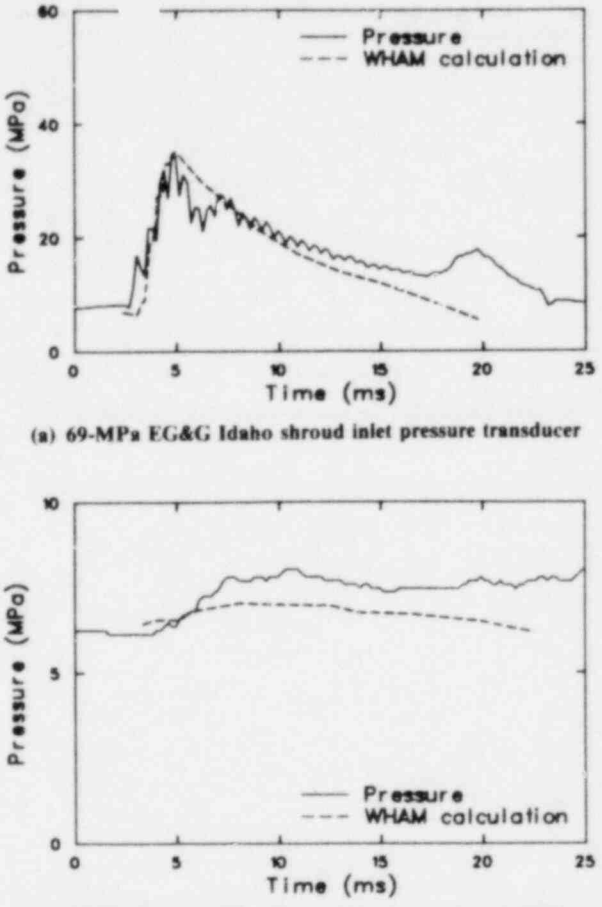

(a) 69-MPa EG&G Idaho shroud inlet pressure transducer

(b) 69-MPa EG&G Idaho upper plenum pressure transducer

Figure 44. Comparison of the assessed and measured pressure characteristics for the shroud inlet and upper plenum pressure transducers.

7.2.2 Compressible Fluid in Source Region. The exact nature of the compressiblity of the source region during the 20-ms pressurization event is uncertain. In the previous calculation it was assumed that the source region was incompressible (that is, a dense fluid) such that pressure waves could freely travel through the source region. However, immediately following fuel rod rupture, noncondensible He-bond gas, fuel vapor, coolant vapor, and/or supercritical gaseous coolant may be present in the source region, such that the region boundaries can be best modeled in the WHAM code[a] as free interfaces. Reflected pressure waves from downstream and upstream area contractions would then be negatively[b,21] re-reflected, as illustrated in Figure 41(b). Assuming that the source region is ideally compressible [bounded by two free interfaces from which pressure waves are reflected negatively rather than transmitted, as in Figure 41(a)], a somewhat higher source pressure is required to account for the measured pressures at the upstream and downstream transducers. The responses of two pressure transducers are compared with the WHAM results in Figure 45, indicating that a pressure peak of approximately 52 MPa would produce pressure characteristics somewhat similar to those measured by the source region and shroud inlet sensors. However, the comparison is not as good as for the incompressible case.

A compressible source region will result in a higher estimate of the impulse and corresponding kinetic energy imparted to the coolant than a noncompressible source region. Therefore, a conservative order-of-magnitude estimate of the mechanical work (kinetic energy) done on the system by the pressure transient can be obtained using the 37-MPa pulse, which will give the lowest energy conversion ratio.

a. Only two cases can be considered in the WHAM code, either with free interfaces (compressible region) or completely incompressible regions.

b. Reflected waves from blunt, solid surfaces (walls) double in magnitude at the wall but are reflected in a positive one-to-one manner in an ideal incompressible fluid, whereas pressure waves are reflected from free interfaces in a negative manner.

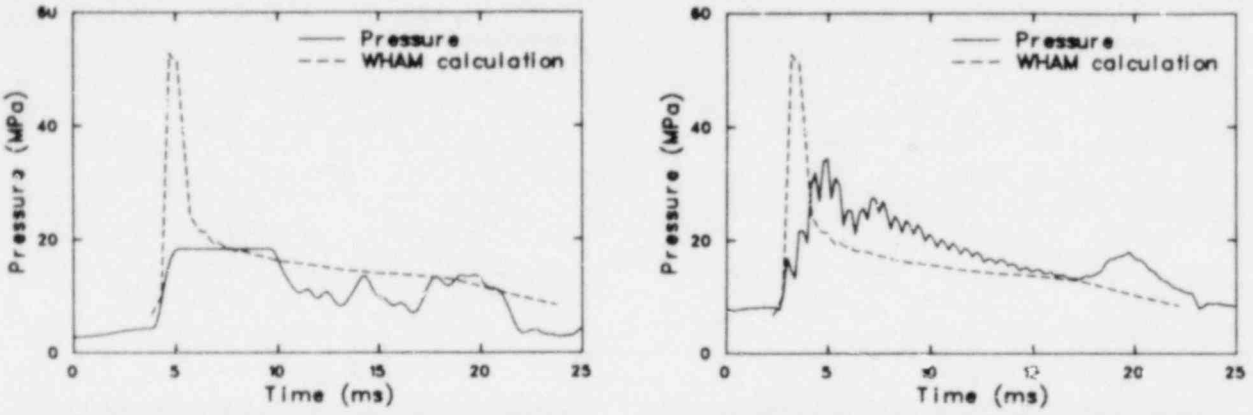

(a) 17.2-MPa Bell & Howell source region pressure transducer

(b) 69-MPa EG&G Idaho shroud inlet pressure transducer

Figure 45. Calculated (WHAM) source pressure characteristics for an ideally compressible source region and comparison with the lower pressure transducer measurements.

7.3 Assessment of Kinetic-Energy from Impulse

A rough estimate of the kinetic energy imparted to the system, due to pressurization, can be obtained using simplifying assumptions concerning the fluid flow characteristics, if the pressure-time history and the mass which is acted upon are known. Considering the following schematic diagram, the flow is considered uniform if the velocity and direction of flow do not change at a particular cross-sectional area from point-to-point (say from A to C). The flow is unsteady if the velocity at a particular point (say B) changes with time, as for a fluid undergoing acceleration due to rapid pressurization. During the RIA-ST-4

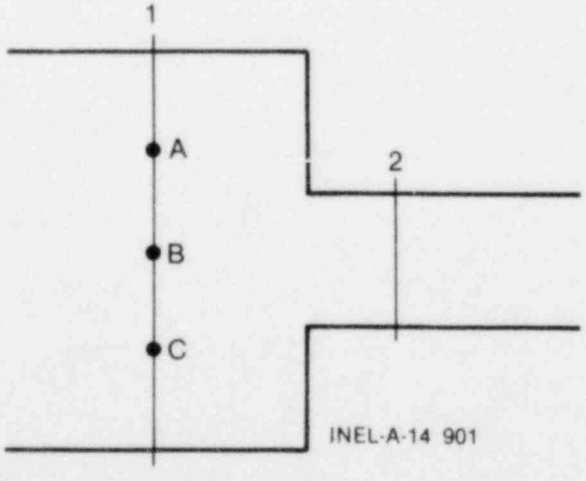

pressure transient, the liquid is assumed to be ideal (incompressible) and the flow unsteady, uniform, and one-dimensional. The conservation of total mass[a] over a time period from Region 1 to Region 2 is used. The density of the fluid is assumed to be constant and the initial coolant velocity is assumed to be negligible. On the basis of these assumptions, the following equation for the average change in kinetic energy was derived for cross section 1, then used to assess the KE of other sections.

$$\Delta KE_1 = \frac{[A \int P(t)dt]^2}{2m_1}$$

where the terms are as defined previously.

It was assumed that two slugs of water were acted upon by the pressure pulse, namely, the water above the rod failure region and the water below the rod failure region. For the 37-MPa pressure pulse in the interaction zone, P(t)dt over the entire 20-ms pulse period was 0.18 MPa·s. Using this value of the integral, the changes in kinetic energy of the upper and lower water slugs are

$$\Delta KE_U = 2910 \text{ cal}$$

$$\Delta KE_L = 6760 \text{ cal}$$

and the calculated total change in kinetic energy is 9670 cal.

a. This assumption is subject to question, since significant fluid mass may be forced out of the test section length during the 20-ms pressure transient.

7.4 Mechanical-to-Nuclear Energy Conversion Rate

The RIA-ST-4 fuel rod failed 3 ms after the time of peak power; the time of the initiation of the pressure pulse. At this time the radial average energy deposition at the peak power elevation was approximately 345 cal/g or 255 cal/g axially averaged over the length of the fuel rod. The total mass of UO_2 in the rod was about 630 g. Therefore, the total nuclear energy contained in the fuel rod at the time of the pressure pulse was 1.60×10^5 cal. Using the value for the total change in kinetic energy (9670 cal) results in a mechanical-to-nuclear energy conversion ratio of 6.0%. The largest mechanical-to-nuclear energy conversion ratio determined for the CDC-SPERT tests was 1.8%.[22]

7.5 Assessment of Fuel Rod Thermal Conditions at Failure

The FRAP-T5 code was used to estimate the thermal condition of the fuel and cladding at the time of failure using the best-estimate total energy deposition of 695 cal/g. The power burst axial peak radial average fuel enthalpy at the time of failure was approximately 350 cal/g. Although the energy deposition is highest at the fuel surface (R_f = 4.65 mm), the temperature of the fuel reaches a maximum slightly interior to the surface at a radius of about 4.19 mm. This is due to the fact that the fuel heating is not completely adiabatic and heat loss occurs from the fuel surface to the cladding and to the interior portions of the fuel pellet. The temperature condition of the fuel, as predicted by the FRAP-T5 code, at the time of fuel rod failure is shown in Figure 46. A maximum temperature of about 3740 K was calculated by FRAP-T5. The code also predicted that film boiling would occur prior to the time of failure. Therefore, the thermal condition of the fuel rod at the time of failure was probably that of molten fuel. Consequences of fuel rod failure during such a condition are strongly dependent on the thermodynamic state of the working fluid surrounding the failing fuel rod, which is the topic of the following discussion.

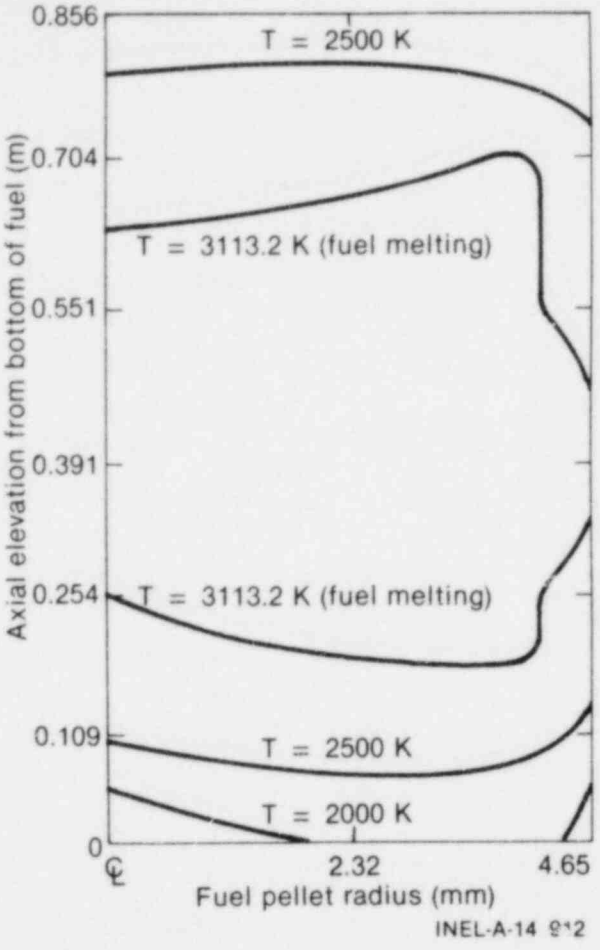

Figure 46. Illustration of the fuel rod temperature condition at time of failure for RIA-ST-4, as predicted by the FRAP-T5 code.

7.6 Assessment of the Working Fluid

There are basically three possible working fluids which could be present in the flow shroud to interact with molten fuel debris expelled from the test rod upon failure: (a) water, or a mixture of water and water vapor; (b) fuel vapor; and (c) fuel rod fill gas.

Rapid heating of an initially subcritical liquid (water) due to an MFCI can lead to the formation of a supercritical fluid prior to the initial relief of the constraining system, with subsequent vapor formation during the expansion process of the working fluid. This can be illustrated by considering the pressure-enthalpy diagram for steam and water shown in Figure 47. For conservative considerations, a constant volume pressurization process, followed by a constant enthalpy expansion process of the working fluid against the constraining system is assumed. For the case in which the working fluid is purely water (illustrated by the x = 0 line in the figure), the coolant becomes

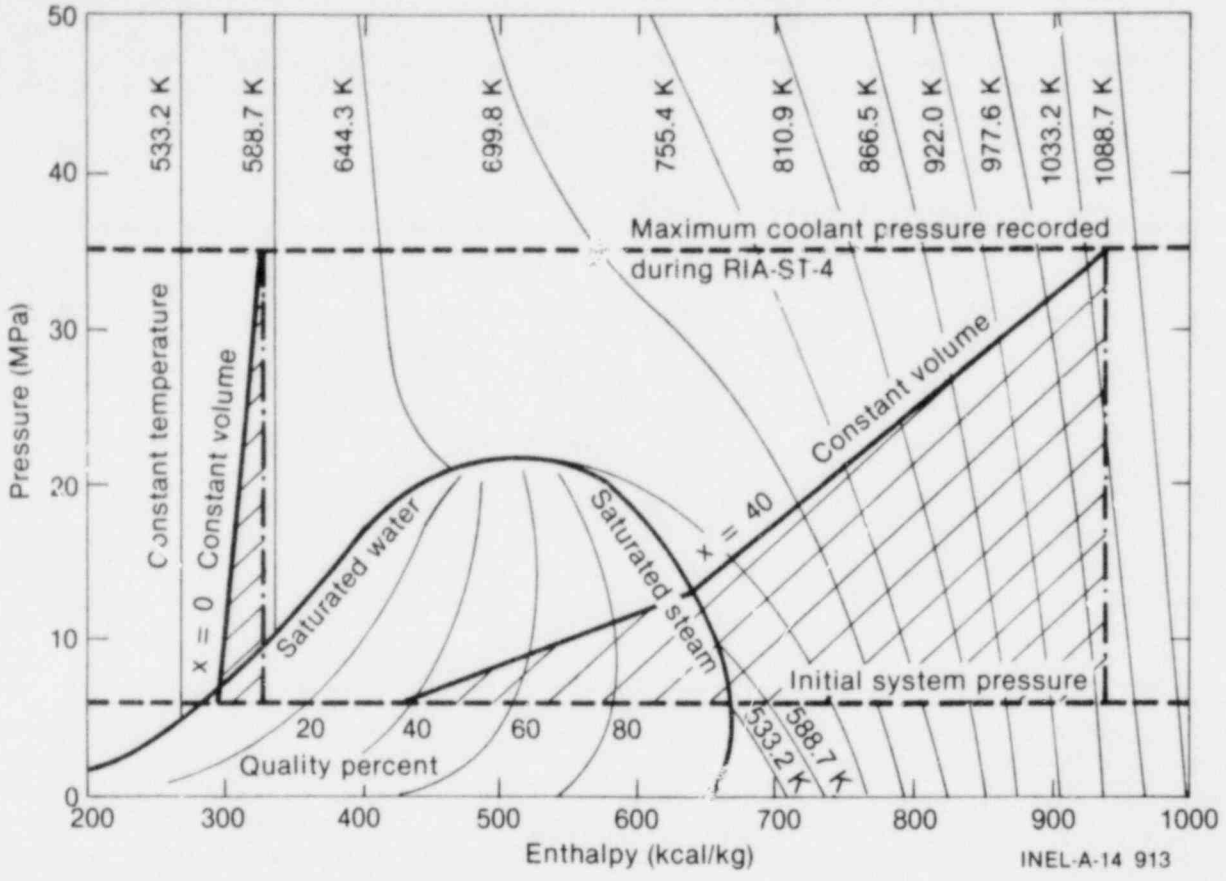

Figure 47. Thermodynamic surface for coolant which experiences MFCI heatup and pressurization above the critical pressure (P_c), and subsequent expansion to the vapor regime.

supercritical as the pressure increases to 35 MPa, at which point the corresponding fluid temperature is about 629 K (this temperature is less than the critical temperature of the water, 647 K). The working fluid will then expand back adiabaticaly to the system pressure at a temperature equal to the saturation temperature of the coolant, 555 K. At the end of the expansion process (illustrated by the dash-dot line in Figure 47), the working fluid becomes a mixture of water and saturated steam with a quality of 5%.

For the case in which the working fluid is initially a mixture of water and water vapor at the time of failure, with a steam quality of 40% (illustrated by the quality x = 40 line in the figure), the temperature of the working fluid at the end of the pressurization process to 35 MPa is about 1033 K. During such pressurization processes, the working fluid is superheated steam as soon as the pressure exceeds the saturated steam line, whereas for the zero quality case, the working fluid was a supercritical liquid at 35 MPa. When the superheated steam expands adiabatically back to system pressure, the steam temperature is reduced to 966 K.

The second case, in which the working fluid is initially a mixture of water and water vapor, best fits the RIA-ST-4 conditions because (a) the working fluid in RIA-ST-4 was a mixture of water and water vapor during film boiling, and (b) a temperature in excess of 940 K was recorded 470 ms after fuel failure by a thermocouple installed at the exit to the flow shroud. A working fluid which begins as a mixture of steam and water and is pressurized to superheated steam, causing shock pressurization of the flow shroud, is consistent with the sequence of events that occurred during RIA-ST-4, including the high coolant temperature measured following the relief of the pressure pulse.

For high energy deposition RIA experiments (greater than 400 cal/g), fuel vapor must also be considered as a potential working fluid. In other

words, the release of fuel vapor pressure upon failure of the fuel rod will generate a pressure pulse in the flow shroud. There are two methods of estimating fuel vapor pressure in a fuel rod. The first is to determine fuel enthalpy in the rod and then relate it to an experimentally derived caloric equation-of-state relating enthalpy to UO_2 vapor pressure. The second method is to use an experimentally derived temperature prediction of UO_2 vapor pressure. However, the caloric equation-of-state relating enthalpy to UO_2 vapor pressure indicates, for RIA-ST-4, that a maximum fuel vapor pressure of less than 1 MPa could be expected for an axial peak radial average fuel enthalpy of 350 cal/g at failure. The temperature prediction of fuel vapor pressure indicates an even lower pressure level. With an estimated peak pressure of ~1 MPa, fuel vapor can be ruled out as the working fluid for the RIA-ST-4 pressure transient.

The fill gas pressurization that occurs upon heating and the work potential of the gas have also been assessed as possible sources of the pressure pulse in RIA-ST-4. Two cases were considered. First, an assessment was made of the pressure and work potential that would be expected, assuming that the bond-gas was heated to the maximum fuel surface temperature just prior to failure and that no gap-gas relocation occurred during transient heating (that is, the gas heated up in a constant volume). Secondly, the effect of the gas contained in the dish spaces between the fuel pellets and in the open porosity of the fuel was assessed, assuming that the gas came to thermal equilibrium with the fuel at the average fuel temperature in the molten length of the fuel stack at the time of failure (in this case, the release of gas to the plenum was discounted).

The results of these assessments indicate that the initial pressurization could be accounted for by internal gas pressurization, assuming no volume change. The calculated pressurizations were 65 MPa for the first case and 87 MPa for the second case. For the first case, assuming the entire volume of the gap gas was heated to the maximum fuel surface temperature and considering either isothermal or isotropic expansion down to the approximate system pressure of 6.8 MPa, the work potential is negligibly small (100 cal or less compared with 9670 cal estimated for the kinetic energy of the water slug). For the second case, the work potential for expansion down to system pressure was also negligibly small (101 cal). Therefore, even through the initial system pressurization could be accounted for by internal gas pressurization, the work done on the system could not have resulted from fuel rod internal gas pressurization.

7.7 Posttest Metallurgical Results

Extensive fuel fragmentation is generally observed for fuel rod failures under simulated severe reactivity insertion accident conditions. Posttest metallurgical examination of the RIA-ST-4 test section was performed to assess the fuel fragmentation that occurred as a result of rod failure in a flowing coolant environment. In addition, an assessment of the dynamic pressure loading required to cause the observed flow shroud deformation was made. These two topics are discussed in the following paragraphs.

7.7.1 Metallurgical Observations. Severe fuel fragmenation occurred, as evidenced by the collection of finely fragmented fuel from the test loop. A total of 143.4 g of fuel fragments were collected from within the shroud and the upper filter, and the size distribution was determined by a sieve analysis. An additional 11.8 g of fuel fragments, which were not sieved, were either left within a lower filter or fell from the shroud during handling. Fuel was also found adhering to the inside surface of the flow shroud. Since the starting fuel weight was 632.8 g, approximately three-quarters of the fuel is estimated to have been deposited onto the shroud, assuming negligible fuel washout into the PBF loop.

The results of the screening measurements are summarized in Table 15 and the size distribution is shown graphically in Figure 48. The particle size distribution is characteristic of that generally observed in MFCI events. The figure indicates that the fuel particles were smaller within the upper filter than within the shroud, presumably because smaller particles move upward more easily with the pressure difference and coolant flow. Figure 49 illustrates the fuel found adhered to the inside surface of the flow shroud. Although ~75% of the total fuel was deposited onto the shroud, the results shown in Figure 48 probably represent typical fuel behavior. That is, if the shroud had been absent, the particle size distribution of the fuel deposited onto the shroud would have been the same as that of the fuel collected for the screening measurements.

TABLE 15. RESULTS OF THE RIA-ST-4 FUEL SCREENING MEASUREMENTS

		Fuel Fragments Left in Each Vial					
		Within Shroud		Within Upper Filter		Total	
Vial	Screen Size (μm)	Weight (g)	Fraction (%)	Weight (g)	Fraction (%)	Weight (g)	Fraction (%)
1	5600	4.9178	4.47	0	0	4.9178	3.43
2	2000	46.9841	42.69	7.0571	21.18	54.0412	37.69
3	1700	9.6056	8.73	3.4272	10.29	13.0328	9.09
4	1180	9.9552	9.04	6.0260	18.08	15.9812	11.15
5	850	12.7180	11.56	5.4588	16.38	18.1768	12.68
6	500	10.0368	9.12	4.4300	13.29	14.4668	10.09
7	355	4.0296	3.66	1.9619	5.89	5.9915	4.18
8	212	3.6952	3.36	2.3778	7.14	6.0730	4.24
9	150	1.2592	1.14	1.0541	3.16	2.3133	1.61
10	106	1.5866	1.44	0.8498	2.55	2.4364	1.70
11	75	1.8014	1.64	0.4413	1.32	2.2427	1.56
12	63	1.4874	1.35	0.1230	0.37	1.6104	1.12
13	45	1.3024	1.18	0.1152	0.35	1.4176	0.99
14	38	0.3956	0.36	0	0	0.3956	0.28
14	38	0.2896	0.26	0	0	0.2896	0.20
Total		110.0645	100.00	33.3222	100.00	143.3867	100.00

In addition to the tabulated fragments, 6.2385 and 5.5463 g of fuel fragments were left within the lower filter and fell from the assembly, respectively. These fragments were not analyzed by screening.

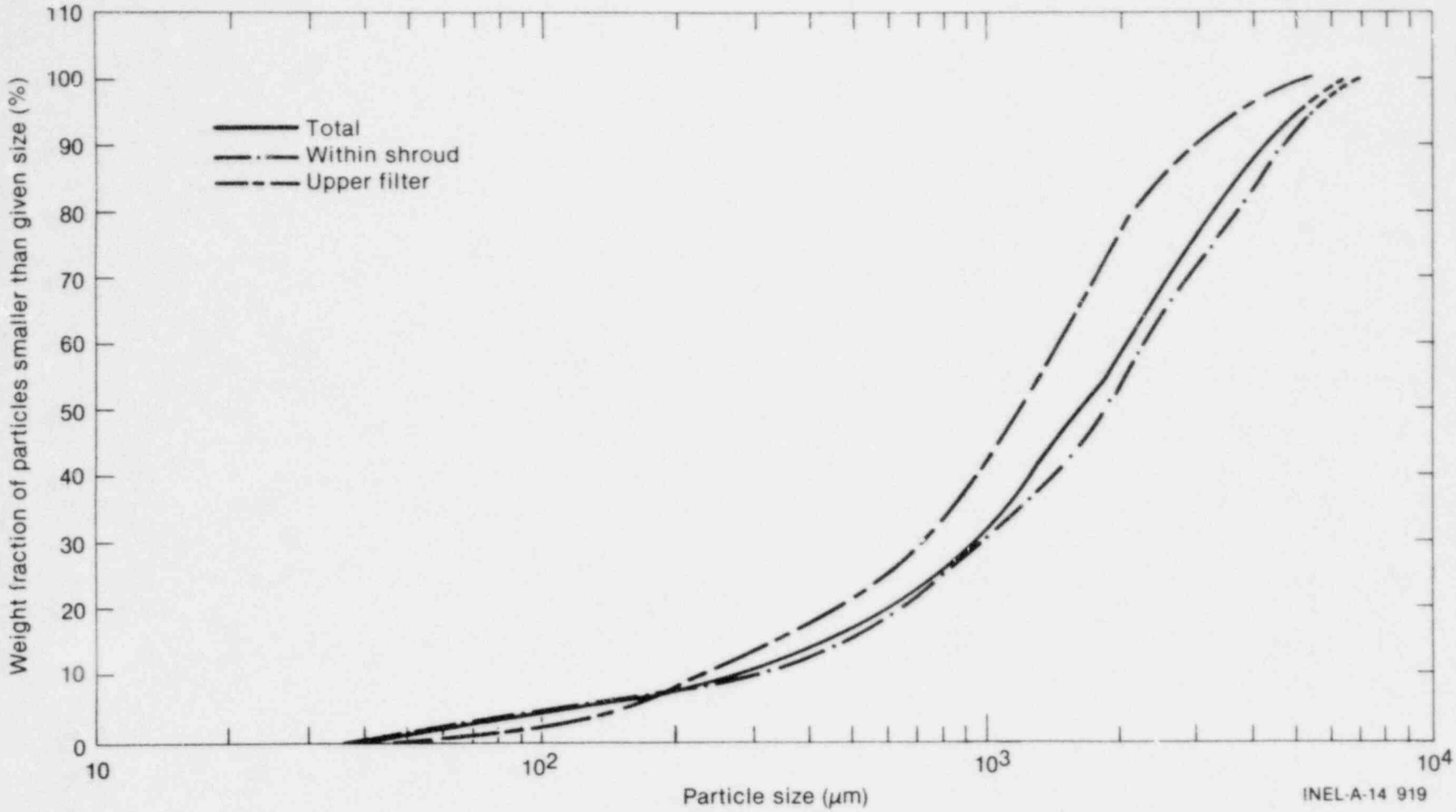

Figure 48. Fuel particle size distribution in high energy deposition experiment (RIA-ST-4).

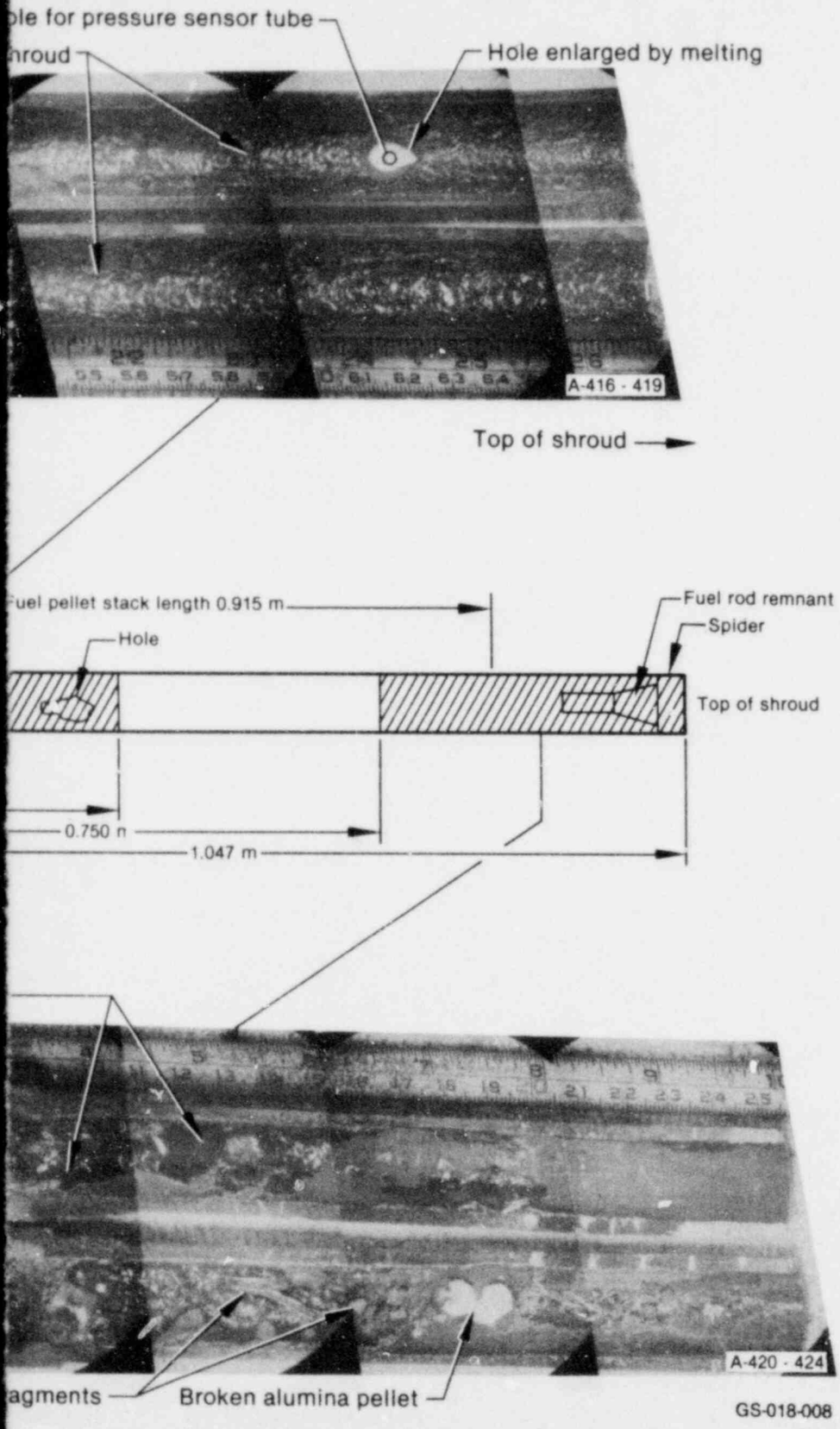

o the inside surface of the flow shroud and fuel debris found in the test section from

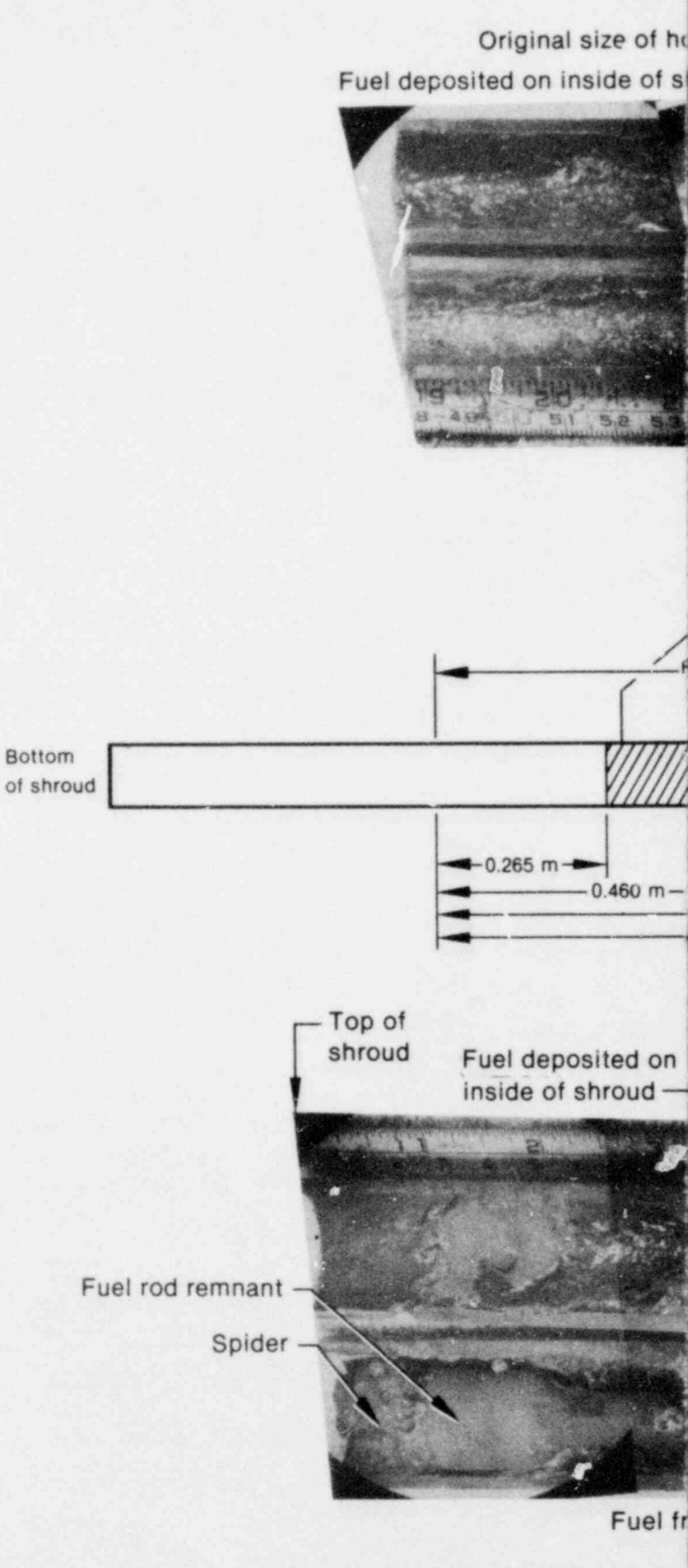

Figure 49. Photographs of fuel found adhered t RIA-ST-4.

As shown in Figure 50, most of the particles were spherical or outlined by a round edge. This suggests that the fuel was molten at the time it fragmented rather than after the rod failure. A few unmelted pieces of fuel were observed in the debris, indicating that the fuel at the extreme ends of the active fuel stack did not melt. The observed fuel fragments probably include the cladding debris which did not deposit on the shroud inner surface along with the UO_2 fuel. It is difficult to distinguish cladding fragments from fuel fragments because nonmolten cladding fragments were not found in the collected fuel fragments; almost all of the cladding debris appeared to have been previously molten.

The tube that had been attached to the flow shroud at the midplane for pressure measurement became detached, possibly by melting. The post-test microstructure of the zircaloy flow shroud indicated an outer surface zircaloy-steam reaction, which implies that film boiling occurred on the outside of the shroud. A dendritic microstructure was observed for the fuel-cladding layer found adhering to the inside surface of the flow shroud, indicating that the fuel was previously molten, since dendritic structures only form upon solidification. Further, the porous nature of the fuel suggests that it was deposited on the inside surface of the flow shroud in a liquid state, since a volume decrease occurs upon solidification. Thus, the fuel attached to the inside surface of the flow shroud was probably liquid at some time during deposition. It is not presently possible to assess from the metallurgical examination whether the fuel was previously vaporized.

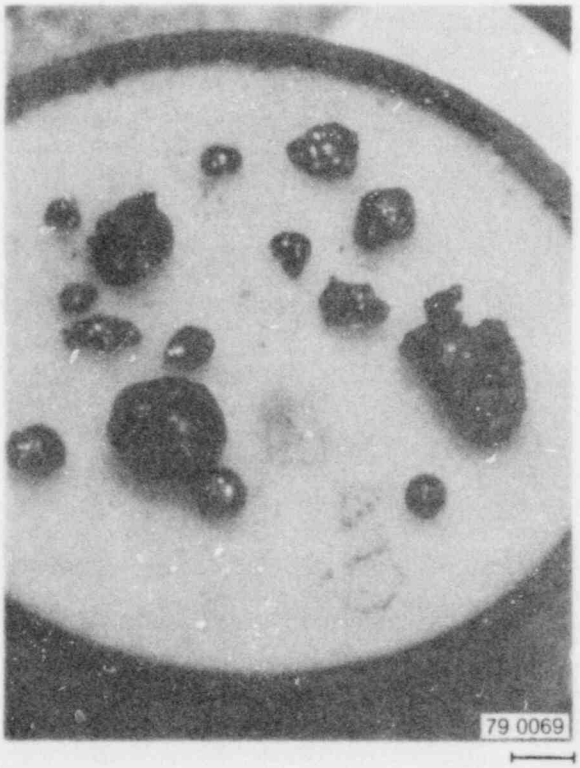

Figure 50. Typical appearance of fuel particles from RIA-ST-4 rod.

Oxidation thickness measurements were made as a function of axial location along the flow shroud to estimate the shroud temperatures. From these measurements it appears that the flow shroud reached ~1550 K at the outer surface. On the basis of the energy deposited in the test fuel rod per centimetre of shroud length, the possibility exists for zircaloy shroud heating to near melting. However, comparison of the thermal response time scale of the power burst with the rise and decay time of the pressure pulse indicates that the power burst and pressure pulse were essentially over before the flow shroud heated up. As a result, the calculations of the effect of the pressure pulse on the flow shroud deformation, discussed in the following parapraphs, were performed assuming lower shroud temperatures.

7.7.2 Assessment of Dynamic Pressure Loading of Flow Shroud. Posttest measurements of the flow shroud deformation indicated that significant deformation occurred despite the fact that the shroud wall thickness was 6.35 mm. To account for the observed deformation, a dynamic-loading stress analysis assessment of the pressurization was performed. The maximum measured increase in outer diameter was 2.2 mm. The analysis indicated that neither a 37-MPa nor even a 52-MPa pressure pulse could have caused the observed deformation when the shroud was relatively cool. Since the calculated deformations are much smaller than observed, the shroud inside surface must have been heated by contact with the fuel, such that the mechanical strength of the flow shroud wall was degraded. Shroud-fuel contact probably occurred immediately following rod breakup. Therefore, shroud deformation was calculated considering some wall heating. Figure 51 illustrates the stress-strain relationships used to assess the heated shroud deformation. These calculations clearly indicate that even if inside shroud wall heating is accounted for during

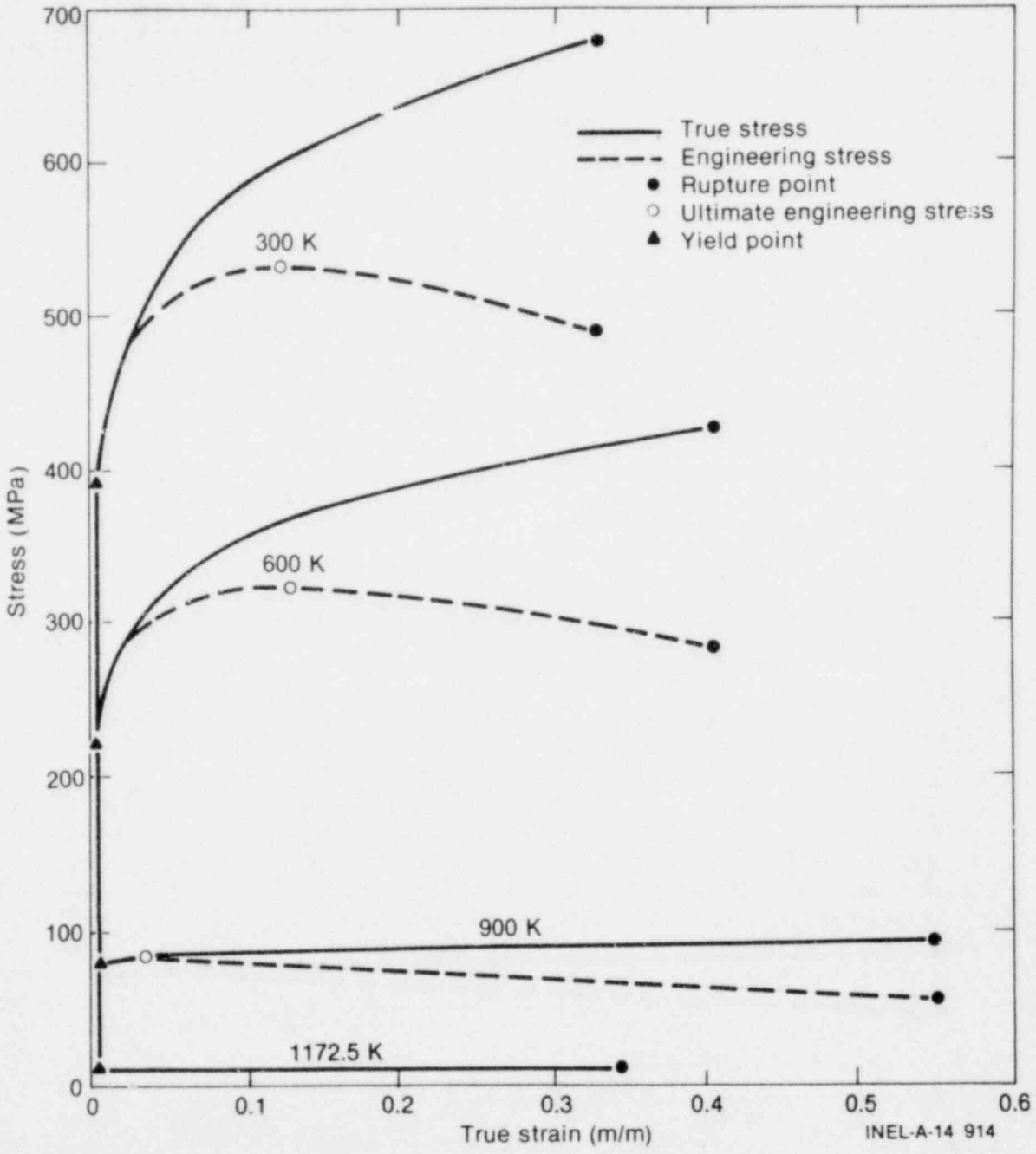

Figure 51. Stress-strain curves used to assess RIA-ST-4 shroud deformation.

the entire 20-ms pulse period, the resultant deformation predicted to occur only during this period is quite minimal; approximately an order-of-magnitude less than that which was observed. Therefore, it is concluded that shroud deformation occurred over a longer time period while the pressure-pulse-induced pressure difference was still significant (~5 MPa) and the flow shroud was hot due to film boiling.

7.8 Summary of High Energy Deposition Consequences

The peak pressure, pressure increase, and rise time results from the four pressure transducers used in RIA-ST-4 are given in Figure 44 and Table 14. The highest pressure indication was 34.6 MPa in the inlet section of the flow shroud. The peak pressures measured in the upper plenum and flow bypass regions were less than 9 MPa. An assessment of the source pressure pulse was made by modeling the PBF test loop with the WHAM computer code and assuming that the fluid in the source region was either compressible or incompressible. The source pressure pulses which best simulated the measured pressure conditions had peaks of 37 and 52 MPa for the incompressible and compressible cases, respectively.

A mechanical-to-nuclear energy conversion ratio was calculated to aid in extrapolating the RIA-ST-4 results to other reactor systems. The working fluid was assumed to be incompressible (37-MPa peak pressure pulse) to determine this ratio, because that assumption yields the lowest conversion ratio and is conservative. The first step to determine this ratio was to obtain a rough estimate of the kinetic energy imparted to the system. With simplifying assumptions, the total change in kinetic energy over the entire pulse period was determined to be 9670 cal. The total nuclear energy contained in the fuel rod at the time of the pressure pulse was 1.60×10^5 cal. Thus, the conversion ratio was determined to be about 6%.

Using the FRAP-T5 code, the thermal condition of the fuel at the time of cladding failure was determined. The total radial average fuel enthalpy at the axial flux peak at failure was approximately 350 cal/g. FRAP-T5 indicated that the peak fuel temperature at this time was about 3740 K, and the cladding temperature was about 1000 K. Thus, the rod probably had molten fuel contained within cladding which was relatively cold (~1000 K) at failure.

At this point, the working fluid (fuel vapor, fuel rod fill gas, or water and steam mixture) which could have potentially produced the source pressure pulse was assessed. Fuel vapor was eliminated from consideration because it was determined that a maximum vapor pressure of less than 1 MPa could be expected from the estimated fuel rod thermal condition. The results of an analysis of the fill gas as the working fluid indicated that even though the initial flow shroud pressurization could be accounted for by internal gas pressurization, it was highly unlikely that the work done on the system could have resulted from fuel rod internal gas pressurization. It was therefore determined that the most likely working fluid was water in a liquid-vapor, or supercritical state during an MFCI.

It was determined from posttest metallurgical observations that severe fuel fragmentation occurred in RIA-ST-4. The fuel was probably molten at the time of the breakup. Molten fuel was also deposited onto the inside surface of the flow shroud. This resulted in film boiling on the outside surface of the flow shroud, and it was estimated that the outer flow shroud surface temperature reached a peak of 1550 K in the time frame of the overall pressure transient (~0.025 s). The flow shroud showed significant outer diameter increase. This deformation of the flow shroud (bulging) could be accounted for only by assuming that it occurred when the shroud was in a hot, weakened condition. Pressure pulses recorded in RIA-ST-4 were considered to have been caused by an energetic MFCI[23] that may be viewed in light of the Board-Hall detonation and propagation model.[24]

8. CONCLUSIONS

The RIA Scoping Tests were the first tests to provide RIA fuel behavior data under conditions typical of power reactor operation. The primary objectives of the tests were to:

1. Evaluate proposed methods for measuring fuel rod energy deposition during a power burst

2. Determine the peak fuel enthalpy threshold for failure and the rod failure mechanism of unirradiated fuel rods at BWR hot-startup coolant conditions

3. Determine the relative sensitivity of test instrumentation to high radiation during a power burst

4. Determine the magnitudes and sources of potential pressure pulses resulting from rod failure during an inadvertent high energy deposition in the PBF liquid filled test loop.

The results of the tests led to the following observations and conclusions:

1. The five power burst energy measurement methods have an estimated uncertainty ranging from ± 11 to $\pm 14\%$. Detailed independent review of the measurement methods confirmed that none of the measurements were unreliable; however, direct fuel burnup analysis of a fuel rod exposed only to the power burst was judged to be the most reliable method for measuring the total fuel energy. The other methods must rely on calorimetric or rod burnup measurements of the fuel rod power during steady state operation, and must then be interrelated to other neutron detecting instruments to measure the fuel rod energy during a power burst.

2. The axial peak radial average fuel enthalpy cladding failure threshold of the unirradiated test rods was concluded to be between 225 and 250 cal/g, since the RIA-ST-3 fuel rod remained intact when subjected to an axial peak radial average fuel enthalpy of 225 cal/g and the RIA-ST-1 rod failed at 250 cal/g. The axial peak radial average fuel enthalpy cladding failure threshold is probably about 240 cal/g. The corresponding axial and radial peak fuel enthalpy is 265 cal/g, which corresponds to a total radial average energy deposition of 315 cal/g UO_2 at the power peak elevation.

3. The cladding damage mechanisms occurring in the test rods subjected to power bursts resulting in axial peak radial average fuel enthalpies of 250 to 260 cal/g (axial and radial peak fuel enthalpies of 275 to 290 cal/g) included (a) plastic flow of the cladding, which produced regions of wall thickening and thinning; (b) zircaloy oxidation by steam and UO_2, which completely embrittled the thinner regions; and (c) cracks in the embrittled cladding due to thermal stresses and differential cladding and pellet thermal strains during quench from film boiling.

4. Local melting of a zirconium-UO_2 eutectic mixture was observed, but UO_2 fuel melting was not reached for the rods tested at 250 and 260 cal/g axial peak radial average fuel enthalpies (275 and 290 cal/g peak fuel enthalpies).

5. Fuel shattering along grain boundaries resulted in the washout of from 10 to 15% of the fuel from the rods tested at 250 and 260 cal/g axial peak radial average fuel enthalpies (275 and 290 cal/g peak fuel enthalpies).

6. The failure threshold of approximately 265 cal/g axial and radial peak fuel enthalpy under BWR hot-startup conditions is slightly higher than observed in CDC tests conducted in closed capsules under ambient pressure and elevated temperature conditions.

7. The radiation sensitivities of the five different pressure transducers, a thermocouple, a cladding elongation detector, and

two strain gages were measured during one or more power bursts. It was determined that only the radiation sensitivity of the strain gages was significant.

8. A large pressure pulse of 34.6 MPa was measured near the pressure source region during RIA-ST-4 for a peak fuel enthalpy of 350 cal/g (total energy deposition of 695 cal/g UO_2). WHAM computer code calculations indicate that the actual source pressure inside the flow shroud was in the range of 37 to 52 MPa, depending on the assumed compressibility of the source region.

9. Although a large source pressure occurred during RIA-ST-4, only low magnitude pressures were measured elsewhere in the in-pile tube and loop piping.

9. REFERENCES

1. *Code of Federal Regulations*, Title 10, Part 50, Appendix A, Criterion 28, "Reactivity Limits," 1979.

2. "Assumptions Used for Evaluating a Control Rod Ejection Accident for Pressurized Water Reactors," *NRC Regulatory Guide 1.77*, May 1974.

3. D. H. Risher, Jr., *An Evaluation of the Rod Ejection Accident in Westinghouse Pressurized Water Reactors Using Spatial Kinetics Methods*, WCAP-7588, December 1971, and Rev. 1-A, January 1975.

4. C. J. Paone et al., *Rod Drop Accident Analysis for Large Boiling Water Reactors*, NED-10527, March 1972.

5. T. Fujishiro, et al., *Light Water Reactor Fuel Response During Reactivity Initiated Accident Experiments*, NUREG/CR-0629, TREE 1237, August 1978.

6. United States Nuclear Regulatory Commission, Reactor Safety Research Program, *A Description of Current and Planned Reactor Safey Research Sponsored by the Nuclear Regulatory Commission's Division of Reactor Safety Research*, NUREG-75/058, June 1975.

7. T. E. Murley et al., "Summary of LWR Safety Research in the USA," *International Conference on Nuclear Power and Its Fuel Cycle, Salzburg, Austria*, NUREG-0234, May 1977.

8. C. L. Zimmermann et al., *Experimental Data Report for Test RIA-ST (Reactivity Initiated Accident Test Series)*, NUREG/CR-0473, TREE-1235, March 1979.

9. *Quarterly Progress Report on the NSRR Experiments (3)*, JAERI-M 7051, 1977.

10. P. Hofmann et al., "Chemical Interaction Between UO_2 and Zry-4 in the Temperature Range Between 900 and 1500°C," *ASTM STP 681, American Society for Testing and Materials*, 1979, pp. 537-560.

11. S. L. Seiffert and R. R. Hobbins, *Oxidation and Embrittlement of Zircaloy-4 Cladding from High Temperature Film Boiling Operation*, NUREG/CR-0517, TREE-1327, April 1979.

12. A. W. Cronenberg and T. R. Yackle, "Intergranular Fracture of Unrestructured UO_2 Fuel During Film Boiling Operation," *Journal of Nuclear Materials, 84*, 1979, pp. 295-318.

13. J. R. Coombe, G. A. Remley, R. K. Brown, *Radiation Effects Testing of Linear Variable Differential Transformers Used in Nerva Program*, WANL-TME-1779, April 1968.

14. F. S. Gunnerson and A. W. Cronenberg, "Film Boiling and Vapor Explosion Phenomena," to be published in *Nuclear Technology*, July 1980.

15. A. W. Cronenberg, "Recent Developments in the Understanding of Energetic Molten Fuel/Coolant Interactions," *Journal of Nuclear Safety, 21*, 3, May-June 1980.

16. H. K. Fauske, "On the Mechanisms of Uranium Dioxide - Sodium Explosive Interactions," *Nuclear Science and Energineering, 51*, 1973, pp. 95-101.

17. R. E. Henry and H. K. Fauske, "Nucleation Processes in Large Scale Vapor Explosions," *Journal of Heat Transfer, 101*, May 1979, pp. 280-287.

18. A. W. Cronenberg and M. A. Grolmes, "Fragmentation Modeling Relative to the Breakup of UO_2 in Sodium," *Nuclear Safety, 16*, 1975, pp. 683-700.

19. A. W. Cronenberg and R. Benz, *Vapor Explosion Phenomena with Respect to Nuclear Reactor Safety Assessment*, NUREG/CR-0245, TREE-1242, July 1978.

20. A. W. Cronenberg and R. Benz, "Vapor Explosion Phenomena with Respect to Nuclear Reactor Safety Assessment," *Advances in Nuclear Science and Technology, 12*, 1979, pp. 247-334.

21. J. A. Fox, *Hydraulic Analysis of Unsteady Flow in Pipe Networks*, New York: John Wiley & Son, 1977.

22. T. G. Taxelius (ed.), *Annual Report, SPERT Project, October 1968-September 1969*, IN-1370, June 1970.

23. M. S. El-Genk, "On a Vapor Explosion in the RIA-ST-4 Experiment," *American Nuclear Society Annual Meeting, Las Vegas, Nevada, June 8-13, 1980.*

24. S. J. Board, R. W. Hall, R. S. Hall, "Deformation of Fuel-Coolant Explosions," *Nature, 254*, March 1975.

DOCUMENT/ PAGE PULLED

ANO. 8005270156

NO. OF PAGES 1 / MICROFICHE

REASON:

☒ PAGE ILLEGIBLE:

☒ HARD COPY FILED AT: (PDR) CF

OTHER _____

☐ BETTER COPY REQUESTED ON ____/____/____

☐ PAGE TOO LARGE TO FILM:

☐ HARD COPY FILED AT: PDR CF

OTHER _____

☐ FILMED ON APERTURE CARD NO. _____